To the Graduate Council:

I am submitting herewith a thesis written by Kevin T. Zysk entitled "Pulsed CO_2 Laser Welding of Inconel 718." I have examined the final copy of this thesis for form and content and recommend that it be accepted in partial fulfillment of the requirements for the degree of Master of Science, with a major in Mechanical Engineering.

T. Dwayne McCay, Major Professor

We have read this thesis
and recommend its acceptance:

Mary Helen McCay

Jim-Mow Jeng

Accepted for the Council:

Vice Provost
and Dean of the Graduate School

STATEMENT OF PERMISSION TO USE

In presenting this thesis in partial fulfillment of the requirements for a Master's degree at the University of Tennessee, Knoxville, I agree that the Library shall make it available to borrowers under rules of the Library. Brief quotations from this thesis are allowable without special permission, provided that accurate acknowledgment of the source is made.

Permission for extensive quotation from or reproduction of this thesis may be granted by my major professor, or in his absence, by the Head of Interlibrary Services when, in the opinion of either, the proposed use of the material is for scholarly purposes. Any copying or use of the material in this thesis for financial gain shall not be allowed without my written permission.

Signature ____________________

Date 3 - 29 - 89

PULSED CO_2 LASER WELDING OF INCONEL 718

A Thesis

Presented for the

Master of Science

Degree

The University of Tennessee, Knoxville

Kevin T. Zysk

May 1989

ABSTRACT

Welding of Inconel 718 by conventional methods produces microfissures within the heat affected zone (HAZ) which weakens the weld. This study investigated the effects of pulsed CO_2 laser welding upon the HAZ to determine the suitability of this process for commercialization.

Samples of Inconel 718 in the as-received (AR) and solution-treated (ST) condition were pulse CO_2 laser welded (bead-on-plate) with a fixed pulse on-time and a varying off-time. Laser cavity peak power, shield gas flow rate, beam focus, and welding speed were held constant. Welded ST samples were subjected to furnace aging to simulate conditions used on most of the Space Shuttle Main Engine welds. A limited number of continuous wave (CW) welds were done on AR material for comparison.

Microhardness in the weld pool and base metal, top weld bead width, bottom weld bead width, cross-sectional area, percentage pore area, pore diameter, and pore spacing were measured. The number of microfissures per weld (cross-section) was quantified and the total microfissure length per weld (cross-section) was measured.

The HAZ was found not to extend beyond 0.2 mm from the weld pool. Porosity did not exist in the CW and short pulse off-time samples. Microfissures were not found in the pulse welded ST samples. Post-weld heat treatment induced microfissures in 1/3 of the pulse welded samples. All CW welded samples had microfissures.

The effect of subsequent pulses during welding shifts the tensile stress characteristics of the solidifying weld pool such that any induced residual stress is below the yield stress of the Inconel 718, thus eliminating microfissuring. Pulsed CO_2 laser welding has been shown to be an effective method of joining Inconel 718.

TABLE OF CONTENTS

LIST OF FIGURES

NOMENCLATURE

AR	As Received
CW	Continuous Wave
DC	Direct Current
EB	Electron Beam
GMAW	Gas Metal Arc Welding
GTAW	Gas Tungsten Arc Welding
HAZ	Heat Affected Zone
HV	Vicker's Hardness
LBW	Laser Beam Welding
MIG	Metal Inert Gas
SMAW	Shielded Metal Arc Welding
ST	Solution Treated
STA	Solution Treated and Aged
TIG	Tungsten Inert Gas
TP-LBW	Translating Pulsed Laser Beam Welding
f_1	Weld Process Heat Transfer Efficiency

n	Number of Tests Points in a Sample
s	Standard Deviation of Test Data
t	Student t Statistic
$\overline{x}$	Sample Mean Value
α	Confidence Level

CHAPTER I

INTRODUCTION

The 3180 *kg* Space Shuttle Main Engine (SSME) is constructed with 1600 *kg* of Inconel 718 using both cast and wrought forms. Fabrication of this engine requires extensive use of welding which induces microfissures within the heat affected zone (HAZ) of the alloy. Two theories explaining the occurrence of microfissuring in welded Inconel 718 have been postulated. One explanation is based on grain boundary liquation with an accompanied strain while the other considers the tensile strains induced when the HAZ cools and contracts while the surrounding environment is still heating and expanding [1]. The development of a welding process which can eliminate or reduce the number of microfissures within the welds used on the SSME will facilitate production of this engine and future engines.

This study was initiated to determine if Translating Pulsed Laser Beam Welding (TP-LBW) could produce welds in Inconel 718 free of microfissures and to provide the foundation necessary for future implementation of this process. Specifically, the objectives of this research were:

1. to compare the microstructure of the heat affected zone of a continuous wave laser beam weld (LBW) on Inconel 718 with that of the translating pulsed laser beam weld (TP-LBW) under equivalent conditions;
2. to relate the thermal history of the weld zone to the microstructure exhibited by the weld;
3. to establish the feasibility of TP-LBW for use in welding Inconel 718 and other alloys.

Many of the parameters common to continuous wave LBW apply to TP-LBW, such as shield gas flow, diffusivity of the material, beam absorption, and translation velocity. In addition, the same problems affecting continuous wave laser beam welds; porosity, depth of penetration , heat cracking, segregation, and microfissuring, affect the TP-LBW. The benefit of the TP-LBW process lies in the added degree of control afforded by manipulation of pulse energy, pulse overlap, and translation velocity. Energy input can be reduced, thereby reducing the width of the heat affected zone while still obtaining total penetration. Though much has been written concerning the effects of continuous wave laser beam welding, very little information is available for translating pulsed laser welds [2]. Information related to translating pulsed laser beam welding on Inconel 718 seems to be nonexistent.

Shield gas flow rate, beam focus, and translation velocity were held constant in the initial stage of this study. Upon determining the baseline conditions that produced a reasonable quality weld, either frequency or pulse off time was varied. This caused variations in the duty cycle which in turn affected the pulse overlap. These welds were compared to continuous wave welds made under similar conditions.

In the second phase of this study, pulse frequency and velocity were altered, while maintaining the same energy per pulse, to determine the effects of increased translation velocity on the weld microstructure.

All laser welding for this study was done at the Center For Laser Applications, University of Tennessee Space Institute, Tullahoma, Tennessee.

CHAPTER II

BACKGROUND

A. Conventional Welding Techniques

Conventional welding processes used on Inconel 718 include GTAW, GMAW, and SMAW. Plasma arc welding is also used to a limited extent on thicknesses up to 7 mm [3]. All of these processes require some form of weld shielding either as a blanket of inert gas over the weld surface or as a flux coating on the weld electrode which is deposited upon the weld surface during the welding operation. Helium and argon are the shielding gases most often used. These conventional welding techniques employ the use of a heat source at or above the surface of the weldment.

GTAW is the welding process commonly referred to as TIG (tungsten inert gas) welding by the metal fabrication industry. This process can be used with or without filler material. Autogenous welds (welds without the addition of any filler material) are typically used on precise fitting components which cannot tolerate either a large heat input without distortion or the buildup of additional material on the surface. GTAW is a slow process more suited for precision hand operations.

GTAW welding of aluminum or magnesium is done with an alternating current power source. The tungsten electrode is negative and argon is normally used as a shielding gas. Helium is used if an increased weld speed is necessary. The heat transfer characteristics of helium makes increased welding speeds possible. The use of alternating current provides a scouring action which helps to remove the rapidly formed oxides which reduce weld quality. This scouring action is not effective on other metals and therefore a direct current power supply is utilized for welding of most other metals [4]. Arc stability in GTAW is a function of both the tungsten electrode tip's taper and end diameter [5]. Contamination of the tip will alter the weld characteristics.

GMAW, also known as MIG welding, has become very popular within industry due to its ability to bridge large gaps, reducing the need for precise component fit-up prior to welding. A moving consumable positive electrode is mechanically fed off a spool to what is called the MIG weld gun. A mixture of argon and CO_2 are commonly used as shielding gases. The shielding gas is fed coaxially with the electrode wire through the MIG gun and is also used to cool the gun.

Weld quality is a function of feed wire diameter, nozzle weldcup, gas flow rate, gas selection, voltage, and weld speed [6]. In spite of these variables, this process is very repeatable and readily adaptable to manufacturing processes requiring automatic welding.

SMAW is the traditional welding process known as stick welding. A direct current power supply is used with a positive electrode. A flux coating on the electrode (stick) provides the shielding necessary to produce quality welds. This flux coating absorbs water from the air which can be released and converted to hydrogen during welding, leading to hydrogen embrittlement and potential cracking. Preheating of the electrodes is normally used to alleviate this problem. This welding process is poorly suited for production. It requires a worker to initiate an arc with a 30 mm electrode, weld till the electrode has been consumed, clean the flux slag which is deposited on the weld pool surface, replace the electrode and reinitiate welding.

The major advantage to this process is it can be done just about anywhere. There is no shielding gas to be blown away by air currents. If a DC power source can be made available, stick welding is possible.

Maximum power densities for conventional welding processes are in the range of

10^3 to 10^4 $Watts/cm^2$ [7]. Only a portion of this energy actually goes into creating the molten weld pool. It is estimated that f_1, the heat transfer efficiency of the mentioned welding processes, lies between 0.7 and 1.0. GTAW is the least efficient with a value for f_1 equal to 0.7 while GMAW has a f_1 value of 0.9 [8].

The weld geometries for these conventional welding processes are dictated by heat conduction through the material and surface tension driven flow. Highly conductive materials have weld pools which are broad and flat while poor thermally conductive materials such as stainless steels tend to have narrower and deeper weld pools. The geometry can be strongly modified depending upon the surface tension variation with temperature and the presence of surfactants. The input of large quantities of energy through the surface of the material being welded leads to the problems of material distortion and the creation of an excessive HAZ. Deep penetration welds with minimal distortion and minimal heat affected zones cannot normally be made in a single weld pass as can be done using laser beam welding. Welds in close proximity to heat sensitive components or materials are generally not possible with the conventional welding techniques but can be accomplished with the laser beam due to the narrow HAZ and small total heat input.

B. CW Laser Welding

Precise focusing of a laser beam permits the application of large amounts of energy to very small areas. This ability minimizes the problems of material distortion and excessive HAZ created by conventional heat sources. Power densities at or above 10^6 $Watts/cm^2$ are commonplace, while maximum power densities for conventional welding processes are in the range of 10^3 to 10^4 $Watts/cm^2$ [9].

Depending on the power density ($Watts/cm^2$) input to the workpiece, a laser weld can be either a conductive or a key hole type weld. Conduction limited welds are characterized by the transfer of energy to the weld pool by conduction alone. The thermal properties of the material determine weldability. Materials which are not highly thermally conductive produce better welds since rapid conduction of large quantities of energy away from the point of application does not occur. If a pool of molten metal cannot be maintained, there will be no fusing of the material. In order to maintain the molten pool during welding of highly conductive metals such as aluminum, a very large energy input is required. This can result in material distortion. Conduction limited welds typically have a large top weld bead width in relation to the depth of penetration and an extended HAZ, i.e. the weld profiles are semi-circular in shape.

In the keyhole case, the high intensity laser beam raises the temperature in the region of the beam spot to above the vaporization temperature of the metal. The beam then bores into the base material by vaporizing additional material. As the beam goes beyond its focus, the power density within the beam decreases. This diminished power density can be somewhat offset by internal reflection of the beam from the liquid region surrounding the keyhole. In effect, a nearly cylindrical region is vaporized [10]. This resulting void is maintained by the vapor pressure of the metal. The ability to focus the laser beam below the surface permits deep penetration autogenous (no filler metal added) welding in the key hole mode [11]. This type weld is typically used in production laser joining.

As with any weld, evaluation of the CW laser weld is based upon appearance, strength, porosity, distortion, and penetration. For many applications laser beam welding can consistently produce high quality welds at high production rates. The laser beam weld is noted for its narrow bead and narrow heat affected zone. Cooling is very rapid due to the large temperature gradients induced in the metal. As a result of the small weld zone and the comparatively small heat input to the weldment, distortion can be kept to a minimum.

The high rate of cooling in laser beam welded parts results in unique microstructures within the weld. Grain structure for laser welds tends to be smaller than that of conventional welds and has a very homogeneous distribution. The metal in the weld pool resembles cast metal which results in welds that are normally harder and have higher tensile strength than the surrounding base metal. With the short solidification time, microsegregation effects are minimized.

Porosity is a problem in laser welds due to the extremely high temperatures generated by the laser beam and the rapid cooling rates. Vaporized metal forms bubbles which are frozen in place if they are not able to reach the surface in the short time allowed for cooling.

C. Pulsed Laser Welding

Pulsed lasers commonly found in use today for metal joining include CO_2 and Neodymium:YAG. Each of these lasers has characteristics which make them suitable for specific tasks. A brief explanation of how a CO_2 laser functions can be found in Appendix A. The 10.6 μm radiation from the CO_2 laser is readily absorbed by glasses but is initially reflected by most metals. The 1.06 μm radiation from the Nd:YAG laser passes through most glass but is strongly absorbed by many metals [12]. The CO_2 lasers are better suited for jobs requiring large power inputs while the Nd:YAG lasers are ideally suited for welding small components. Materials which have been successfully laser pulse welded include gold, silver, aluminum, copper, iron, stainless steel, carbon steel, titanium, and nickel. Parameters controlling the pulsed welding process are translation velocity, power input, pulse frequency, and duty cycle.

Although pulsed lasers have been in use for many years [13], little data is readily available concerning the effects of part translation. Data from stationary pulsed welds do not correlate well with the results from translated pulsed welds due to blurring effects of the overlapped pulses from parts moving under a stationary beam.

Average power during pulsed welding is dependent upon the pulse duty cycle which is a ratio of the pulse on-time to the total on and off-time of the pulse. Figure II-1 (all figures can be found in Appendix B) gives a plot of power versus time for a CW laser and a pulsed laser. For the case shown (duty cycle equal to 2/3), the average power of the pulsed laser is 2/3's that of the CW laser. It is evident from the figure that while specific energy (J/mm) is viable for discussing the CW weld process, it is not useful in the pulse weld process. A more often used comparison is the energy per pulse ($J/pulse$) which is independent of both off-time and velocity.

The keyhole effect also exists in the pulsed welding mode although its nature is dictated by the pulse frequency and workpiece velocity. At a high pulse rate and slow velocity, the resulting weld will resemble that of a CW weld. At a low pulse rate relative to the translation velocity, a series of distinct overlapped welds becomes evident.

D. Stress in Weldments

During welding, the weld pool experiences both compressive and tensile forces from hot expanding material pushing against cooler restrained material. The stress distribution in the weld pool dramatically changes with distance from the point of heat input. At the point of application of the heat source the material is assumed to be in a liquid state and therefore cannot withstand a shear stress. A short distance from the weld center the material is expanding and creating a compressive force which is countered by a tensile force acting to resist this expansion in the cooler region away from the weld center. This is depicted in Figure II-2a [14].

As the region just behind the point of heat application begins to cool, the weld pool center rapidly contracts creating a large tensile force. This region cools at a rate faster than the outer region which is still expanding causing local compression. The outermost region of the HAZ which remained relatively cool remains in tension as seen in Figure II-2b. When the weld pool is finally cooled, the center stays in tension with the outer region remaining in compression as shown in Figure II-2c.

Hot cracking, tearing, or microfissure can occur any time during the welding process that there is adequate tensile force to rupture the material. The problem is most severe at temperatures near the solidus since the material is in its weakest state [15]. Figure II-3 shows the relationship between yield stress and temperature for a typical structural steel [16]. It is clear that as the melting temperature of the metal is approached, yield stress goes to zero. Liquation at the grain boundary or the presence of intergranular low melting point liquid weakens the grain boundary permitting the tensile forces to pull the material apart at the grain boundary. This is not a problem in the region subject to compressive forces.

E. Inconel 718

Inconel 718 accounts for 35% of all superalloy production. This widely used superalloy was developed over 30 years ago by H. C. Eiselstein who performed much of the early research on the material [17]. The material is routinely used for turbine disks in medium temperature gas turbines because of its resistance to creep and stress rupture at elevated temperatures.

In addition to use in gas turbines, Inconel 718 is currently in use in areas such as nuclear power plants (both piping and reactor vessel usage) and cryogenic facilities. Present applications are limited to temperatures between - 269°C and 700°C [18].

Inconel 718 has a nickel-iron base with additions of niobium, titanium, aluminum, carbon, boron, and other trace elements. Table II-1 gives the weight per cent of the constituents of wrought Inconel 718 [19]. All tables can be found in Appendix C. The physical properties of Inconel 718 are a direct result of its alloying elements. Within the base of nickel and iron, chromium acts to resist oxidation. Strength is enhanced using tungsten and molybdenum in a solid solution with additional strength gained from the precipitation of excess supersaturated compounds formed from aluminum, carbon, niobium, and titanium [20]. Unfortunately, niobium is also considered responsible for the undesirable characteristic of microfissuring of the alloy in the heat affected zone after welding.

The mechanical characteristics of Inconel 718 are a result of the formation of phases or compounds within the matrix structure. These phases can be manipulated by heat treatment to significantly alter the properties of the alloy. The two forms of heat treatments typically used are ST (solution treated) and STA (solution treated and aged). Treatment ST consists of heating the as received material to 1038±25°C for 25 minutes and then air cooling the material. This is done prior to any welding to reduce or eliminate any internal stresses resulting from previous fabrication processes (rolling in the case of the stock used for this study).

Treatment STA is used on welded parts which have been solution treated (ST) prior to welding. The welded parts are heated to 760±8°C for ten hours followed by a reduction in temperature to 650±8°C for an additional ten hours. This process brings the material to a fully precipitation hardened state. This is the same heat treatment used on approximately 90% of the Space Shuttle Main Engine welded components [21].

Phases found in aged material include:

1. γ FCC nickel iron matrix;
2. γ' Ni_3Al or $Ni_3(Al, Ti)$;
3. η Ni_3Ti;
4. γ'' Ni_3Nb.

These are considered to be the primary or principal phases.

Secondary phases that may form are the carbides:

1. $M_{23}C$;
2. M_7C_3;
3. M_6C;
4. MC.

Varying amounts of nitrides (MN), carbonitrides (MCN), and Borides (M_3B_2) may also be present [22].

Other phases which have a major impact on the alloy are the Laves phase (M_2Ti) and the δ (delta) phase (Ni_3Nb). The δ phase has an orthorhombic crystal structure which is platelike in appearance [23]. These phases restrain grain growth at temperatures below 1000°C [24].

Inconel 718 is successfully welded with GTAW, GMAW, SMAW, EB, and LBW processes. With all of these methods, however, microfissuring within the HAZ has been a problem.

F. Rofin-Sinar 3000 Processing System

The Rofin-Sinar 3000 Processing System (CO_2 Laser) used for this study is equipped with a high speed axial flow cavity. The laser is RF excited at 27.12 MHz

and has a linearly polarized output delivered at 45° to the workpiece. Average continuous power can be varied between 0.2 and 3.7 kW.

Output from the laser is possible in three distinct spatial modes:

1. TEM_{00};
2. TEM_{10};
3. TEM_{20}.

In addition, four temporal modes can be selected. These are:

1. Full CW;
2. 5 kHz modulated power;
3. Pulsed (up to 25 kHz);
4. Superpulsed (up to 25 kHz).

Workpiece manipulation is achieved with a five axis CNC computer driven Aerotech work station.

CHAPTER III

EXPERIMENTAL PROCEDURES

A. Sample Preparation

To provide an effective basis for comparison of microstructural changes, three sets of sample treatments were employed:

1. welded as received (AR) without any heat treatment;
2. heat treated to condition ST and welded;
3. heat treated to condition ST, welded, and treated to condition STA.

In addition, three weld sample categories were used in this study:

1. Control (no welds);
2. Pulse Welded;
3. CW Welded.

Unwelded control samples of the Inconel 718 were also subjected to the same heat treatment conditions to provide a standard by which hardness changes in the heat affected zone of the welded samples could be compared. A material process flow chart for this study is shown in Figure III-1. The tests designated in this figure will be described in detail in a later section.

Sample sizes were 3.2 *mm* thick by 50 *mm* wide by 70 *mm* long. All welding was done across the 50 *mm* width. Figure III-2 shows the spatial orientation used and the sample dimensions. The AR samples were cleaned with acetone, lightly scuffed with a medium grade (green) Scotch-Brite abrasive, and flushed with acetone prior to welding. The ST and STA samples were scuffed lightly with 400 grit silicon carbide abrasive paper prior to welding to remove the light oxide coating developed during the heat treatment, and flushed with acetone.

B. Welding

Helium was selected as the shielding gas based on the desire to minimize the generation of plasma during the welding process [25]. A gas flow rate, consistent with the requirements for welding of stainless steel (approximately 60 *liters/minute*) was used [26]. Both a coaxial (with the beam) flow and a plasma destruct jet were employed. The schematic for this arrangement is shown in Figure III-3.

The parts to be welded were mounted so that they were partially restrained from moving vertically along the Z axis but could expand along either the X or Y axis. Figure III-4 shows the fixture used for all welding in this study.

For pulsed welding with an indicated peak power of 3.2 *kW*, 17 *ms* on-time was necessary to produce complete penetration of the sample. Indicated peak power was the laser output reading shown on the operation console display. Pulse off-time was varied from 1 *ms* to 21 *ms* in increments of 2 *ms*. All pulse welded samples will be denoted by the combination of heat treatment received and pulse off-time, i.e. STA7 refers to the sample which was treated to the STA condition after pulse welding with an off-time of 7 *ms*. Similar nomenclature is used for the other pulse times, e.g. AR9 designates the as received condition welded with an off-time of 9 *ms*. All pulsed weld parameters are shown in Table III-1.

The AR samples were welded prior to welding of the ST samples. Beam focus was set at 1 *mm* below the XY plane (top surface) of all welded samples. Beam focus was checked before welding and after completion of welding the AR samples. Beam focus was not checked for the subsequent welding of the ST samples. Laser power output calibration was done prior to welding the AR samples but not repeated for the subsequent welding of the ST samples. Power output calibration measurements were done with a Scientech Model 390 water-cooled flow calorimeter. Figure III-5 is the calibration curve generated for the prescribed welding conditions. Delivered power was the calibrated power delivered to the samples as determined by the calorimeter. All welding was done in the TEM_{10} mode (see Appendix A). Weld table translation for the pulse welded samples was set at 1.5 m/min. This value was selected to provide an approximation to industrial welding speeds [27]. A single weld pass 20 mm from the outer edge of the XZ plane and 40 mm in length was made on each welded sample. Welding was initiated 20 mm from the edge of the YZ plane.

The STA samples were cut from the ST samples which had been previously welded. These cut sections (in the ST condition) were then heat treated to the STA condition. There was no additional welding done on these heat treated sections which became the STA samples.

CW welding was done with an average delivered peak power of 2.5 kW. Gas flow rates were the same as those used for the pulsed welds. Translation velocity was varied between 1.5 m/min and 3.5 m/min in 0.5 m/min increments. All CW welded samples will be denoted by the combination of welding mode and welding speed, i.e. CW1.5 refers to the CW welded sample welded at the rate of 1.5 m/min. All CW weld parameters are shown in Table III-2.

C. Metallurgical Examination

The AR bead-on-plate welded samples were cut into both cross sectional (YZ plane) and longitudinal (XZ plane) sections for examination. The XZ plane sections were ground to the weld centerline using sequentially 80 grit, 120 grit, 180 grit, 240 grit, 320 grit, 400 grit, and finishing with 600 grit wet silicon carbide abrasive paper. This was followed by polishing with nine micron synthetic diamond paste on a silk wheel. The samples were then etched for 15 seconds using Marble's solution, (10g $CuSO_4$, 50ml HCl, 50ml H_2O). YZ plane sections were ground using the same sequence of abrasives as used on the XZ plane sections. The polished YZ plane sections were etched with Marble's solution to bring out the desired grain and dendritic structures. Light etching was chosen so microfissuring and cracking at the grain boundaries adjacent to the weld pool area would be clearly visible along with the microstructure in the fusion zone and base metal. This technique also has the added benefit of not overpowering the dendritic structure in the weld pool area with excess etchant.

The ST and STA heat treated samples were sectioned in the YZ plane for examination. The same polishing and etching procedures were employed as for the AR samples.

After etching, all samples were examined using an optical (Olympus model PME) metallurgical microscope. This microscope is connected by a color video camera to a VICOM digital image processing system. Cross sectional area, top weld bead width, bottom weld bead width, gas pore diameter, gas pore spacing, gas pore area fraction, crack length, and number of cracks were measured.

Photographs showing the total weld cross section of each weld in the AR heat treatment condition were taken and are shown in Figure III-6. Additional higher magnification photographs were taken of each weld in each heat treatment condition. Three locations were chosen for high magnification (100X and 800X) comparison. These locations are shown in Figure III-7.

D. Mechanical Properties Evaluation

All samples were microhardness tested using a Buehler Micromet II microhardness tester with a 500 gram mass impactor. Impact time was set at ten seconds. Test points selected are shown in Figure III-8. Impact spacing outside the weld pool was kept at 0.2 mm. The control samples were tested every 0.25 mm across the 3.2 mm thickness of the sample stock.

CHAPTER IV

RESULTS AND DISCUSSION

A. Microhardness

The control samples had average microhardness values in Vickers Hardness units of 220±9, 230±10, and 380±9 respectively for the AR, ST, and STA conditions. Figure IV-1 shows the average microhardness values in the base metal region of the pulse welded samples for the three treatment conditions. Microhardness in the base metal at a distance greater than 0.2 *mm* from the weld pool showed no significant difference from the control samples. This indicates the HAZ is less than 0.2 *mm* in width or less than 20% of the pool width. This is a significant reduction in HAZ width compared to conventional methods which generate a HAZ of approximately 100% of the weld width for welds less than 3 *mm* in width [28].

Average values of microhardness within the weld pool were greater than the base metal values. Microhardness values for the AR (pulsed and CW) and ST samples were in the range of 260-300 HV while the STA samples were in the range of 400-500 HV. The high values of microhardness for the STA samples are indicative of the hardness induced by the precipitation process.

The scatter in microhardness data for the STA samples has not been explained at this time. Transmission electron microscopy would be necessary but such an instrument was not available.

Determination of microhardness test reliability was accomplished assuming a normal t distribution and using the formula for small-sample tests concerning the differences between two means given as

$$t = \frac{(\overline{x}_1 - \overline{x}_2)\sqrt{\frac{n_1 n_2 (n_1 + n_2)}{n_1 + n_2}}}{\sqrt{(n_1 - 1)s_1^2 + (n_2 - 1)s_2^2}} \tag{1}$$

where s is the standard deviation, $\overline{x}$ is the sample average, and n is the number of microhardness test points used for calculation of the sample mean [29]. The number of actual tests points or sample size (n_1 and n_2) used in calculating each mean and standard deviation was 15. The level of significance α , the probability of rejecting the null hypothesis when it was true, was set at $\alpha = 0.01$. The null hypothesis was

$$\overline{x}_1 = \overline{x}_2, \tag{2}$$

i.e. there was no difference between average microhardness values from test to test. The alternative hypothesis was

$$\overline{x}_1 - \overline{x}_2 \neq 0 \tag{3}$$

with rejection of the null hypothesis occurring if the value for t was less than $-t_{\alpha/2}$ or if t was greater than $t_{\alpha/2}$. The value for $t_{\alpha/2}$ ($\alpha/2 = .005$) with $(n_1 + n_2 - 2)$ =28 degrees of freedom is 2.763 [30]. This test was applied to sample STA7. Three separate mean values of microhardness in the base metal region of the YZ plane were generated using this one sample. Values of average microhardness in Vickers Hardness units for the three tests in the base metal YZ plane of sample STA7 were 421$\pm$15, 428$\pm$12, and 424$\pm$14. In each of the possible combinations the difference in means was found not to be significant. It is concluded that these test sample average microhardness values represent the true average values and the microhardness values of the other samples in this study are reliable indicators of the true microhardness.

B. Gas Porosity in the Welds

Figure IV-2 and Figure IV-3 are plots of gas pore diameter and gas pore spacing versus pulse off-time respectively. There is no clear dependency on pulse off-time. Figure IV-4 shows gas pore area fraction percentage (for the centerline XZ plane in the AR samples) as a function of pulse off-time. Gas pores did not exist or represented less than 0.2% of the total XZ plane area (along the centerline of the weld pool) for samples AR5 through AR13. Gas pore XZ area fraction for samples AR15 through AR21 varied between 1% and 5% with a trend of increased gas pore area with increased pulse off-time. Gas porosity was not found in the CW1.5 sample.

In the CW welds there is adequate heat input and time to allow vaporized material to be released through the molten weld surface. This is also apparent in the short pulse off-time (AR5-AR13) samples. Gas pore or bubble growth by agglomeration in the long pulse off-time samples depends on convective flow within the weld pool and reduced cooling rates. Convective flows are needed to bring multiple gas pores into contact. If the cooling rate is too high, the gas pores will not have sufficient time to grow by agglomeration and will remain a fixed size. This can be seen in Figure IV-2 for samples AR15-AR21. Figure IV-5 shows a gas pore forming by agglomeration.

C. Microfissure

Figure IV-6(a) show the number of microfissures for the CW weld speeds. Each sample had at least one microfissure. The occurrence of microfissure in the region below the top nailhead of sample CW1.5 is clearly shown in Figure IV-7. Any quantitative relationship between weld velocity and the number of microfissures is unclear. However, it is clear that CW welding on Inconel 718 using the conditions listed in Table III-2 yields undesirable results with respect to cracking.

Examination of the pulse welded AR samples revealed one microfissure in sample AR15. No evidence of microfissuring was found in the ST samples. Three STA samples each contained a single microfissure. Figures IV-6 (b) and (c) give the number of microfissures versus pulse off-time for the AR and STA samples. The sensitivity to microfissuring during post weld heat treatment was evident. Three samples which had no signs of microfissure in the ST condition developed cracks during the post weld STA heat treatment.

There are two possible explanations for the lack of microfissure in the AR and ST pulse welded samples. The first explanation is that during the time when the tensile stress induced by the cooling HAZ was above the yield point, there was sufficient heat input from subsequent pulses to remelt material and back fill any microfissure. The second explanation is based upon Figure IV-8 which superimposes a curve of yield strength versus time at temperature and tensile stress versus time for a weld. As the temperature of the HAZ rises (with time and energy input) the yield stress goes to zero. When the weld pool is no longer subject to energy input from the pulsed laser beam, the yield stress within the HAZ begins to rise and eventually reaches a yield stress above the starting point. During this same period, the HAZ has been experiencing first a compressive stress followed by an increasing tensile stress which ultimately reduces upon cooling. At any time that the tensile stress exceeds the yield stress, microfissuring will occur. If the onset of subsequent pulses is able to shift the tensile strain curve to the region below the yield stress curve, microfissuring should not occur. The possibility of both these actions occurring together exists.

Total length of microfissure per weld in the YZ plane for the fully penetrated CW welds did not show any clear dependency on weld speed. Figure IV-9 gives the length of microfissure versus pulse off-time for the CW, AR, and STA samples. Total microfissure length for samples STA7, STA15, and STA17 showed a decrease with increased pulse off-time. No conclusion based upon this limited data can be drawn.

D. Weld Dimensions

Top weld bead width for the CW samples showed little variation with welding speed, Figure IV-10. Bottom weld bead width for all the CW samples showed a dependency upon welding speed. Figure IV-11 gives weld bottom bead width versus velocity. As welding speed decreased, the bottom weld bead width increased. This was to be expected since the specific energy increased from 43 J/min to 100 J/min.

Top weld bead width for the pulse welded samples showed a decline in bead width with increased off-time, Figure IV-12. This would be expected since as off-time increased there was less energy available for formation of the weld pool. In the bottom weld bead width measurements there was considerable data scatter, Figure IV-13. The data scatter can be attributed to the relative position along the YZ plane during sectioning. The samples with a greater amount of off-time permitted a greater chance of sectioning at a narrow point in the weld which had minimal heat input.

YZ plane weld pool area measurements for the CW samples showed a decline with increased welding speed, Figure IV-14. Despite the uncertainty in bottom weld bead width measurements from sample sectioning methods, the YZ plane area measurements for the pulse welded samples decreased with the increase in pulse off-time. The increase in pulse off-time reduced the amount of energy available for melting which reduced the weld pool area. Figure IV-15 gives the YZ plane area versus pulse off-time.

CHAPTER V

CONCLUSIONS

As a result of this study of pulse tailored and CW CO_2 laser welding of Inconel 718, the following conclusions can be made:

1. Quality pulse tailored welding of small grain (ASTM #8) wrought Inconel 718, with a thickness of 3.2 *mm*, is possible using the following conditions
    a. pulse off-time between 5 *ms* and 9 *ms*
    b. pulse on-time of 17 *ms*
    c. welding speed of 1.5 m/min
    d. cavity peak power of 3200 W;
2. CW welding using the parameters in Table III-2 is not feasible;
3. Microhardness in the base metal region is not affected by welding;
4. The HAZ is less than 0.2 *mm* in width;
5. Pulse weld dimensions are smaller than those of CW welds;
6. Pores are not present in samples with off-times between 5 *ms* and 9 *ms*;
7. Pulse welding of ST material does not produce significant microfissuring;
8. Post weld heat treatment tends to induce microfissuring.

Using the restrictions imposed by Table III-1 has produced a narrow range of acceptable welds. A systematic variation of those parameters may lead to an expansion of the acceptable range. It is clear that more research into the effects of pulse welding on Inconel 718 is needed before this process can be implemented commercially.

LIST OF REFERENCES

REFERENCES

[1] A. Nunes, *NASA TM-82531* p. 1-4, June 1983.

[2] M. J. Cieslak and P. W. Fuersback, "On The Weldability, Composition, and Hardness of Pulsed and Continuous Nd:YAG Laser Welds In Aluminum 6061, 5456, and 5086," *Naval Engineers Journal*, p. 61 Aug. 1981

[3] E. F. Nippes, *Metals Handbook*, 9th Edition, Vol. 6 (Welding, Brazing, and Soldering), p. 440, 1986.

[4] Ref. [3], p. 41.

[5] Ref. [3], p. 438.

[6] Ref. [3], p. 440.

[7] Ref. [3], p. 32.

[8] Ref. [3], p. 32.

[9] Ref. [3], p. 32.

[10] E. A. Metzbower, "Laser Welding," *Naval Engineers Journal*, p. 50, Aug. 1981.

[11] Ref. [3], p. 649.

[12] Michael J. Yessick, "Laser Material Processing," *Optical Engineering*, p. 203, May-June 1978.

[13] Conrad Banas, "High Power Laser Welding," *Optical Engineering*, p. 210, May-June 1978.

[14] Ref. [3], p. 858.

[15] J. G. Tweedale, *Welding Fabrication, Vol. I*, p. 71, American Elsevier Publishing Co., 1969.

[16] H. Udin, E. Funk, *Welding For Engineers*, p. 29, John Wiley & Sons Inc., 1954.

[17] John F. Radavich, "Superalloy 718 - A Look At The First 30 Years," *Journal of Metals*, p. 35, July 1988.

[18] S. D. Antolovich, J. E. Campbell, *Superalloy Source Book*, p. 166, ASM, 1984.

[19] F. R. Morral (editor), *Superalloy Source Book*, p. 22, ASM, 1984.

[20] C. T. Sims, W. C. Hagel (editors) *High Temperature Superalloys*, John Wiley & Sons Inc., 1987.

[21] E. Bayless, C.V. Lovoy, M. C. McIlwain, P. Munafo, *NASA TM-82409*, p. 3, March 1981.

[22] F. R. Morral (editor), *Superalloy Source Book*, p. 351, ASM, 1984.

[23] S. D. Antolovich, J. E. Campbell, *Superalloy Source Book*, p. 123, ASM, 1984.

[24] J. F. Barker, D. D. Kruger, D. R. Chang, *Advanced High Temperature Alloys*, p. 126, ASM, 1986.

[25] Private communications with Michael Sharp, Center For Laser Applications, University of Tennessee Space Institute.

[29] I. Miller, J. E. Fruend, *Probability And Statistics For Engineers*, p. 222, Prentice-Hall, Inc., 1985.

[30] Ref. [29], p491.

APPENDIXES

APPENDIX A

CO_2 LASERS

The word LASER is an acronym for Light Amplification by Stimulated Emission of Radiation. There are three fundamental requirements for the operation of all lasers. They are:

1. an active medium;
2. a population inversion;
3. optical feedback.

To understand how these requirements are combined to produce a working CO_2 laser requires a basic knowledge of molecular activity. All molecules undergo oscillation and have rotational and vibrational energy as a result of this motion. This energy exists at discrete levels. The CO_2 molecule has three different modes of vibrational oscillation.

Quantum theory states that the energy of oscillation of a molecule in any given mode can have only discrete values which are integer multiples of a fundamental value. At any given instant, the CO_2 molecules can be vibrating in any linear combination of these fundamental modes. The resulting energy state is represented by the numbers (ijk). These numbers represent the number of energy quanta associated with each of the three fundamental vibrational modes of the molecules; symmetric stretch (v_1), bend (v_2), and asymmetric stretch (v_3).

If a sufficient number of CO_2 molecules are excited to the high energy state (002) and allowed to decay to the metastable energy state (001), and these metastable molecules exist in greater quantities than the molecules in the energy states (100) and (020), a population inversion has been produced. As the excited molecules decay from the (001) state to the (100) and (020) state, they emit light with the wavelength of 10.6 μm and 9.6 μm respectively. The bulk of the light emitted by the CO_2 laser is at 10.6 μm.

To increase the output of the laser, the active medium, or gas mixture, is made up of approximately 10% CO_2, 40% N_2, and 50% He. Excitation of the N_2 molecules to the higher energy state equivilent to that of (002) of the CO_2 molecule requires less energy input than required for the excitation of the CO_2 molecules. The energy is then transferred from the N_2 molecules to the CO_2 molecules by resonant collisions. This improves the output of the laser by reducing the power input. The helium is used to accelerate the transition from the (100) level to the ground state to maintain the population inversion.

The light that is emitted for a certain transition is all of the same wavelength. Some of the light passes out through the walls of the laser cavity and is lost. The remaining light that impinges upon the ends of the cavity is almost totally reflected by the rear mirror and approximately 85% reflected by the front mirror. The 15% transmitted light which passes through the front mirror forms the coherent light beam used for welding. That light which was reflected internally acts to induce emission from other CO_2 molecules within the laser cavity. This forms the optical feedback.

The configuration of the mirrors and any limiting apertures determines the cross sectional shape of the output beam. The resulting TEM or transverse electromagnetic mode of the beam, in turn, determines the ultimate usefulness of the laser. The TEM_{00} produces a spot with a Gaussian profile which can be focused to a minimum diameter yielding an extremely high power density at the surface. Other configurations of the beam exist and are shown in Figure A-1.

APPENDIX B

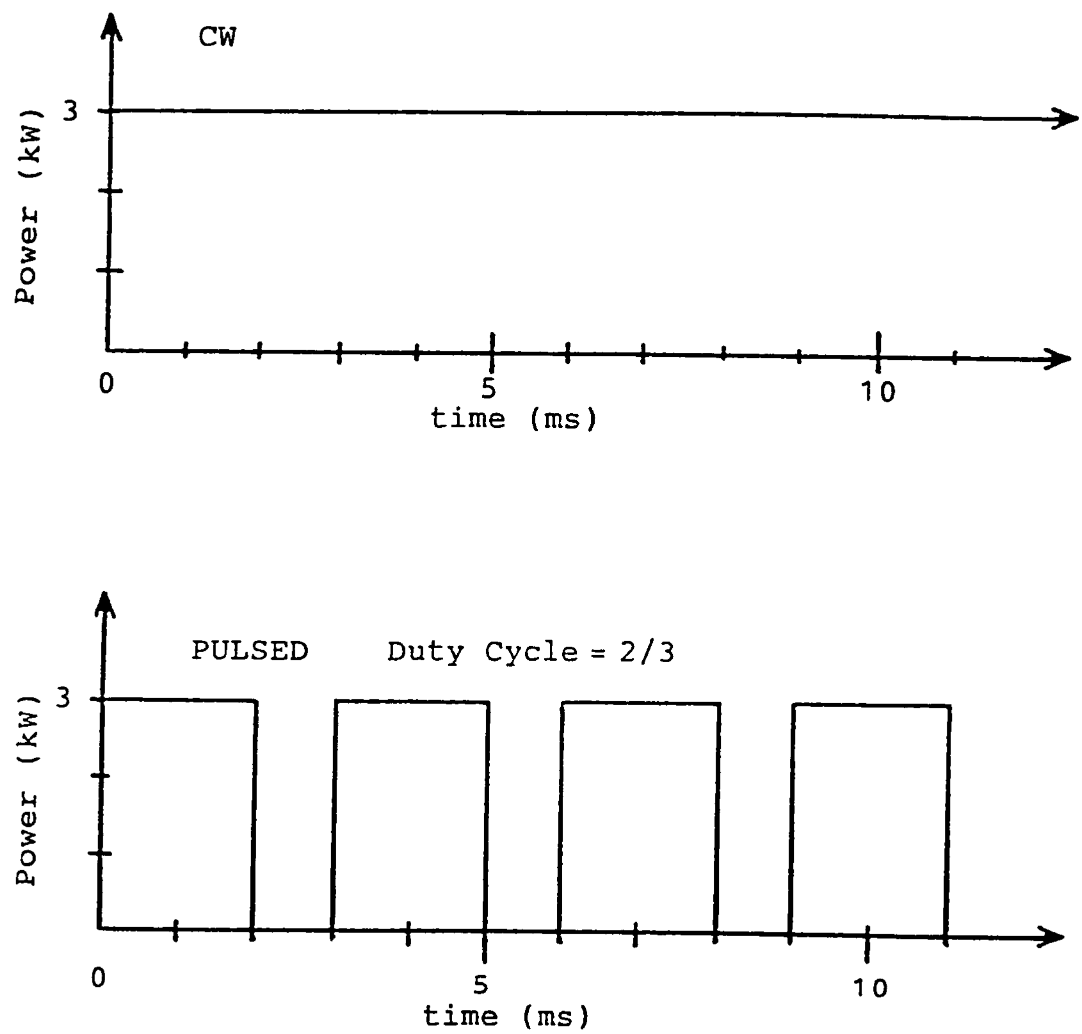

Figure II-1. Power versus time for an ideal CW laser (top graph) and power versus time for an ideal pulsed laser operating with a duty cycle of 2/3 (bottom graph).

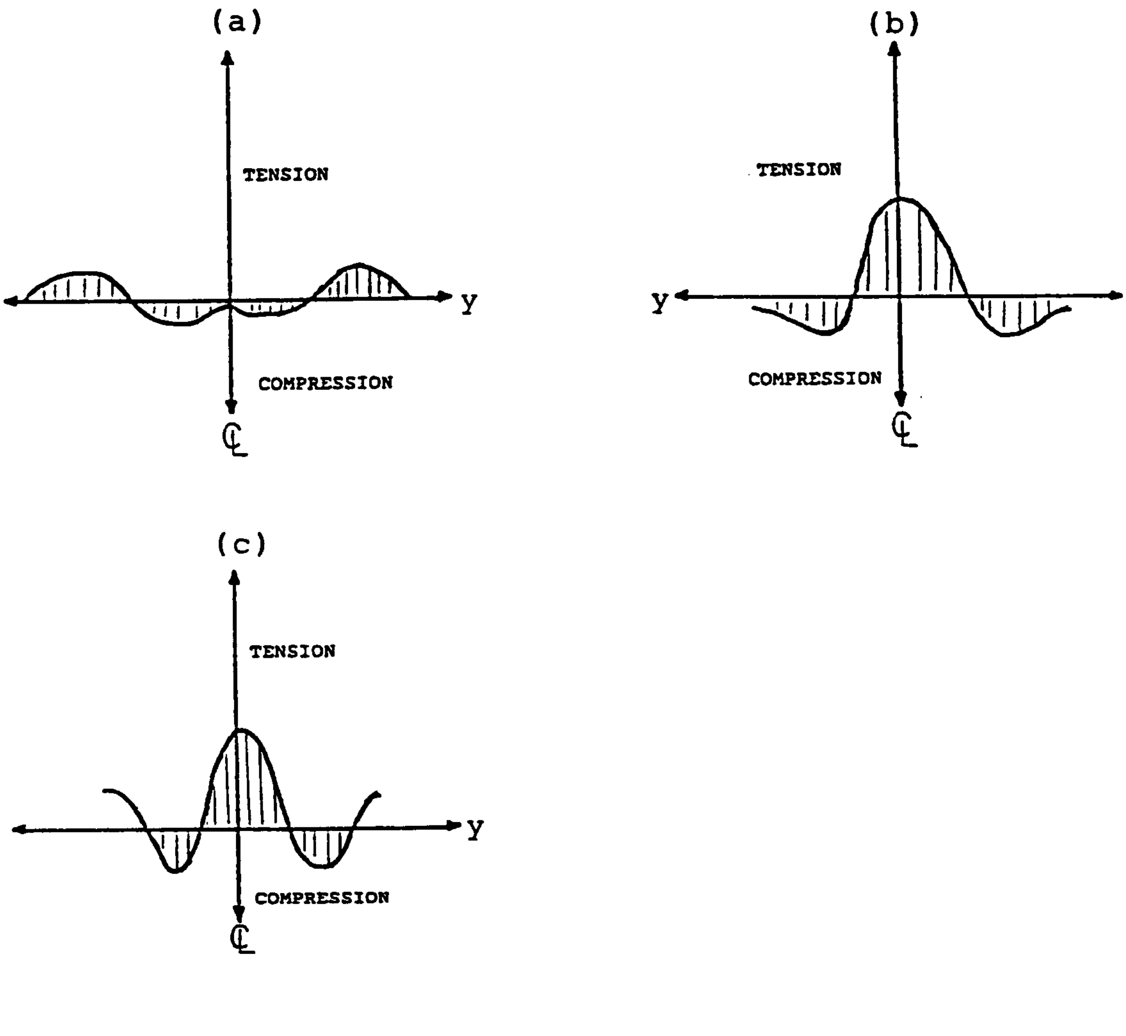

Figure II-2. Residual stresses in a weld as a function of distance from the weld pool center; (a) at point of heat input, (b) small distance behind heat input, (c) at point where weld is at ambient temperature [14].

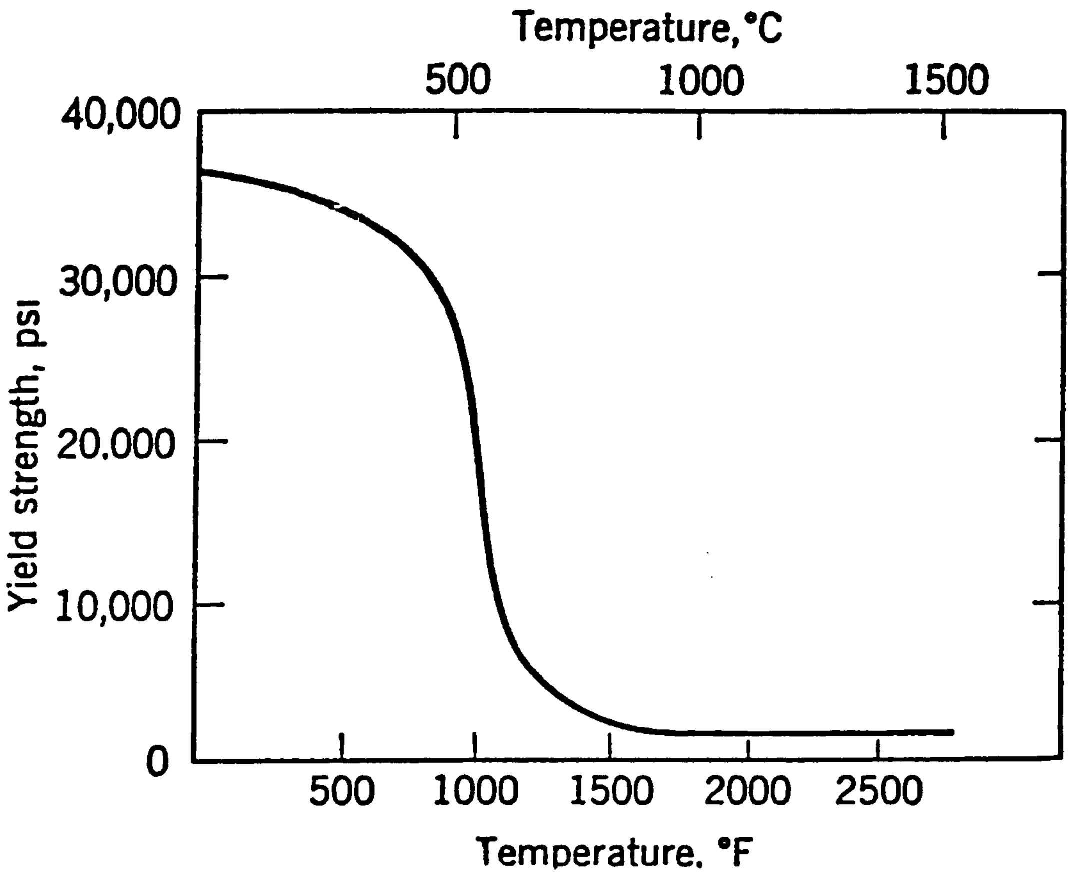

Figure II-3. Yield stress as a function of temperature for a typical structural steel [16].

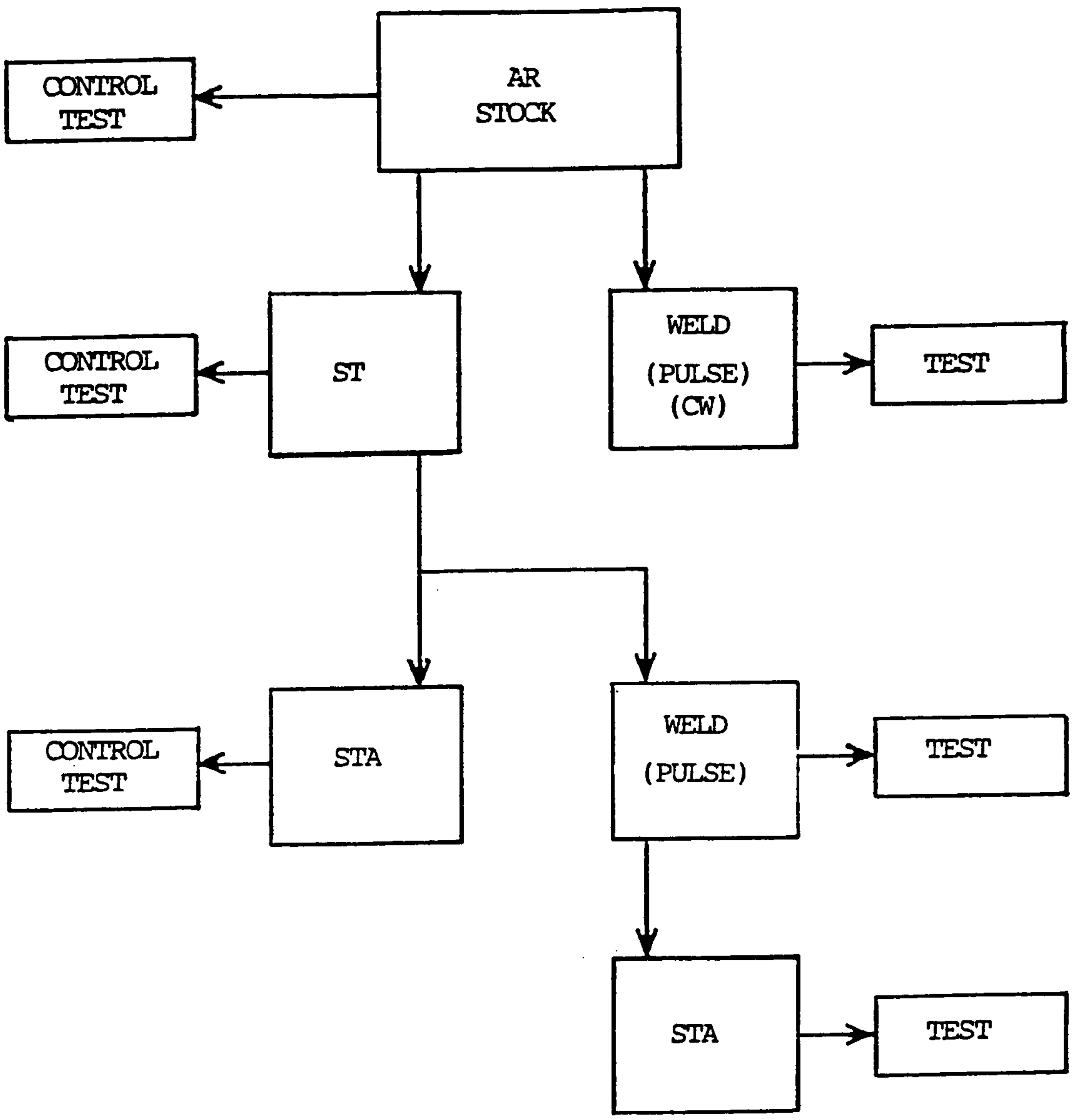

Figure III-1. Material process flow chart.

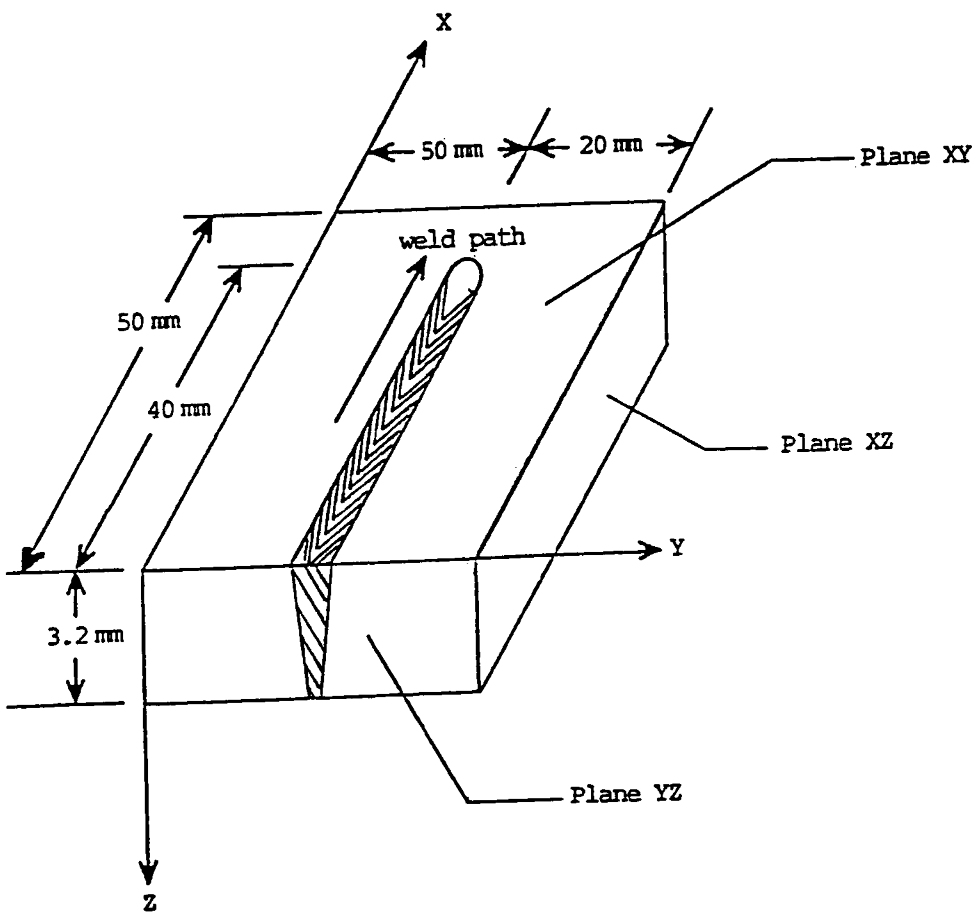

Figure III-2. Spatial orientation of welded parts showing part dimensions.

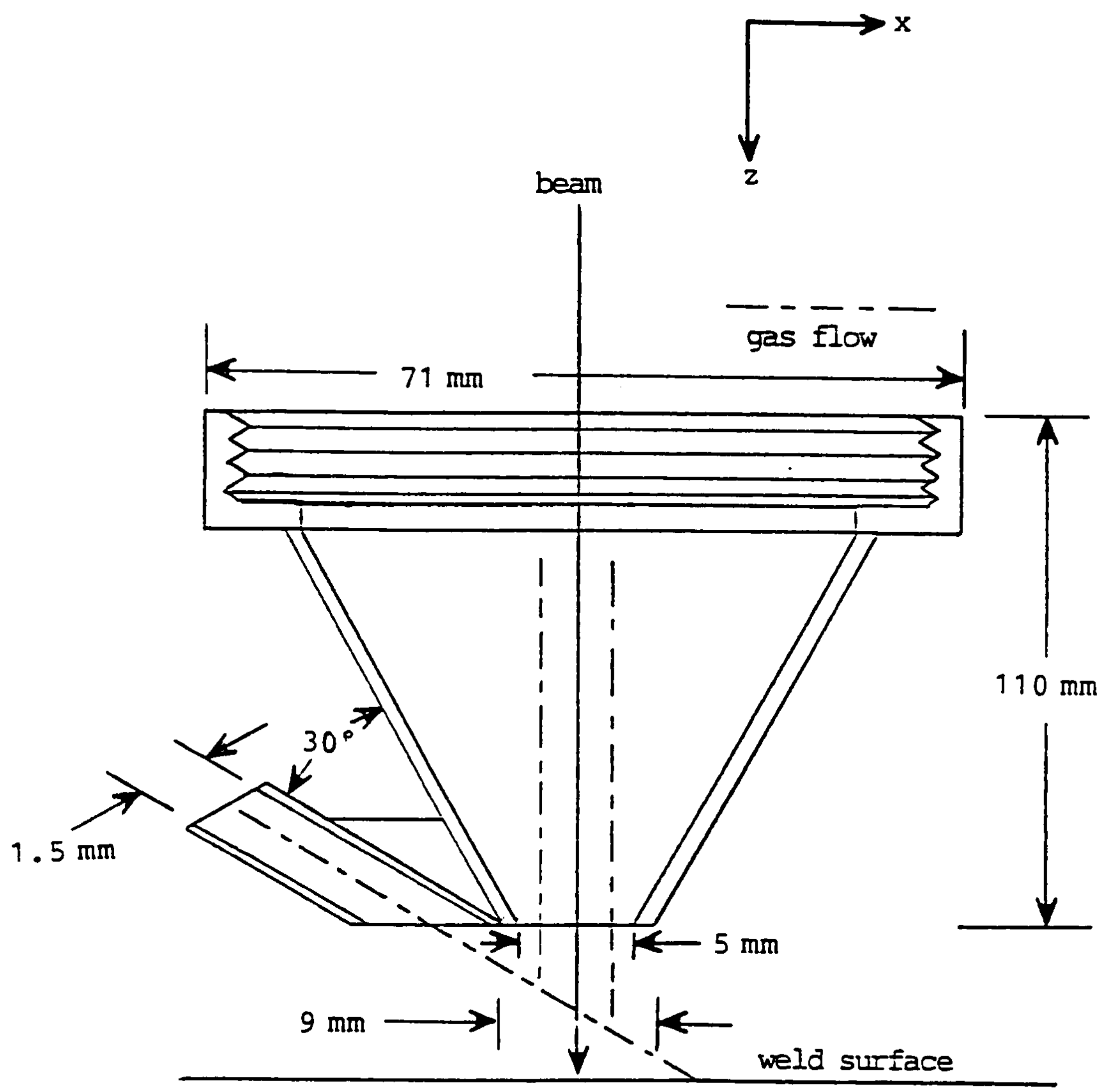

Figure III-3. Shield gas nozzle with plasma destruct jet.

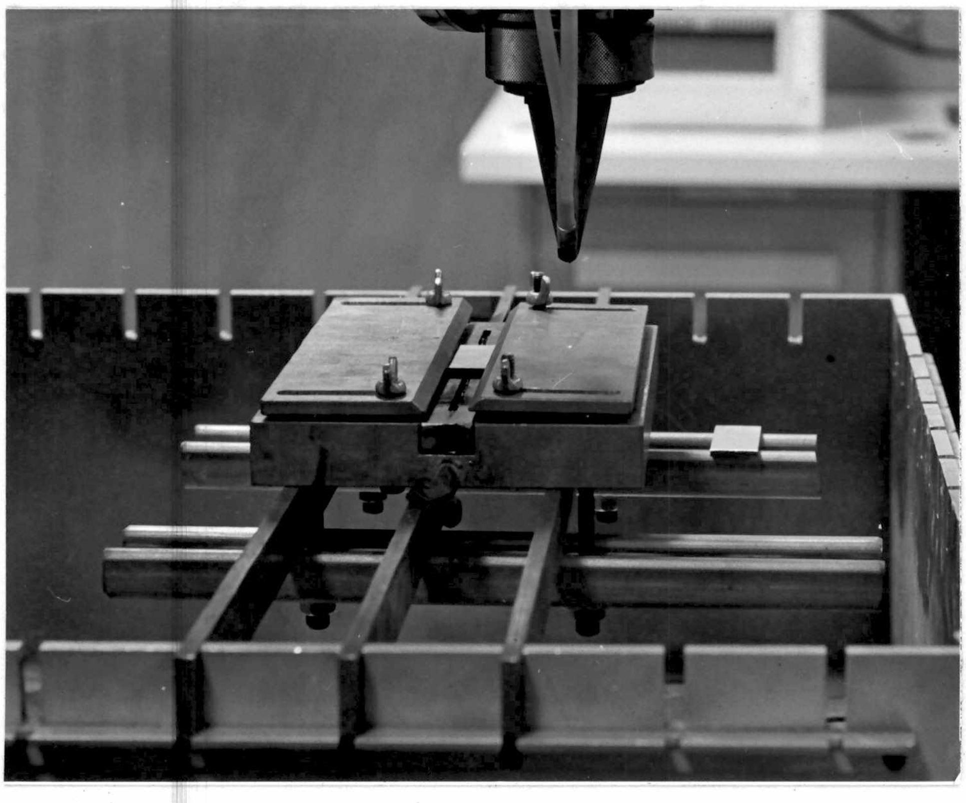

Figure III-4. Welding fixture used to secure samples during welding.

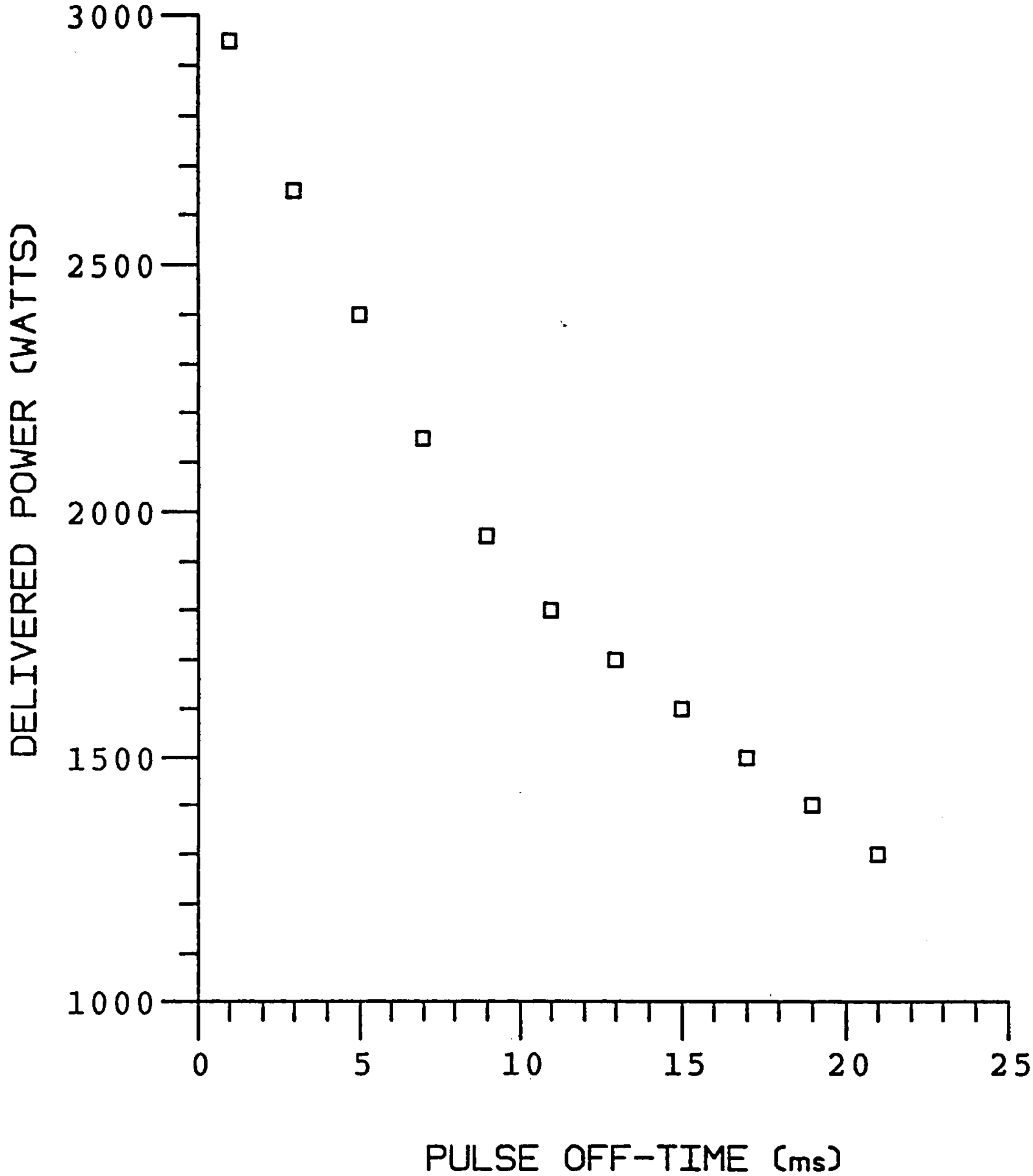

Figure III-5. Delivered power output of the Rofin-Sinar laser as a function of pulse off-time.

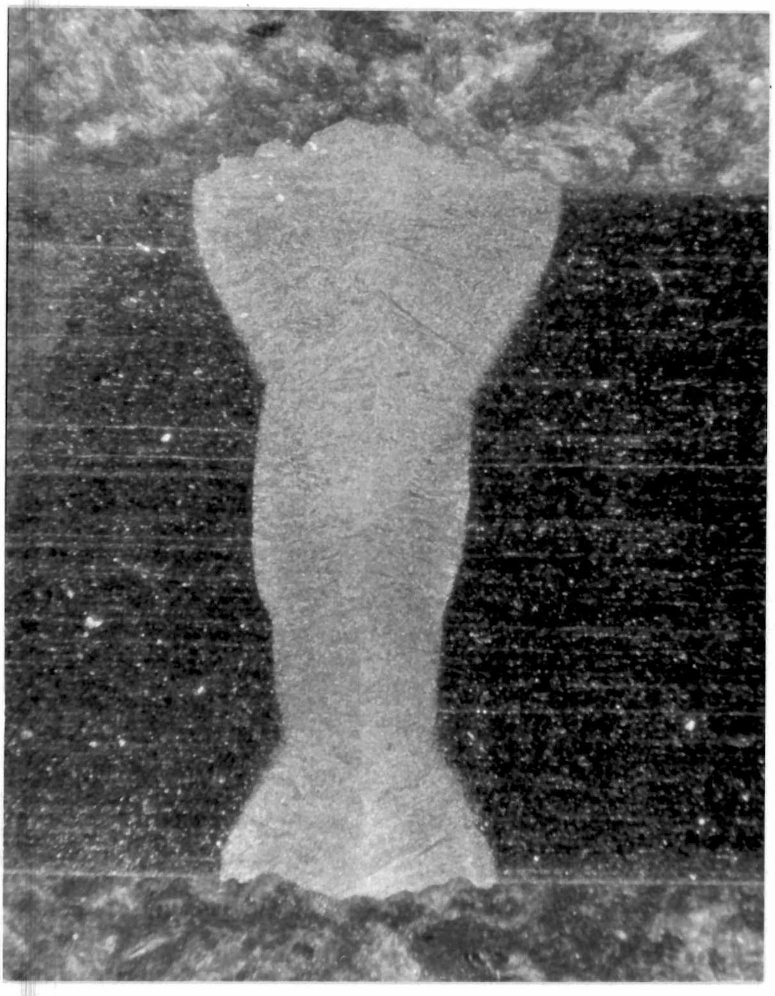

(a)

Figure III-6. YZ plane photographs of the AR pulse welded samples at 28X; (a) AR5, (b) AR7, (c) AR9, (d) AR11, (e) AR13, (f) AR15, (g) AR17, (h) AR19, (i) AR21.

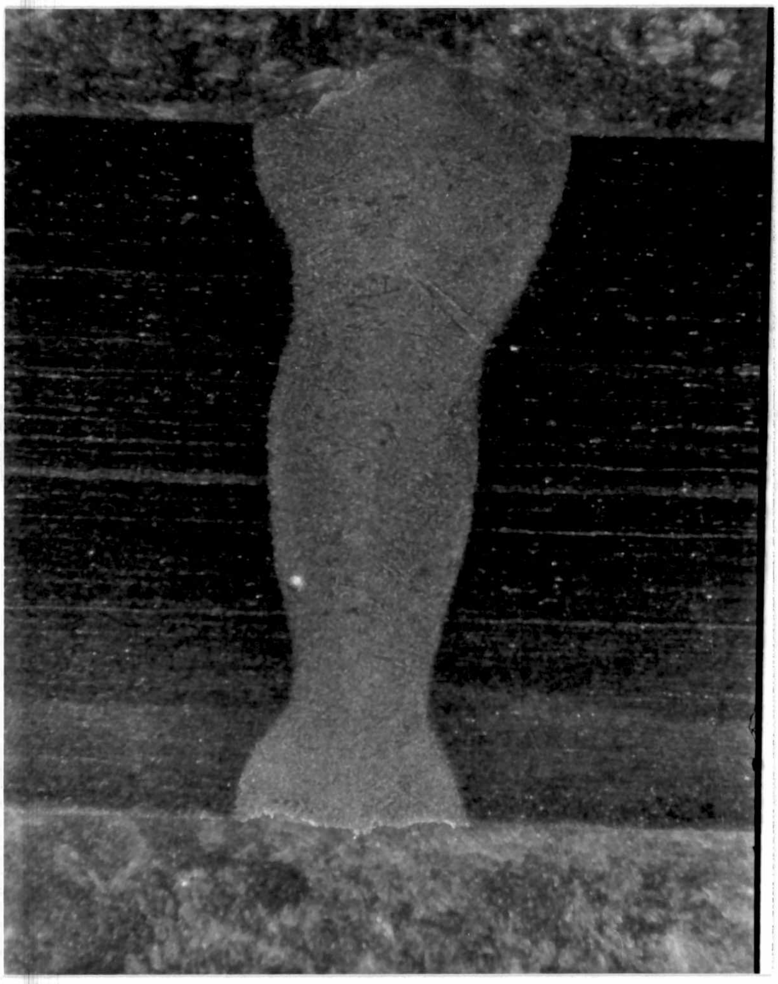

(b)

Figure III-6. (continued)

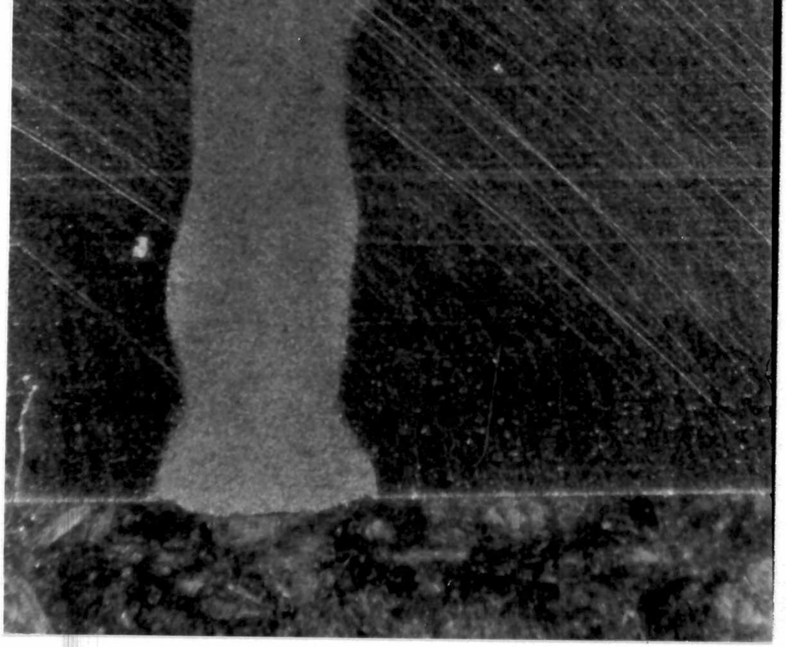

(c)

Figure III-6. (continued)

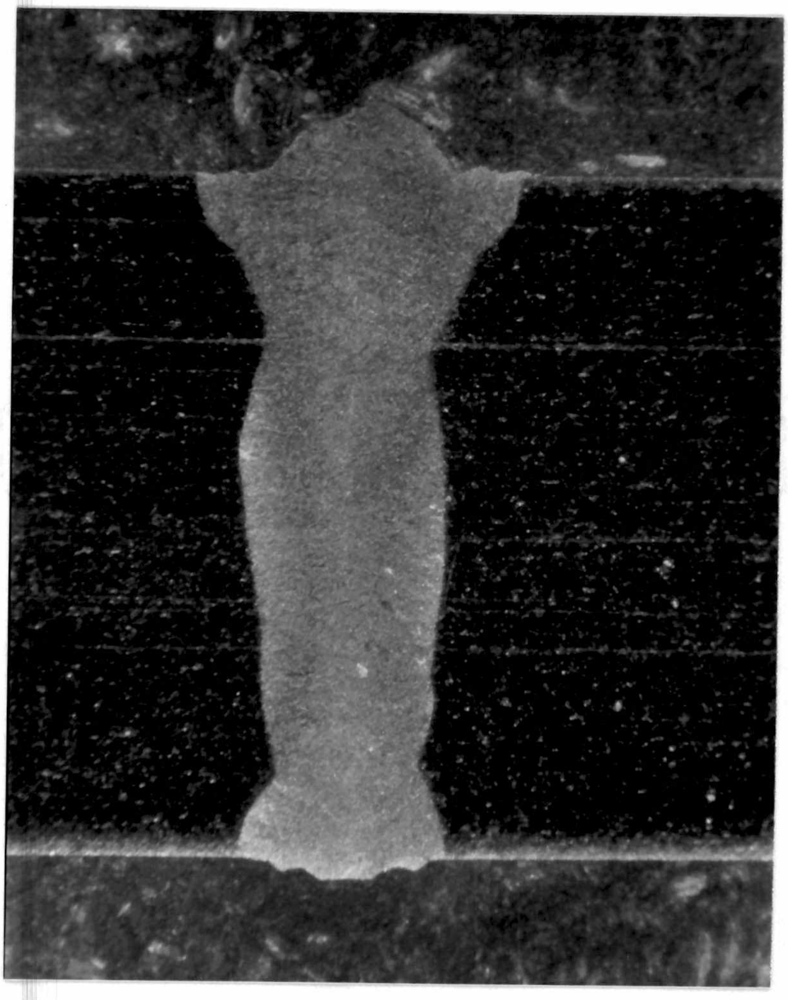

(d)

Figure III-6. (continued)

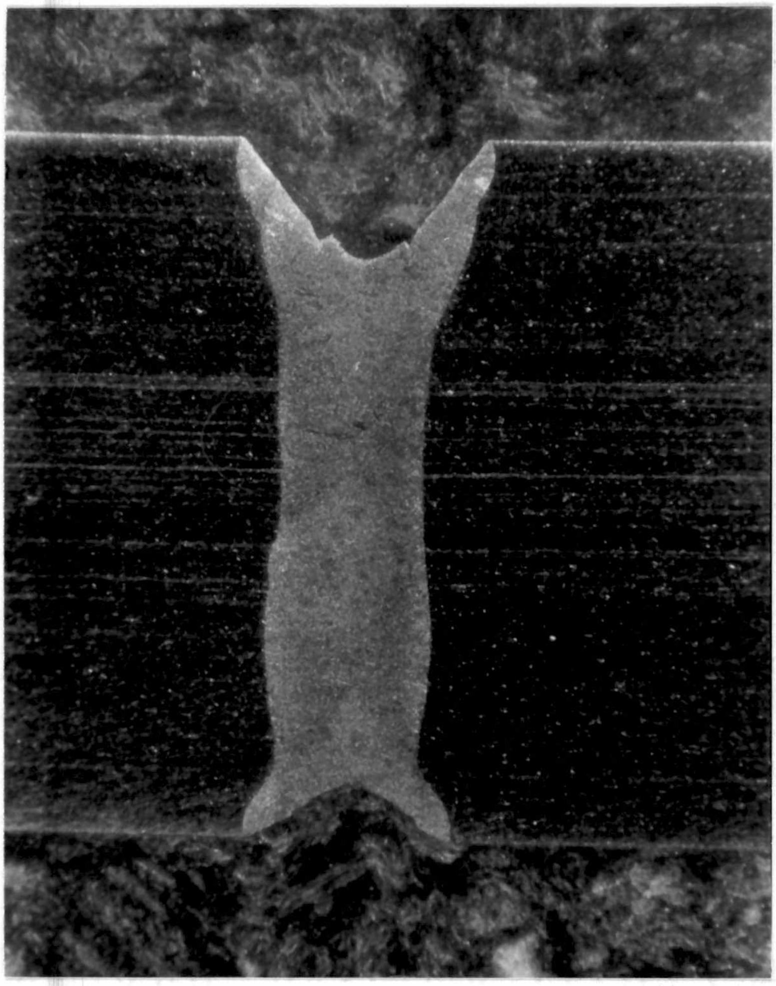

(e)

Figure III-6. (continued)

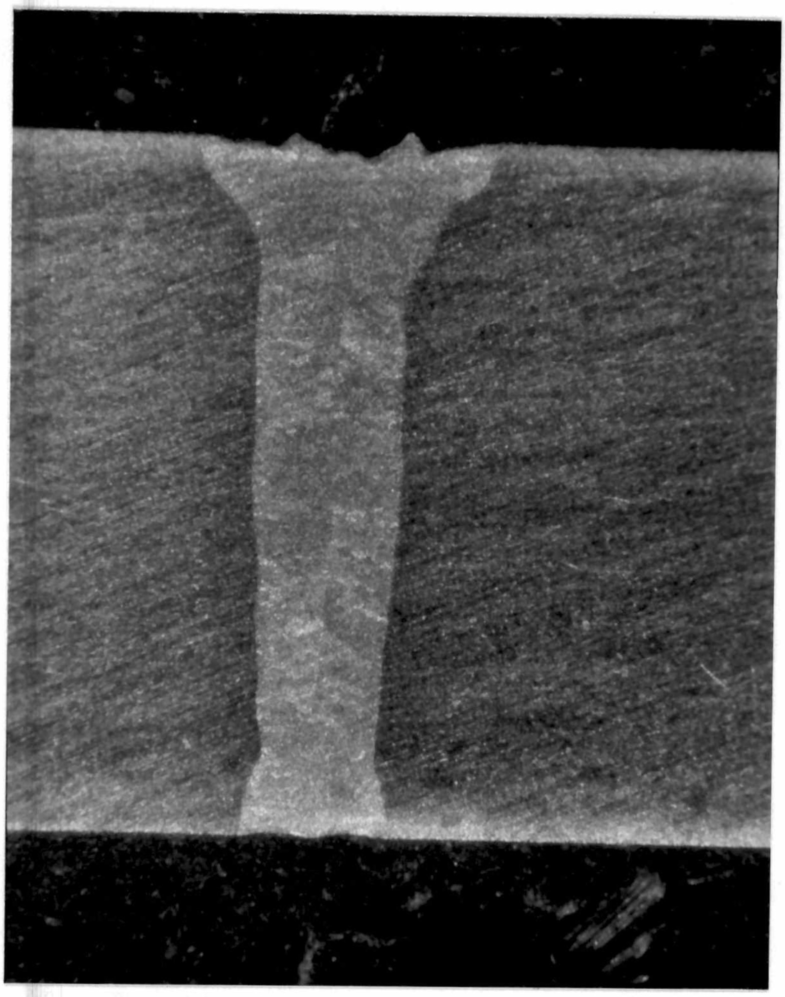

(f)

Figure III-6. (continued)

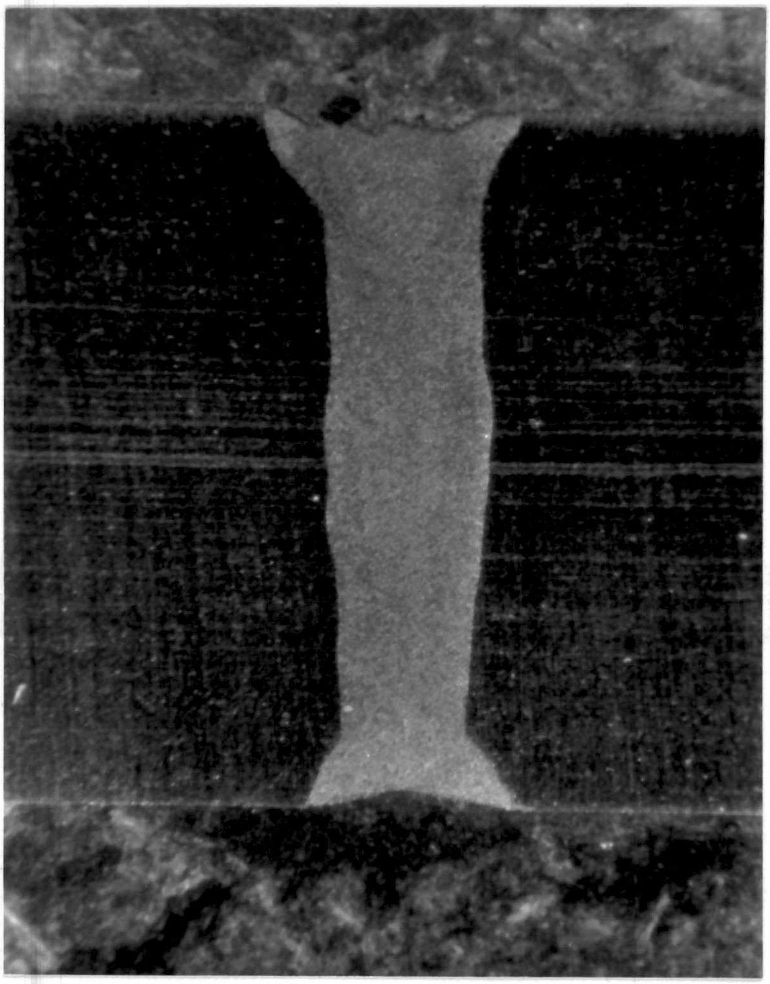

(g)

Figure III-6. (continued)

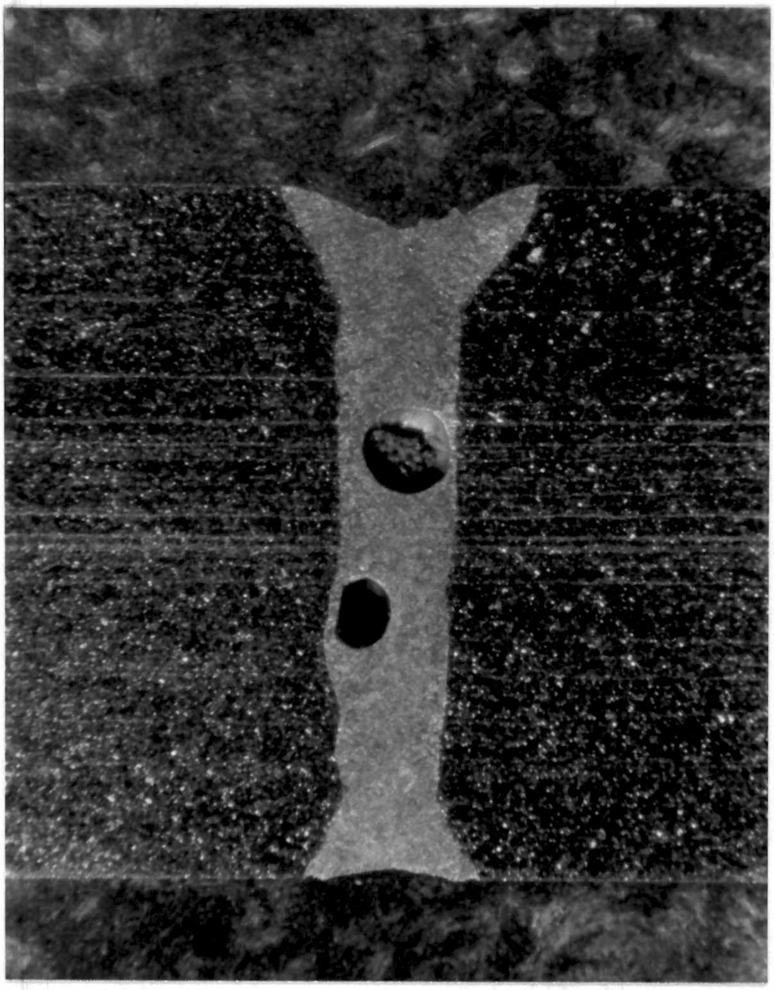

(h)

Figure III-6. (continued)

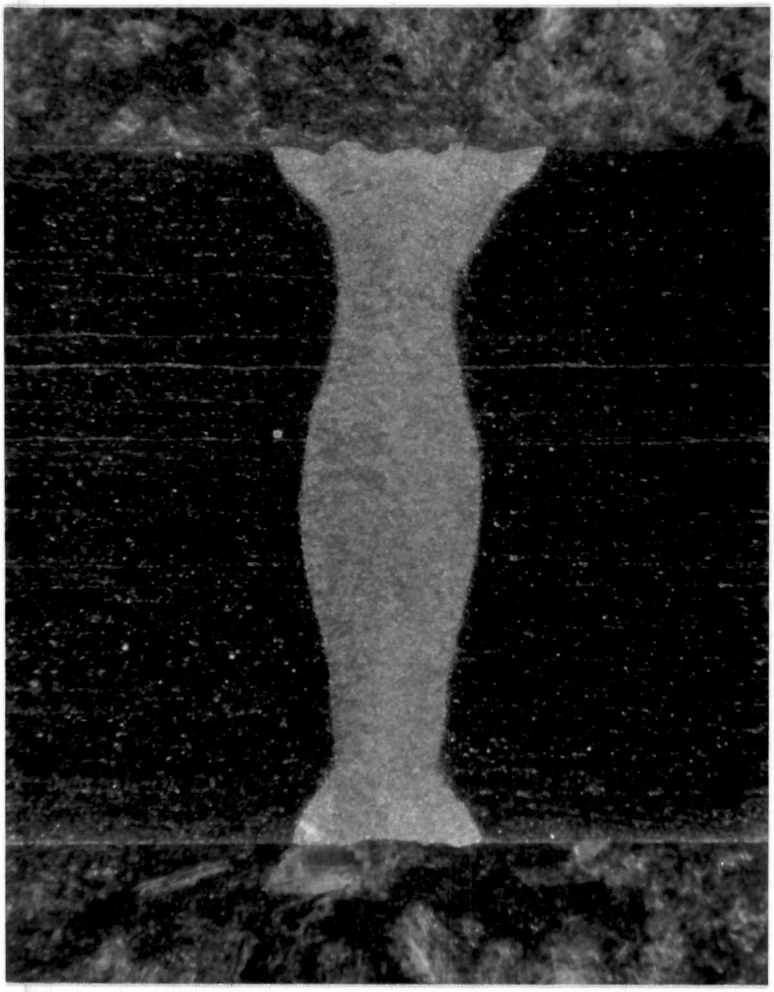

(i)

Figure III-6. (continued)

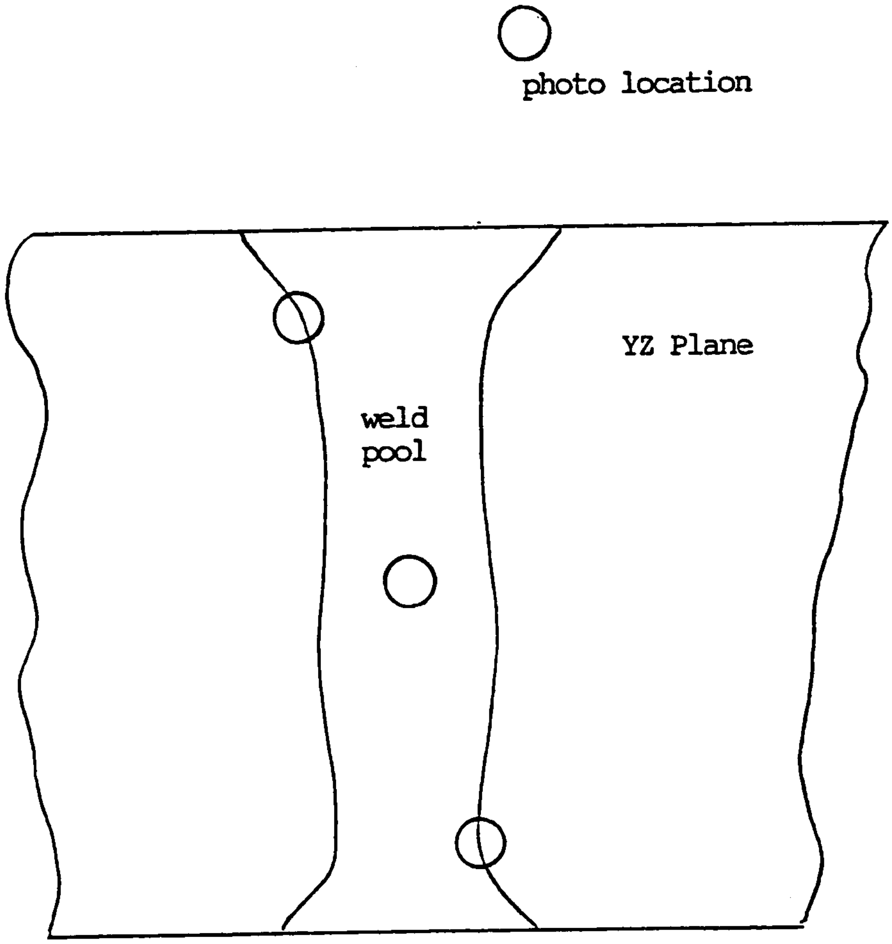

Figure III-7. Locations selected for high magnification photographs of the samples.

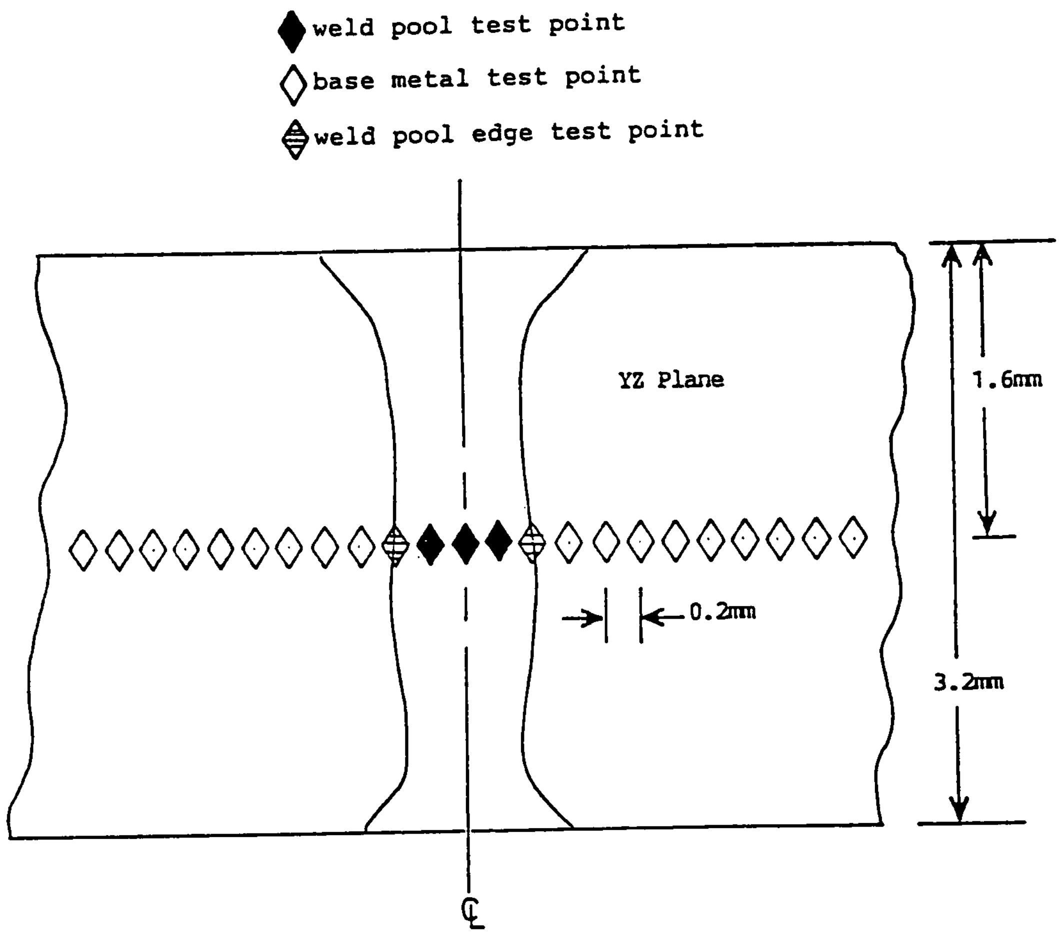

Figure III-8. Microhardness test point locations.

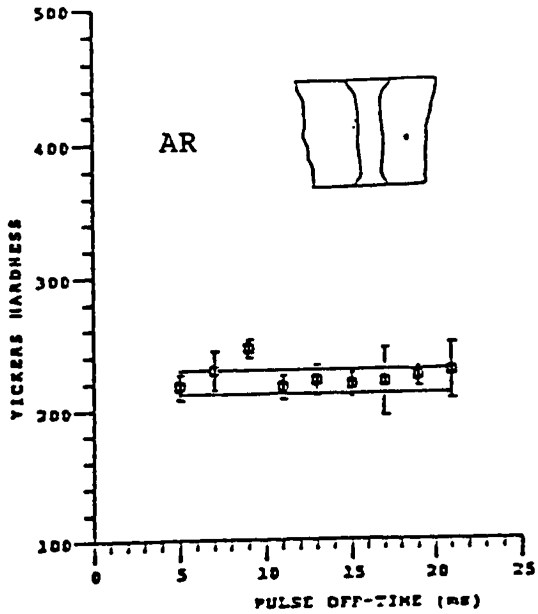

(a)

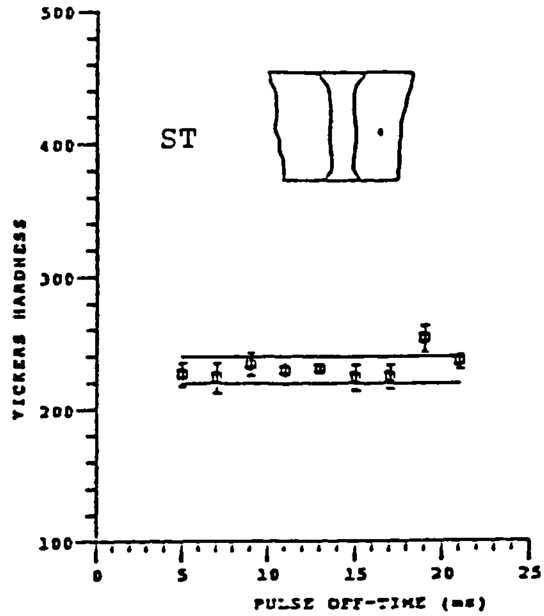

(b)

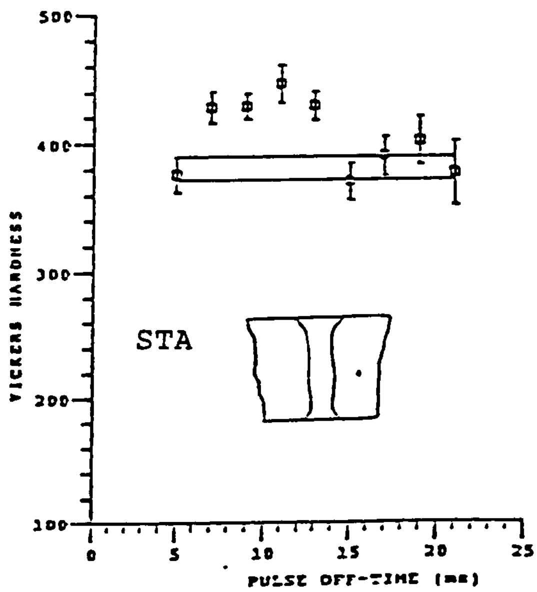

(c)

Figure IV-1. Average microhardness in the base metal region as a function of pulse off-time for the (a) AR, (b) ST, and (c) STA samples. Horizontal bars denote the range of microhardness in the control samples.

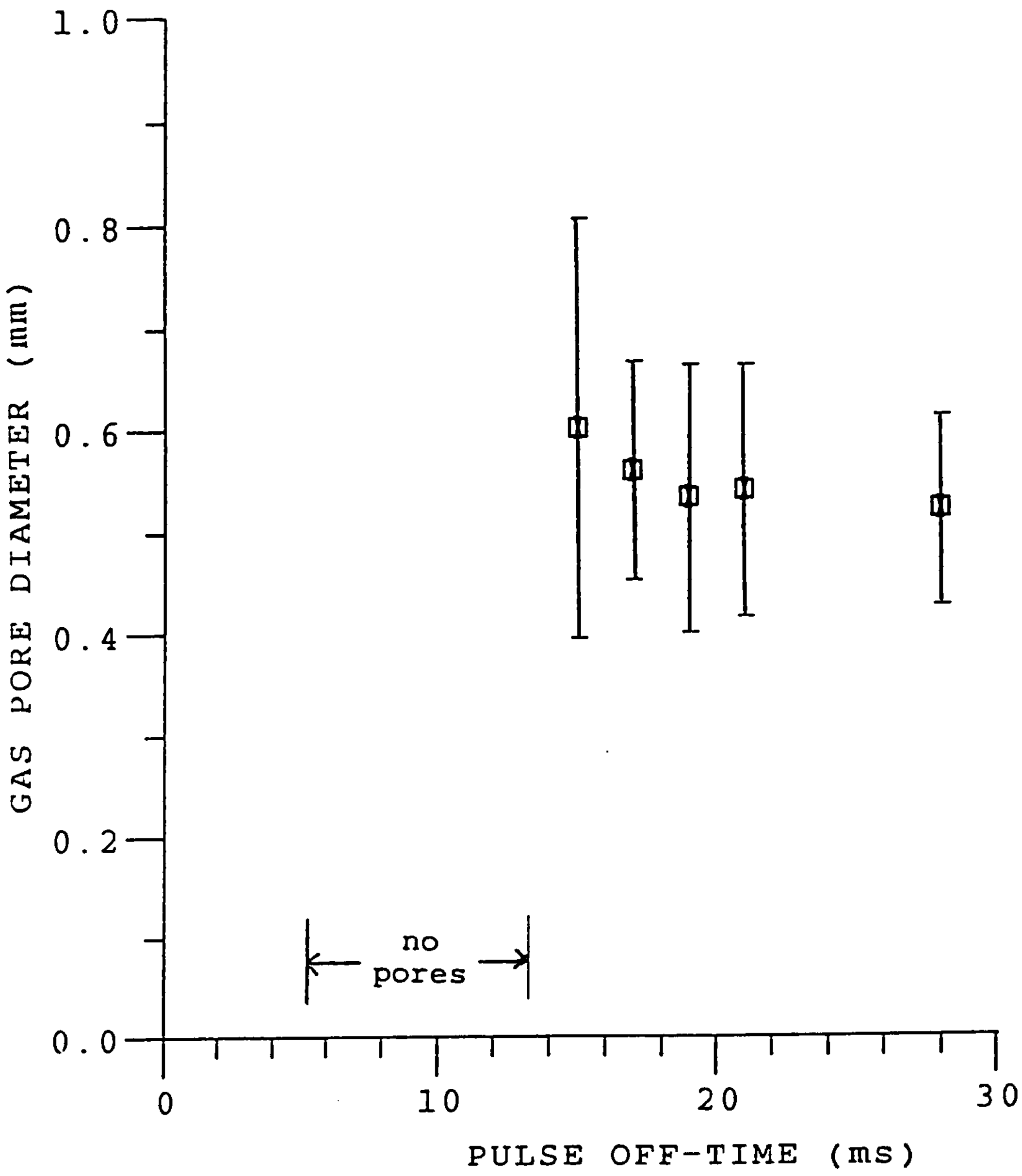

Figure IV-2. Pore diameter versus pulse off-time for the AR samples.

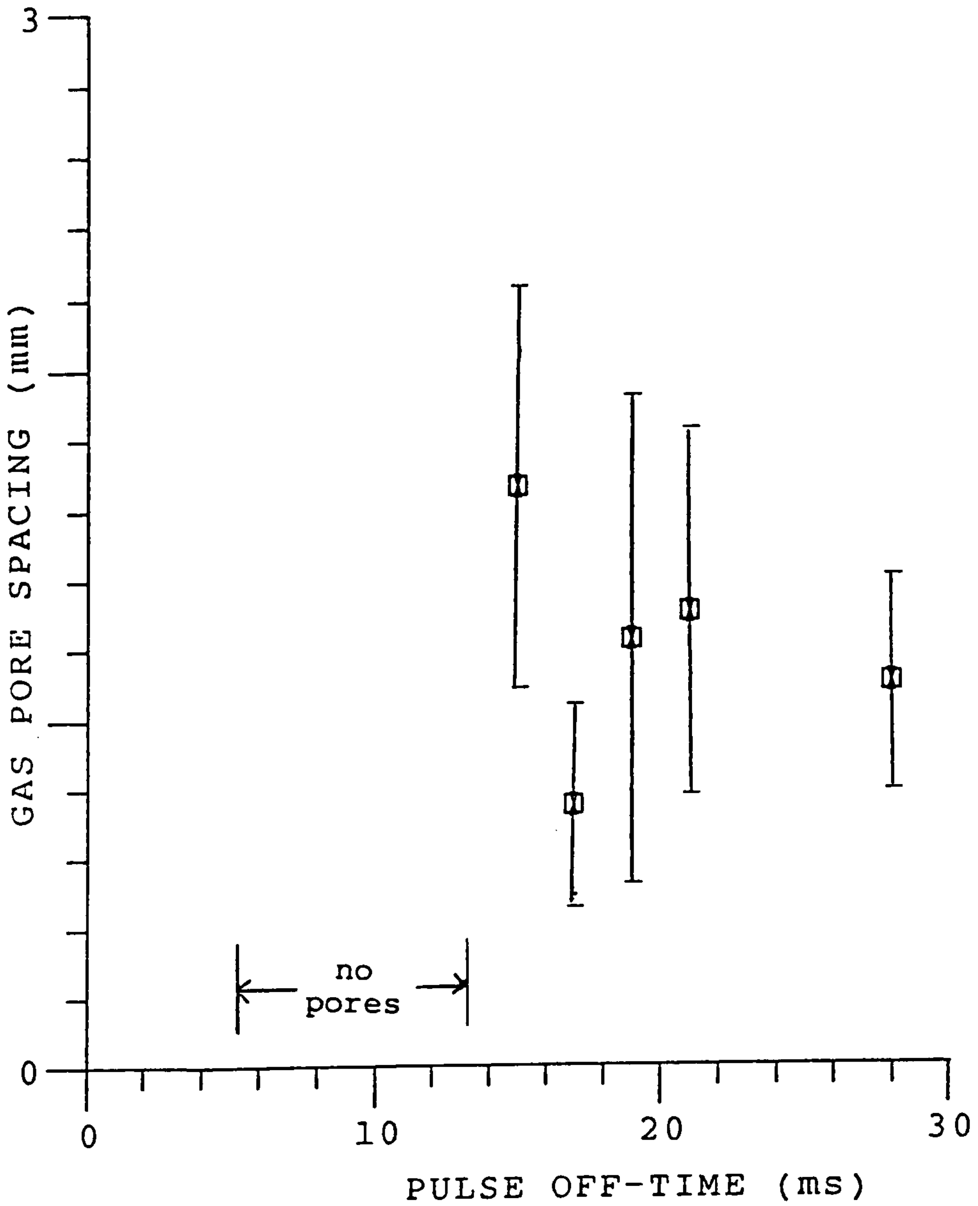

Figure IV-3. Pore spacing versus pulse off-time for the AR samples.

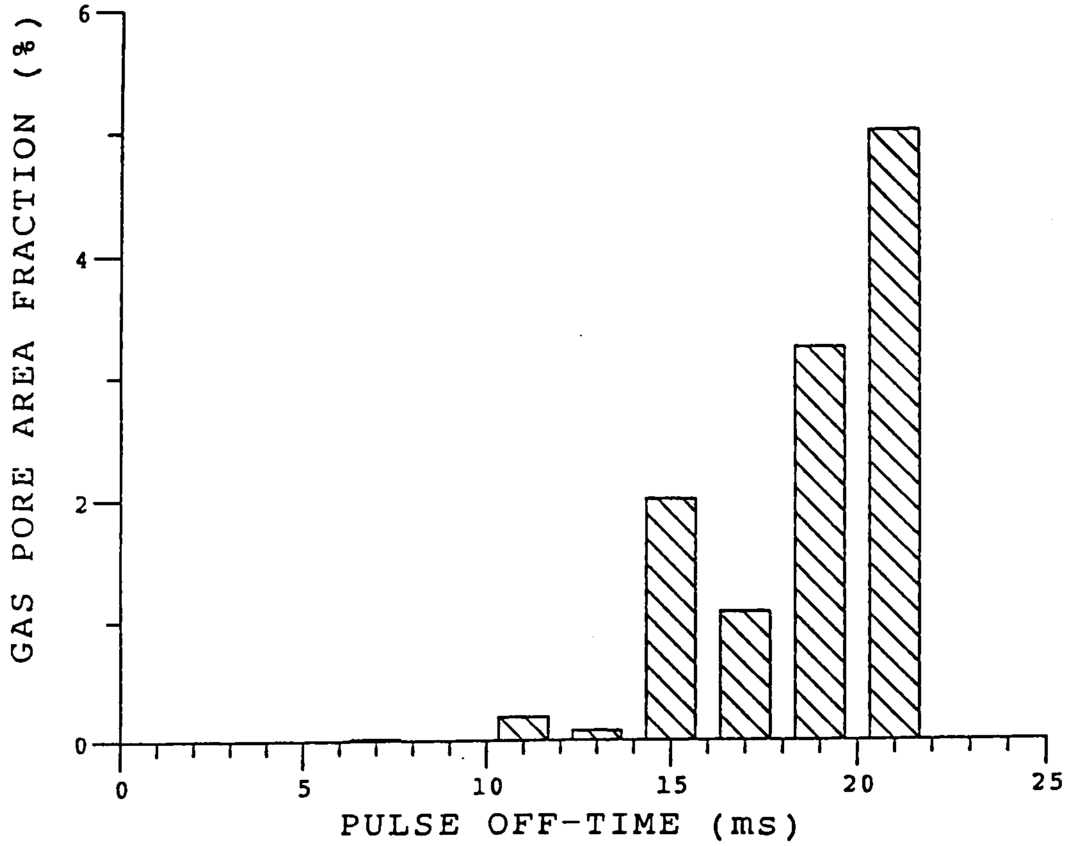

Figure IV-4. Pore area fraction % versus pulse off-time for the AR samples.

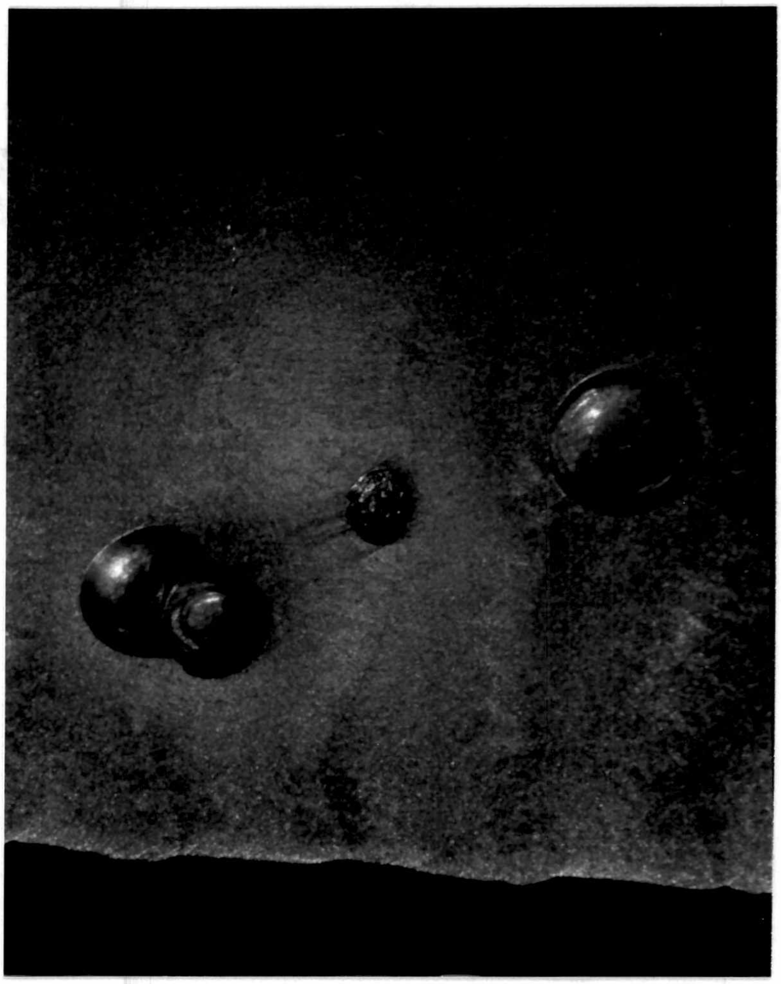

Figure IV-5. Pore growth by agglomeration in AR15 (28X).

(a)

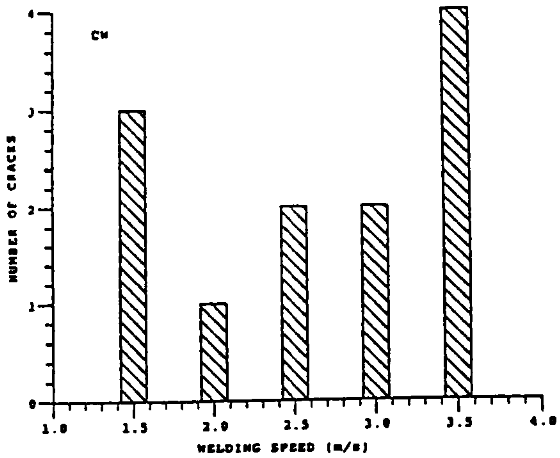

(b)

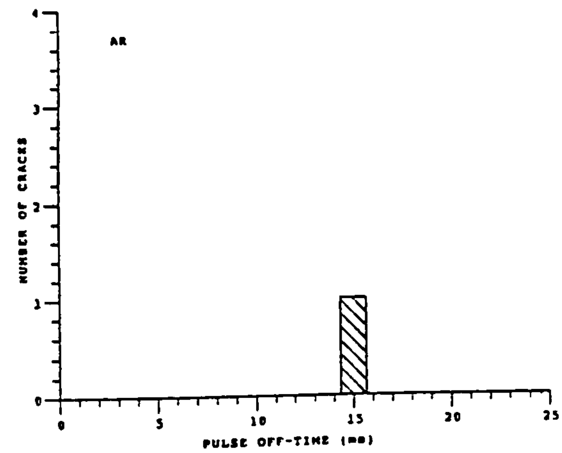

(c)

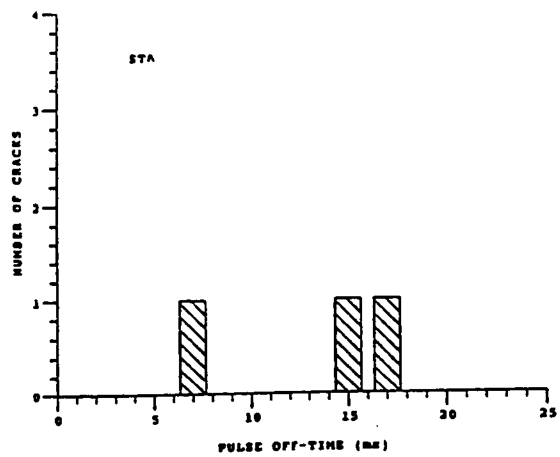

Figure IV-6. Number of microfissures versus welding speed for (a) CW samples and the number of microfissures versus pulse off-time for the (b) AR and (c) STA samples.

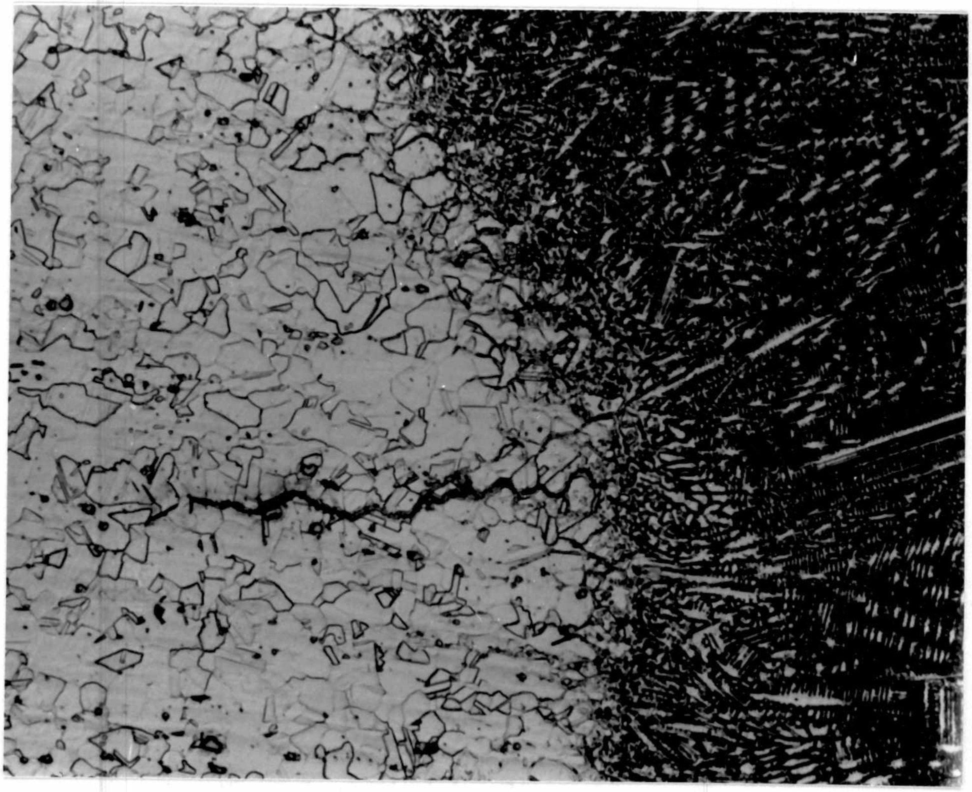

200X

Figure IV-7. Microfissure beneath the nailhead in sample CW3.5 at 200X and 800X.

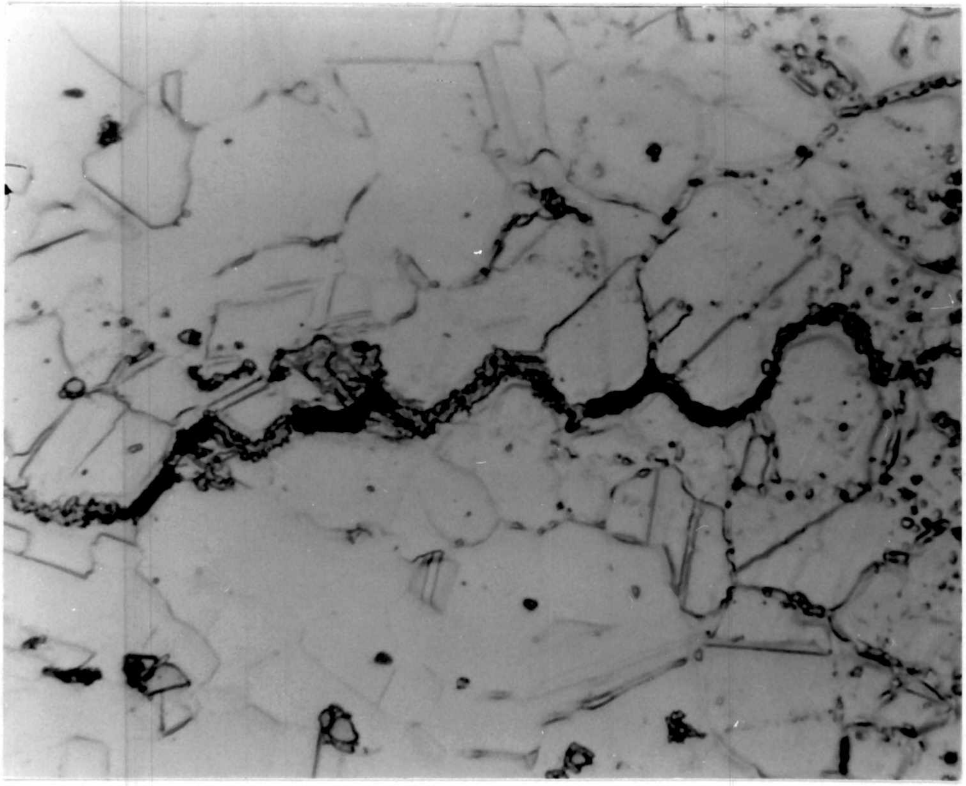

800X

Figure IV-7. (continued)

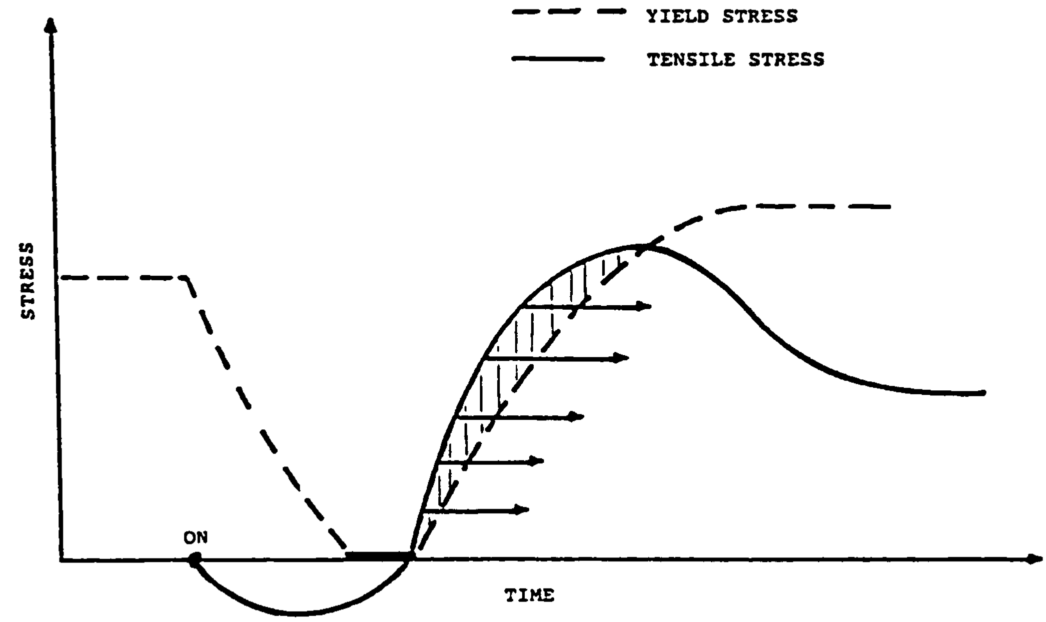

Figure IV-8. Yield strength versus time at temperature superimposed on yield strength versus time for a solidifying weld showing the region where microfissuring is likely to occur (shaded area).

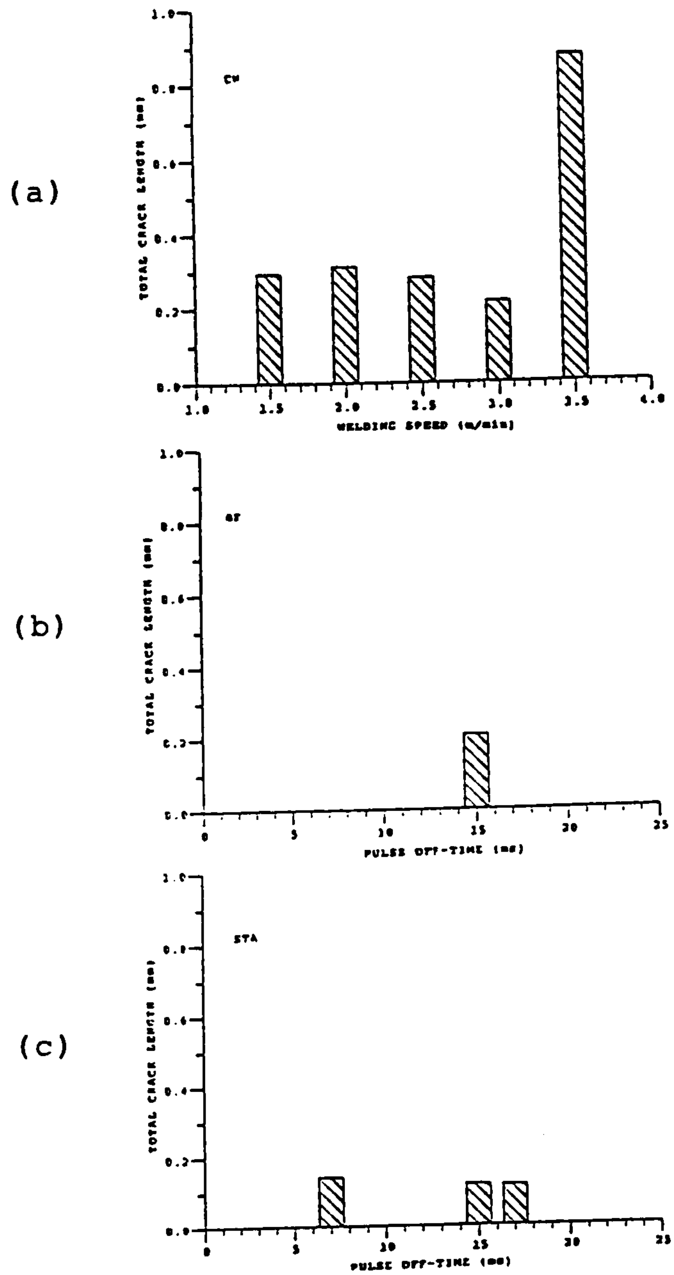

Figure IV-9. Total length of microfissure versus welding speed for the (a) CW samples and the total length of microfissure versus pulse off-time for the (b) AR and (c) STA samples.

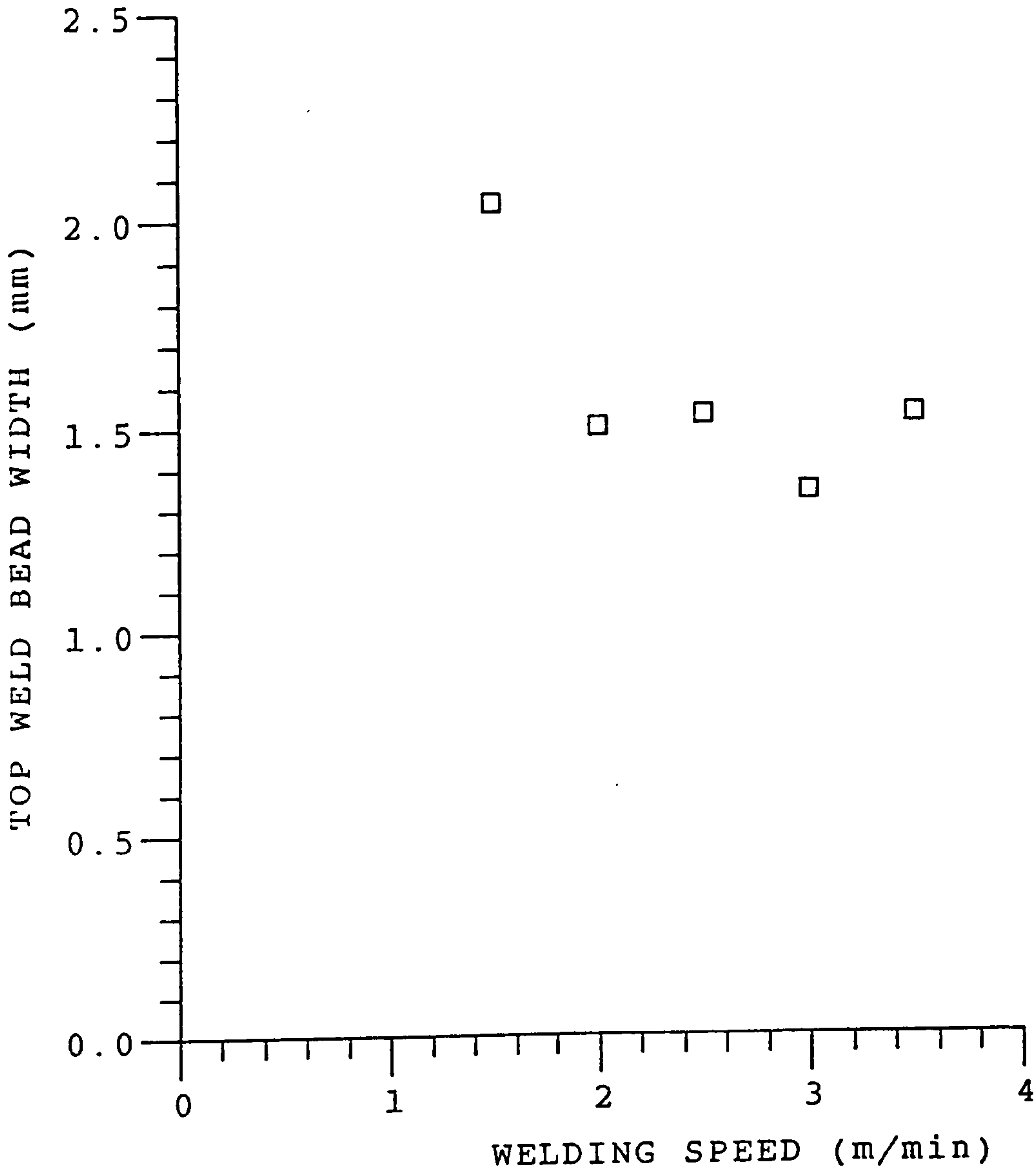

Figure IV-10. Top weld bead width versus welding speed for the CW samples.

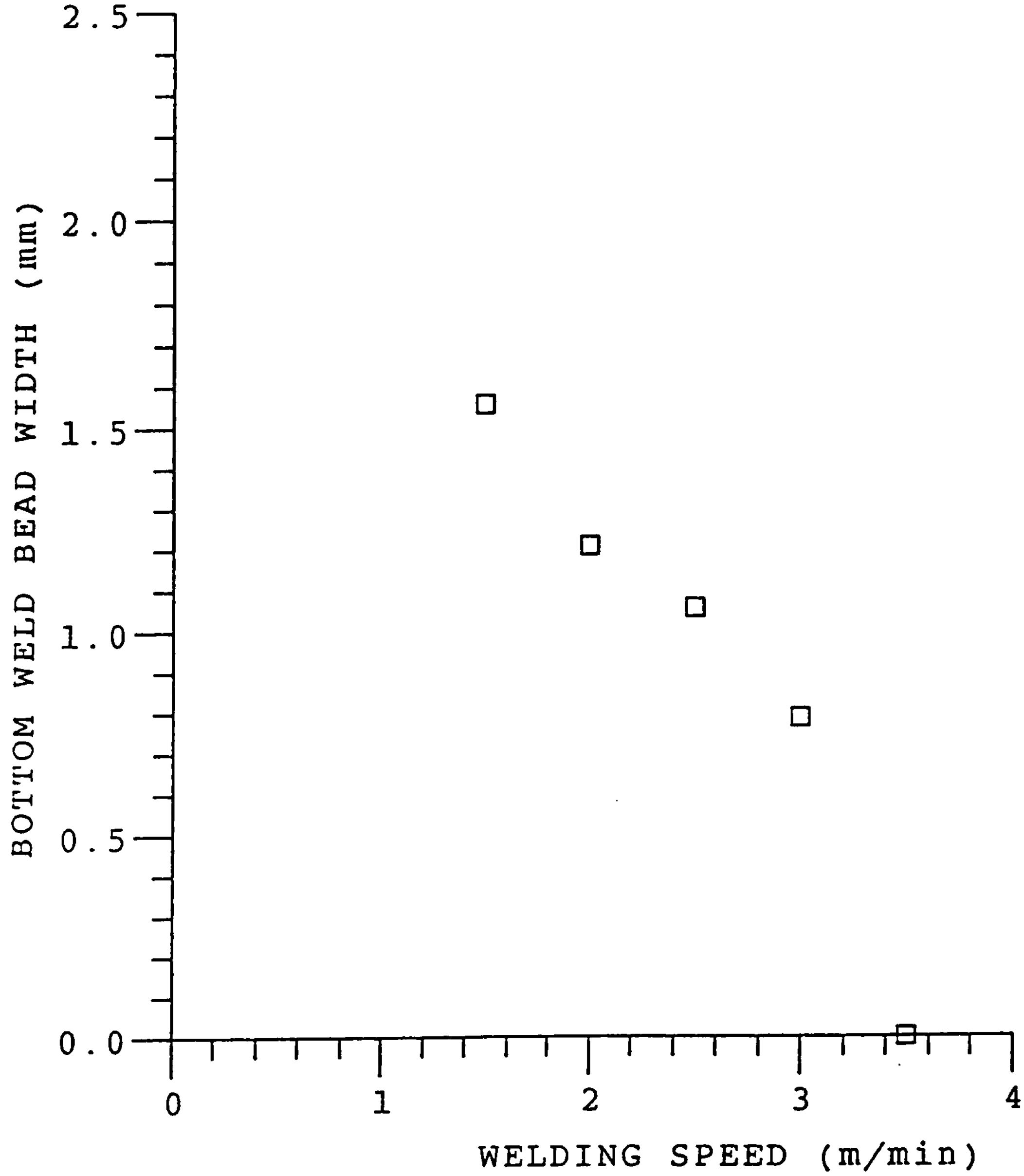

Figure IV-11. Bottom weld bead width versus welding speed for the CW samples.

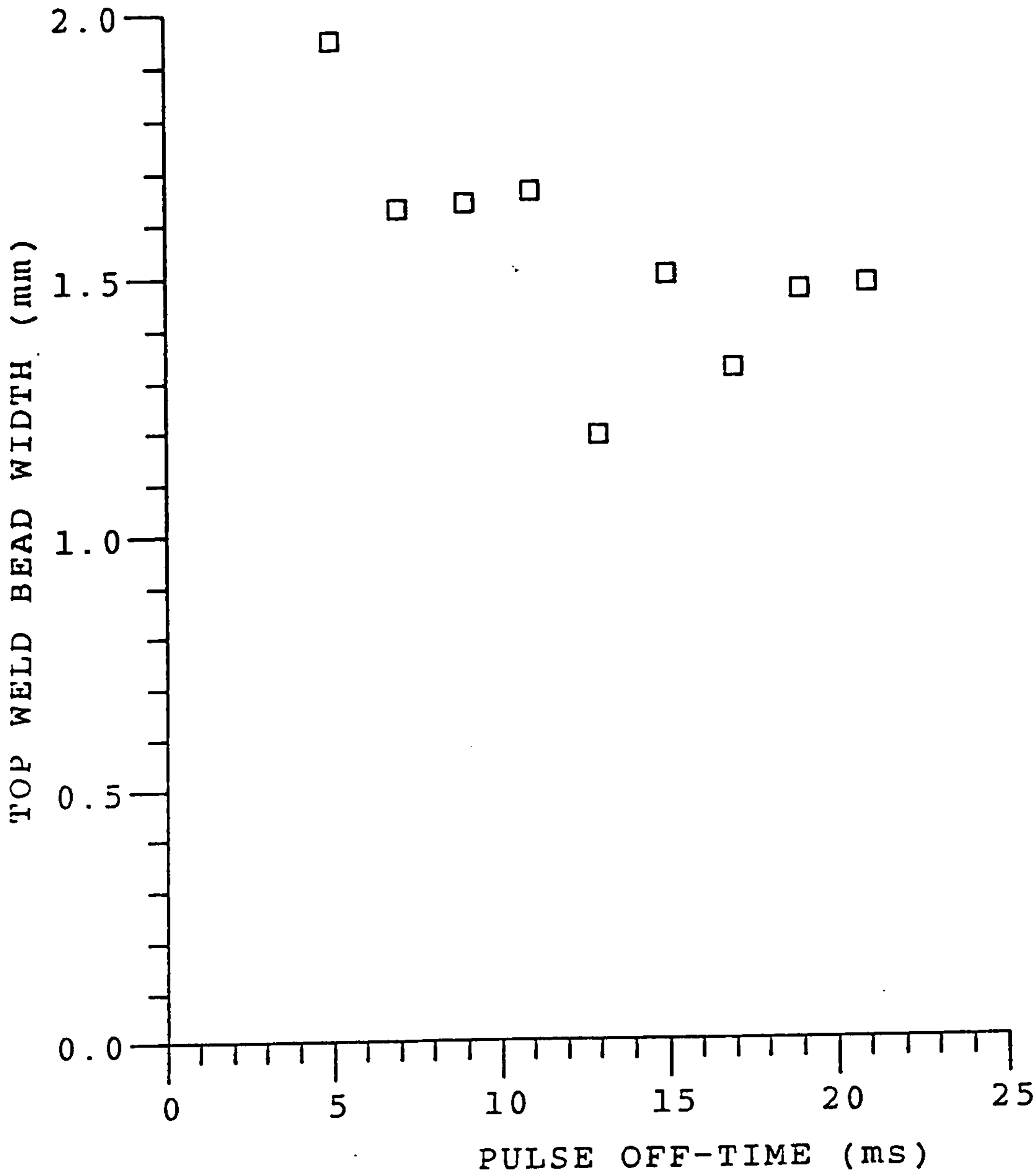

Figure IV-12. Top weld bead width versus pulse off-time for the AR samples.

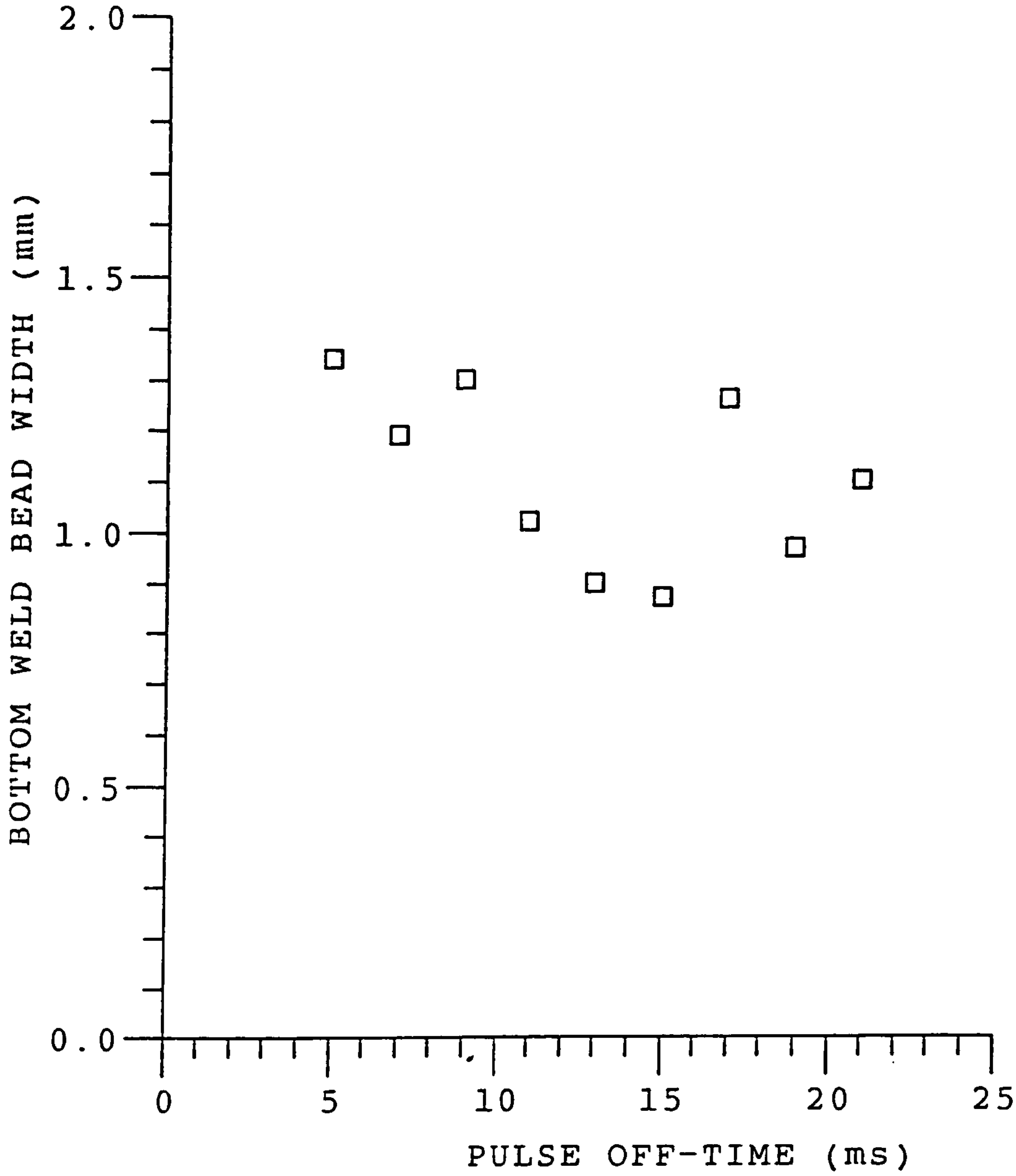

Figure IV-13. Bottom weld bead width versus pulse off-time for the AR samples.

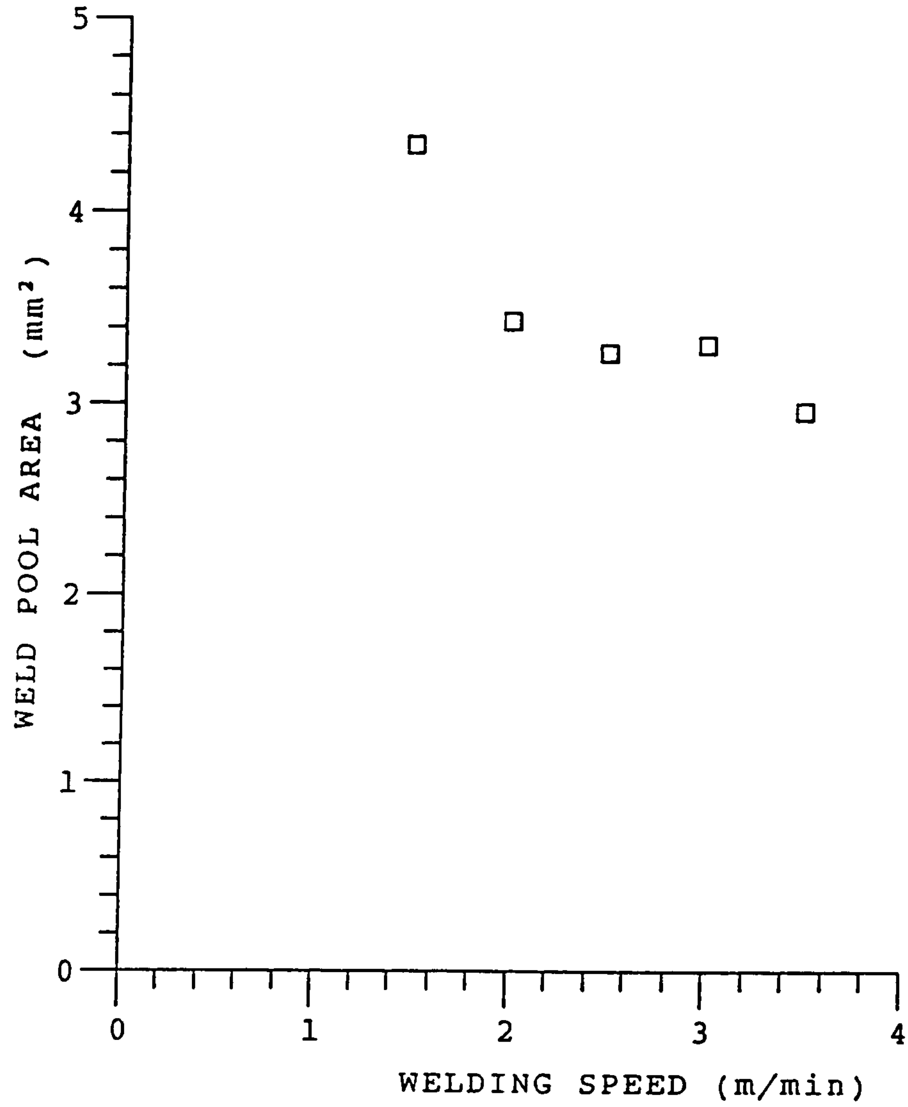

Figure IV-14. YZ plane area versus welding speed for the CW samples.

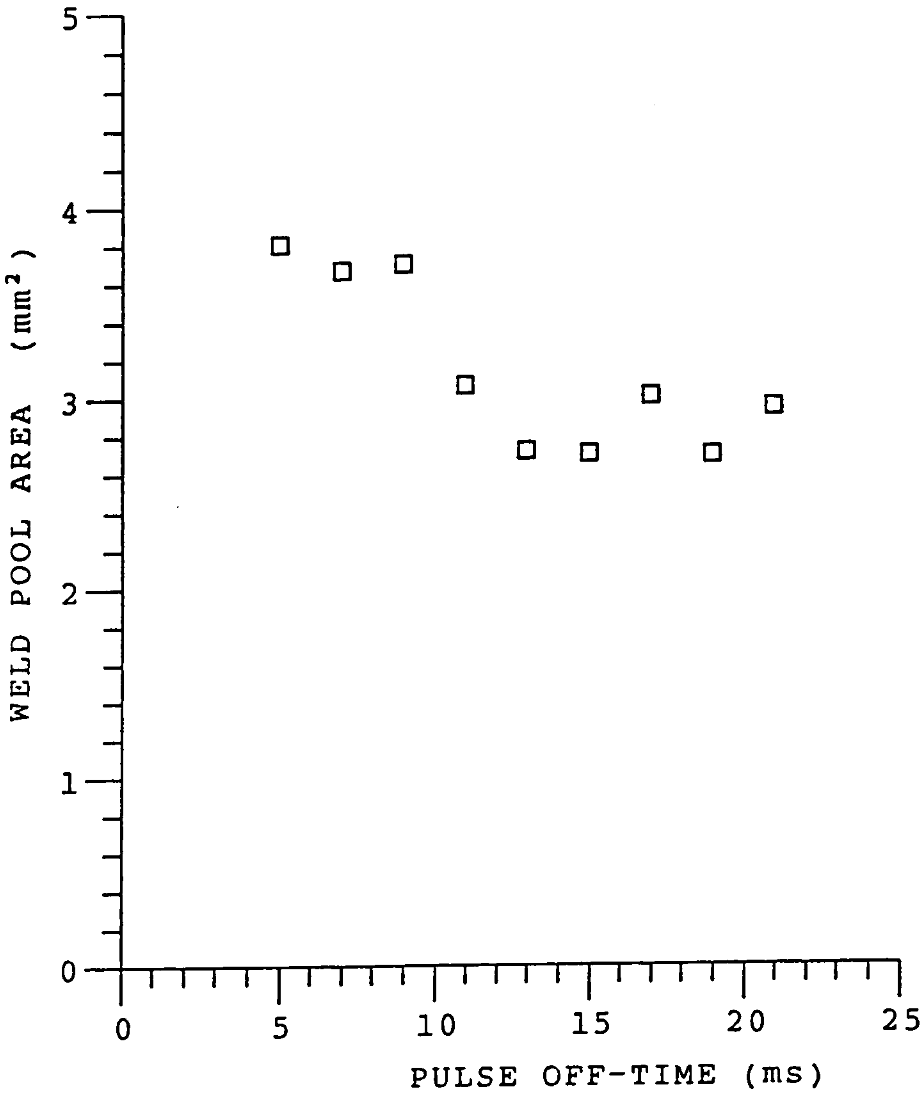

Figure IV-15. YZ plane area versus pulse off-time for the AR samples.

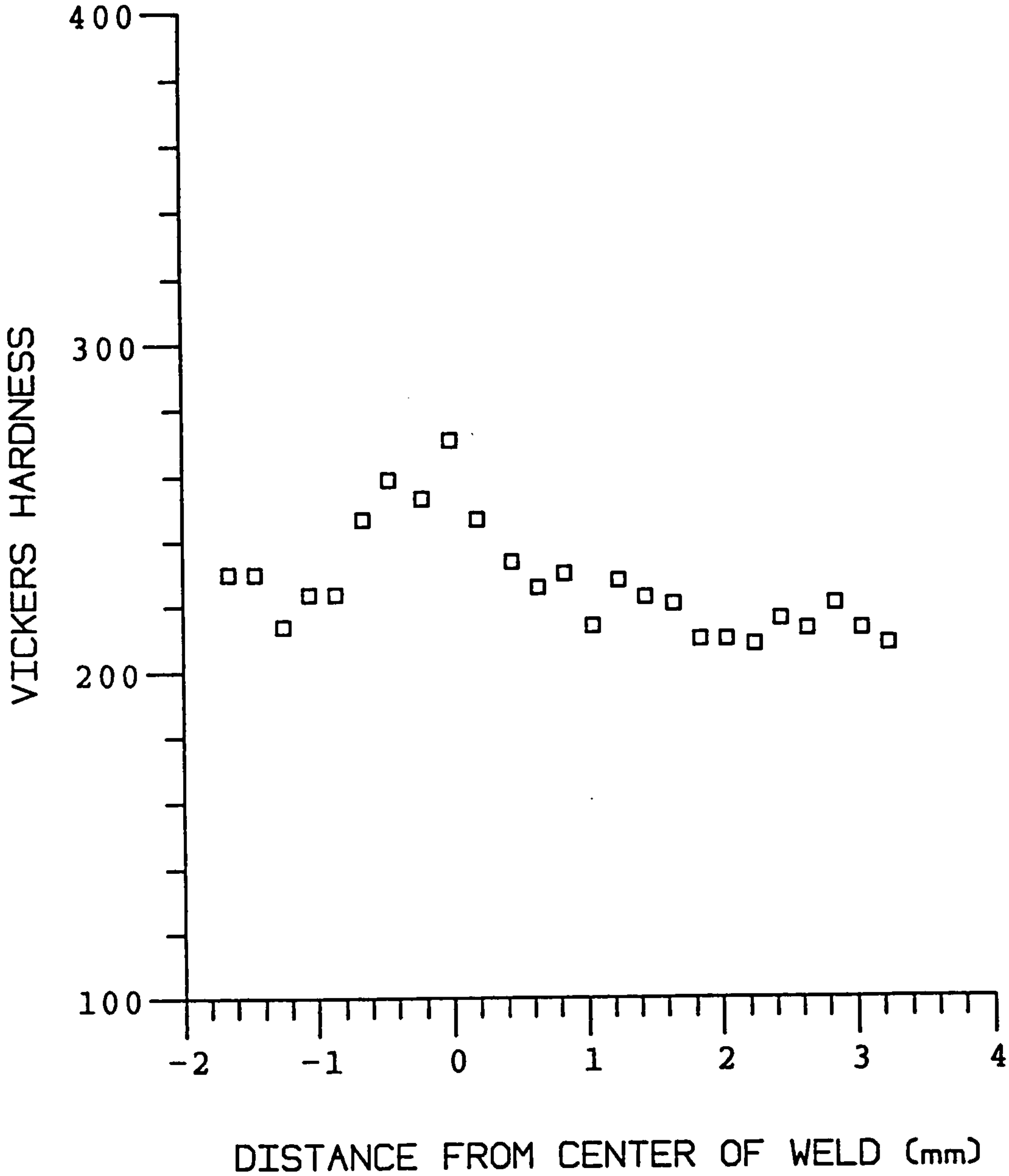

Figure IV-16. Microhardness versus position relative to the center of the weld pool for sample AR5.

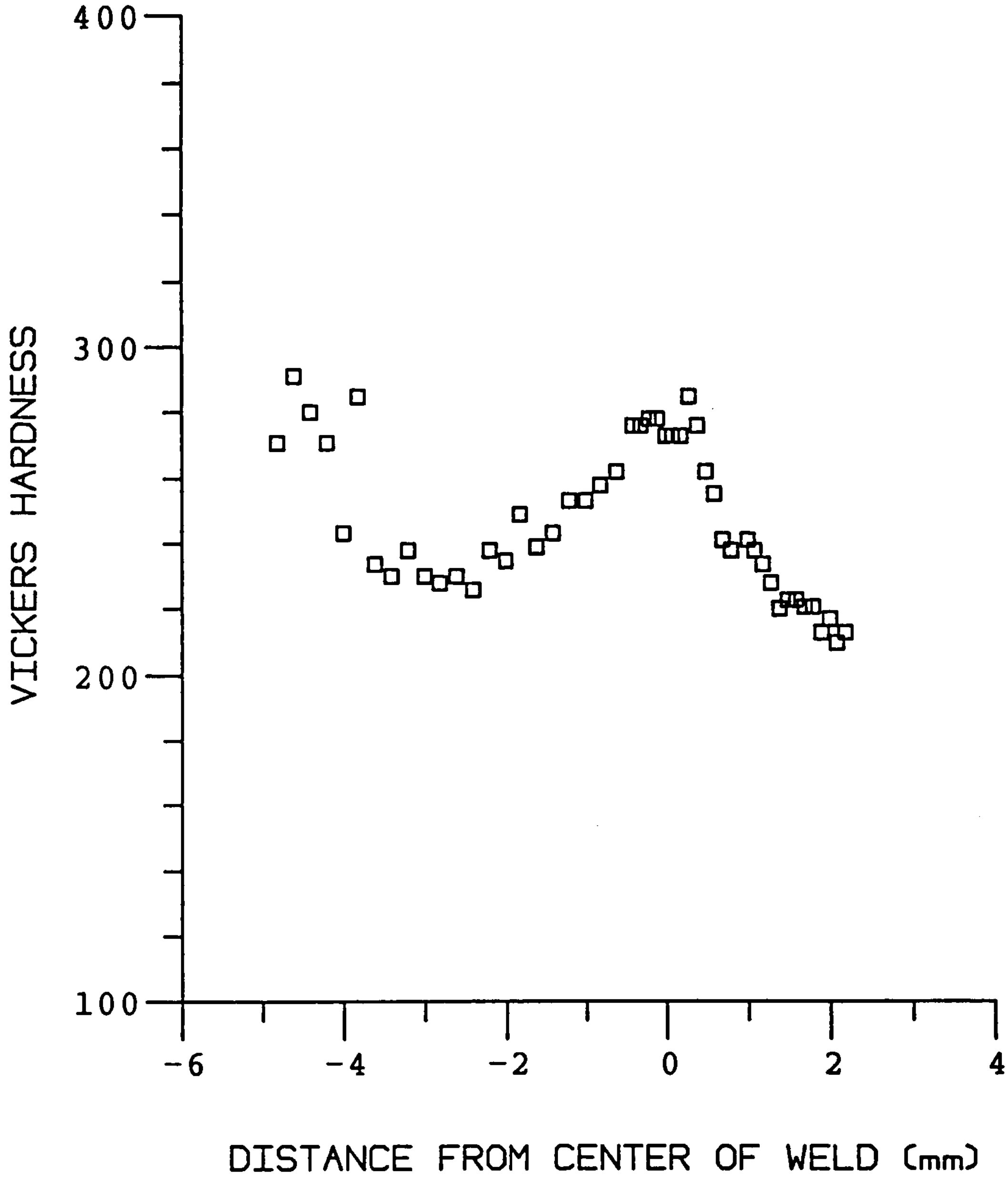

Figure IV-17. Microhardness versus position relative to the center of the weld pool for sample AR7.

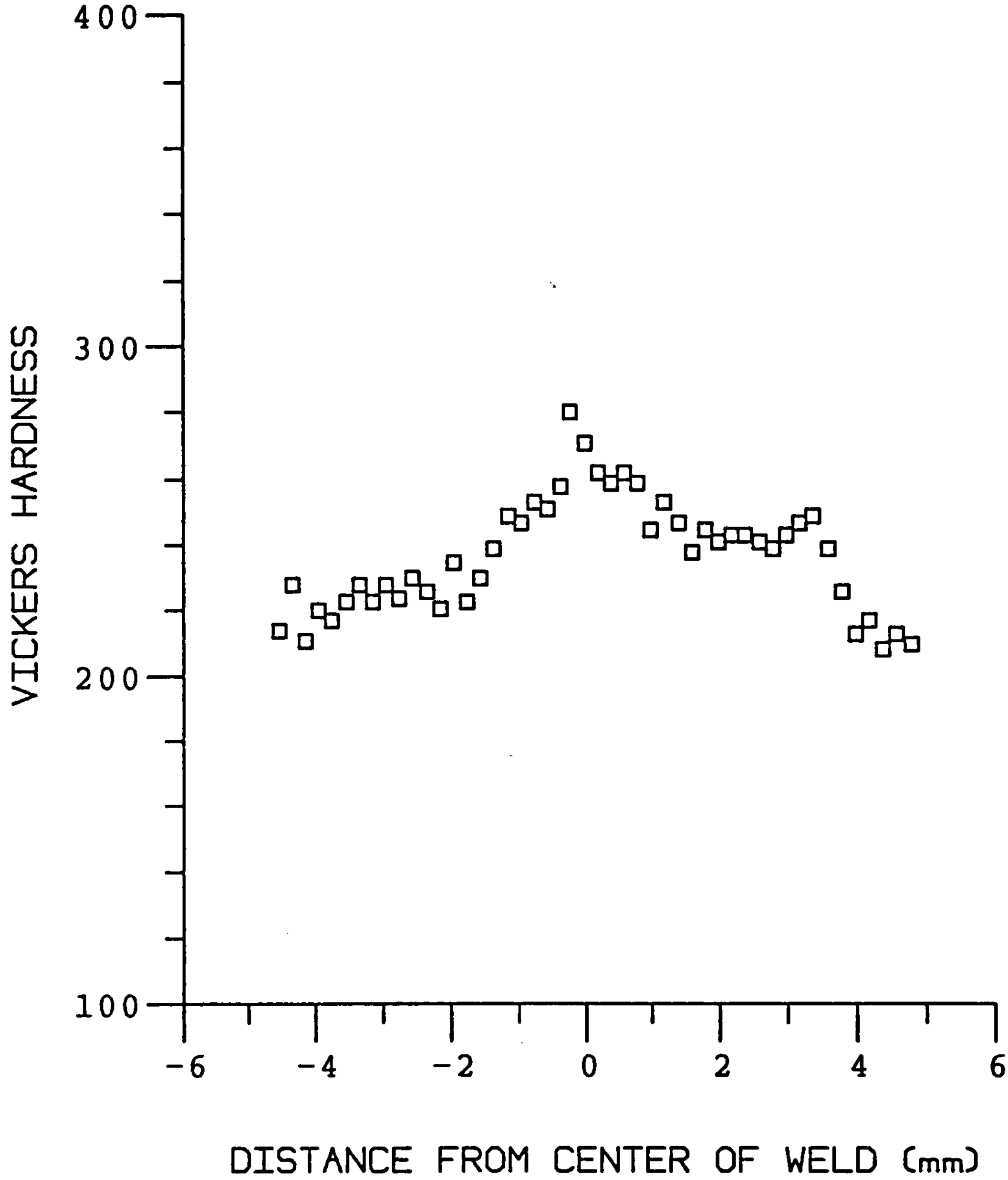

Figure IV-18. Microhardness versus position relative to the center of the weld pool for sample AR9.

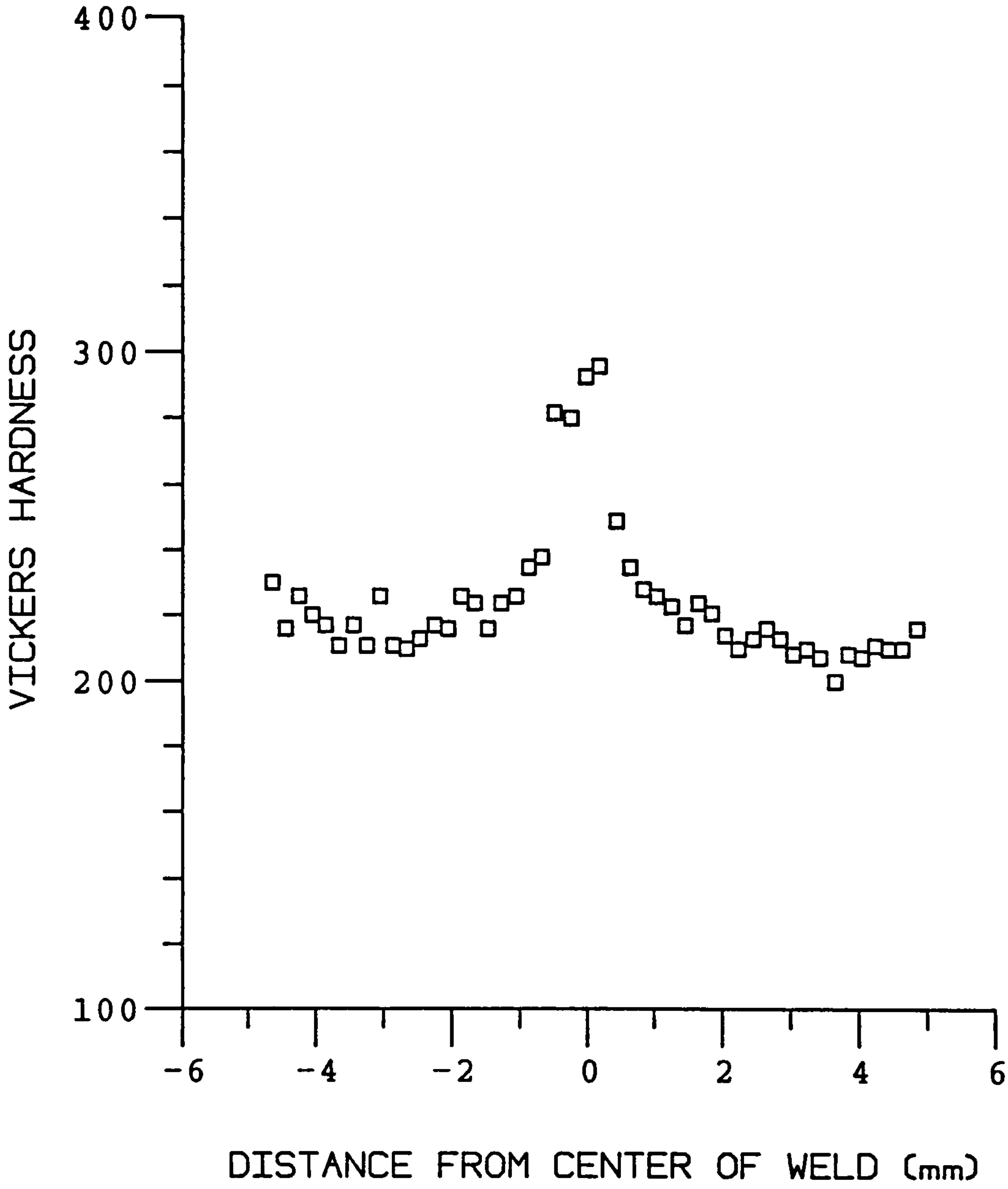

Figure IV-19. Microhardness versus position relative to the center of the weld pool for sample AR11.

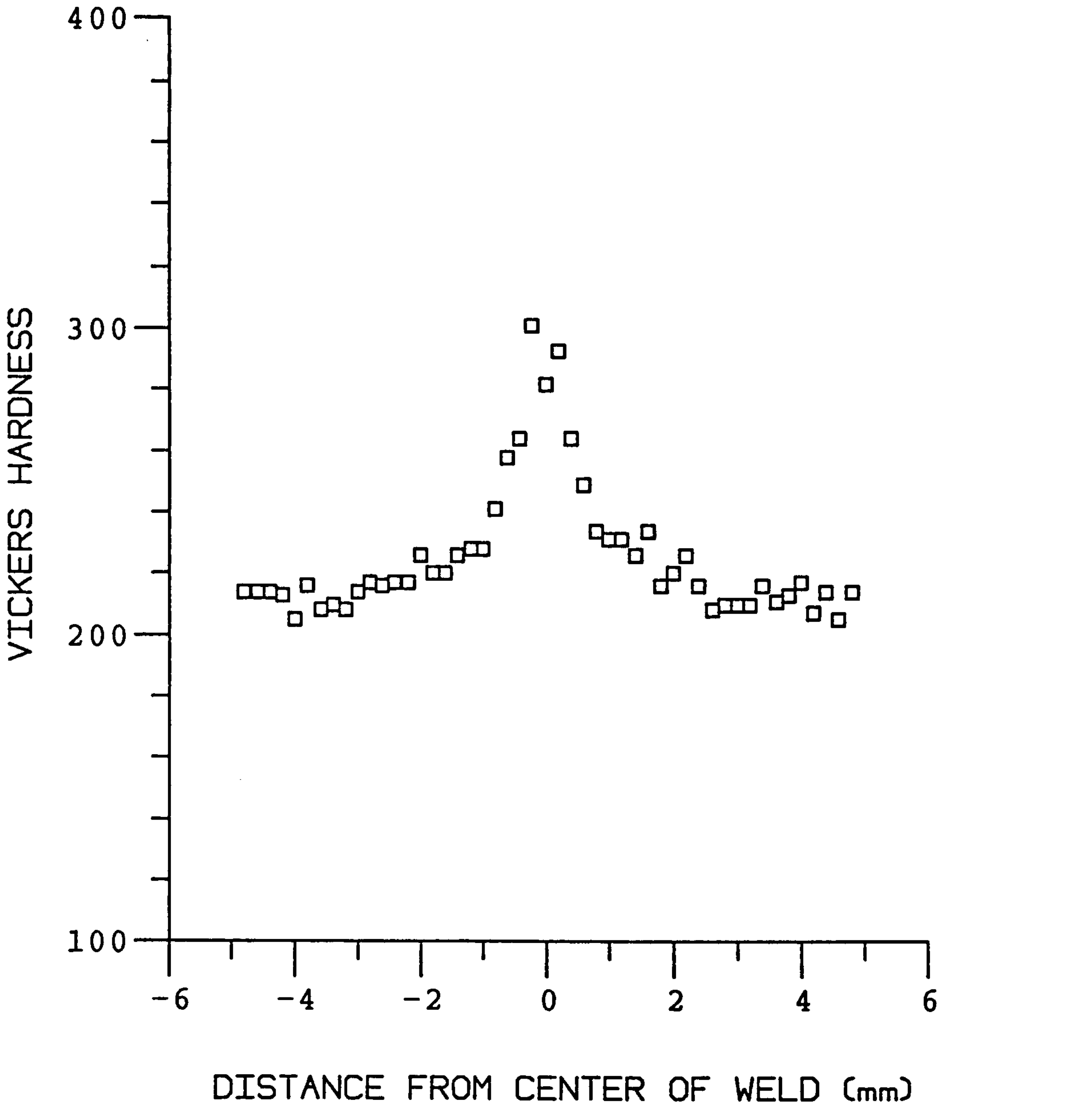

Figure IV-20. Microhardness versus position relative to the center of the weld pool for sample AR13.

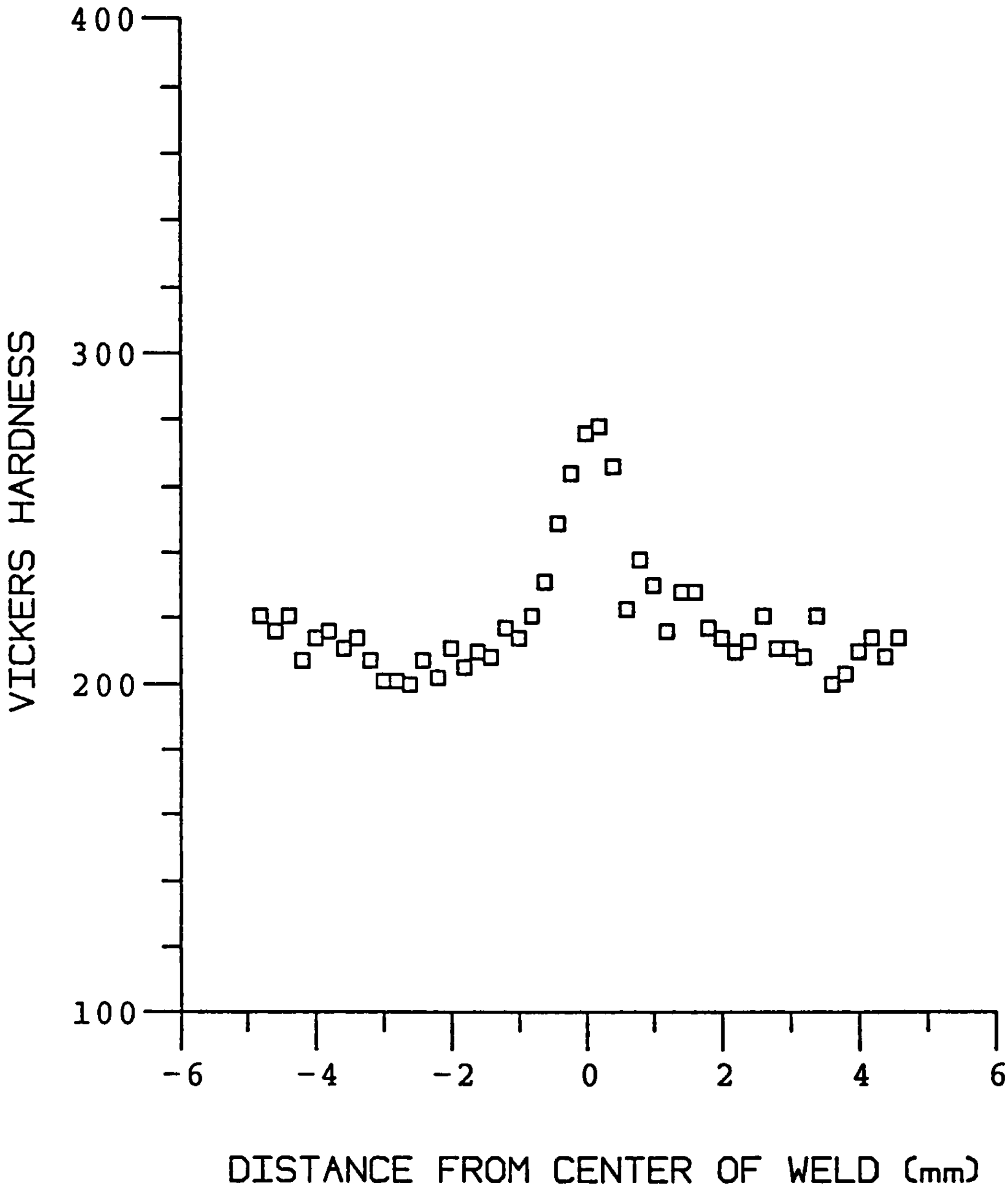

Figure IV-21. Microhardness versus position relative to the center of the weld pool for sample AR15.

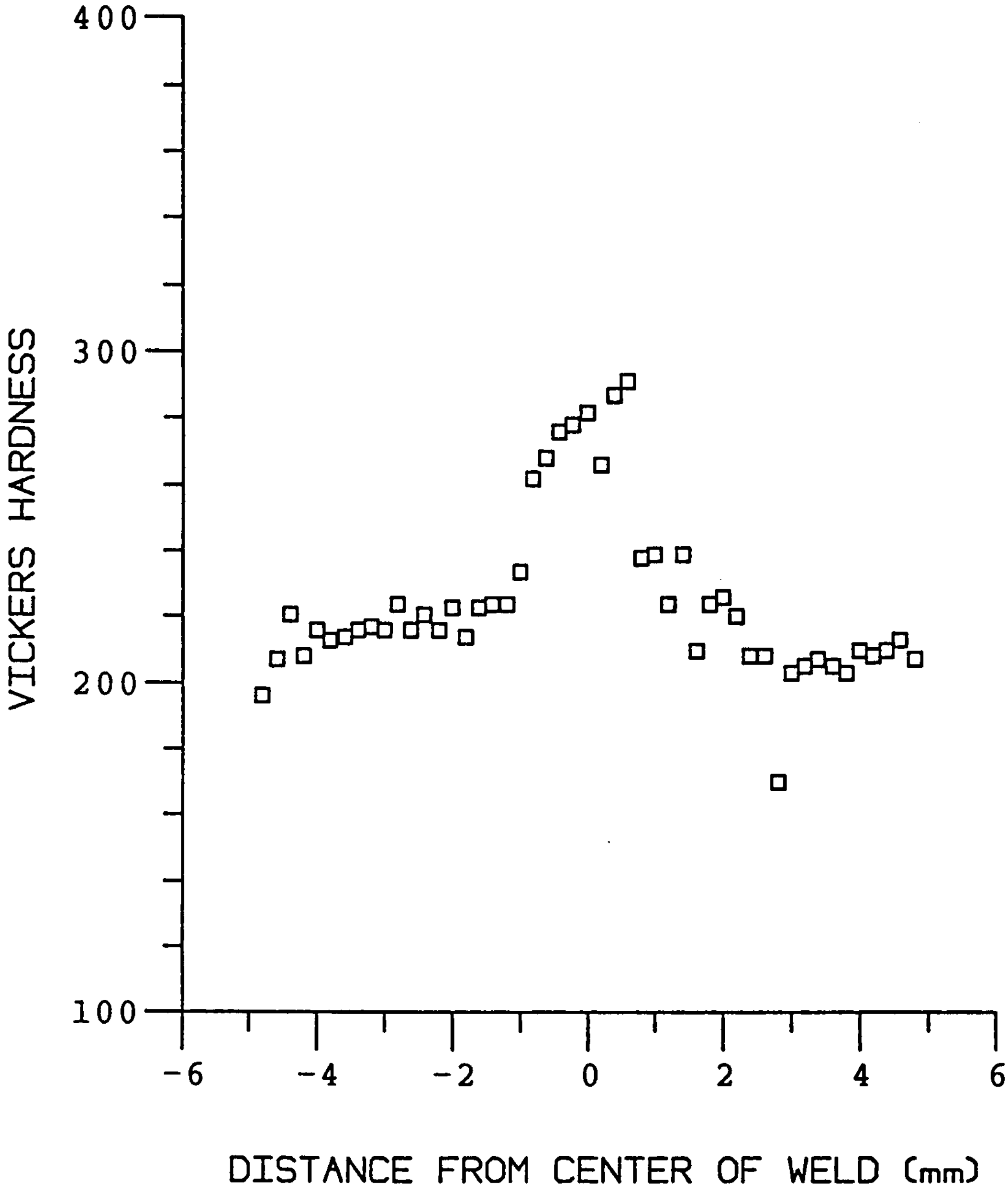

Figure IV-22. Microhardness versus position relative to the center of the weld pool for sample AR17.

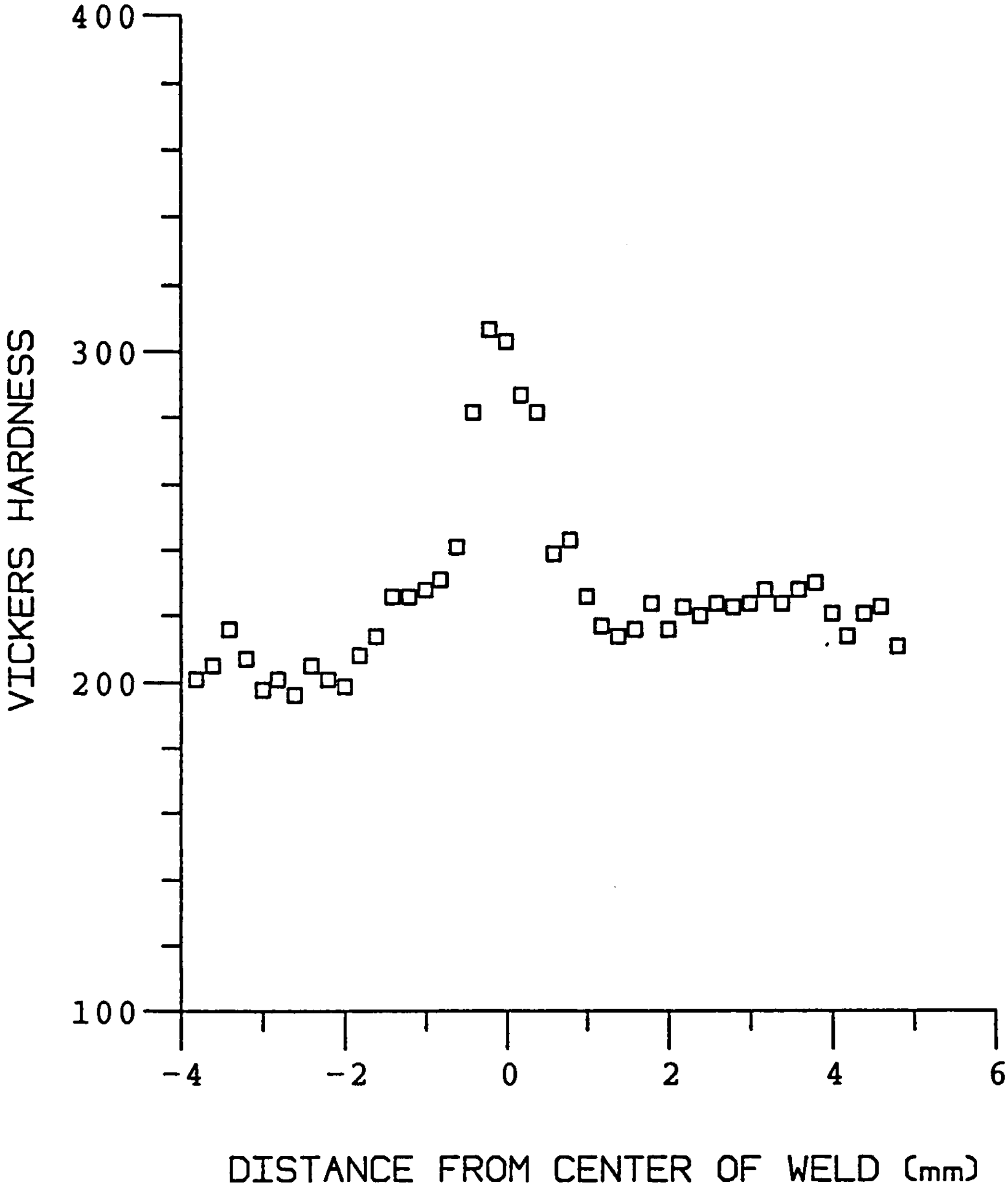

Figure IV-23. Microhardness versus position relative to the center of the weld pool for sample AR19.

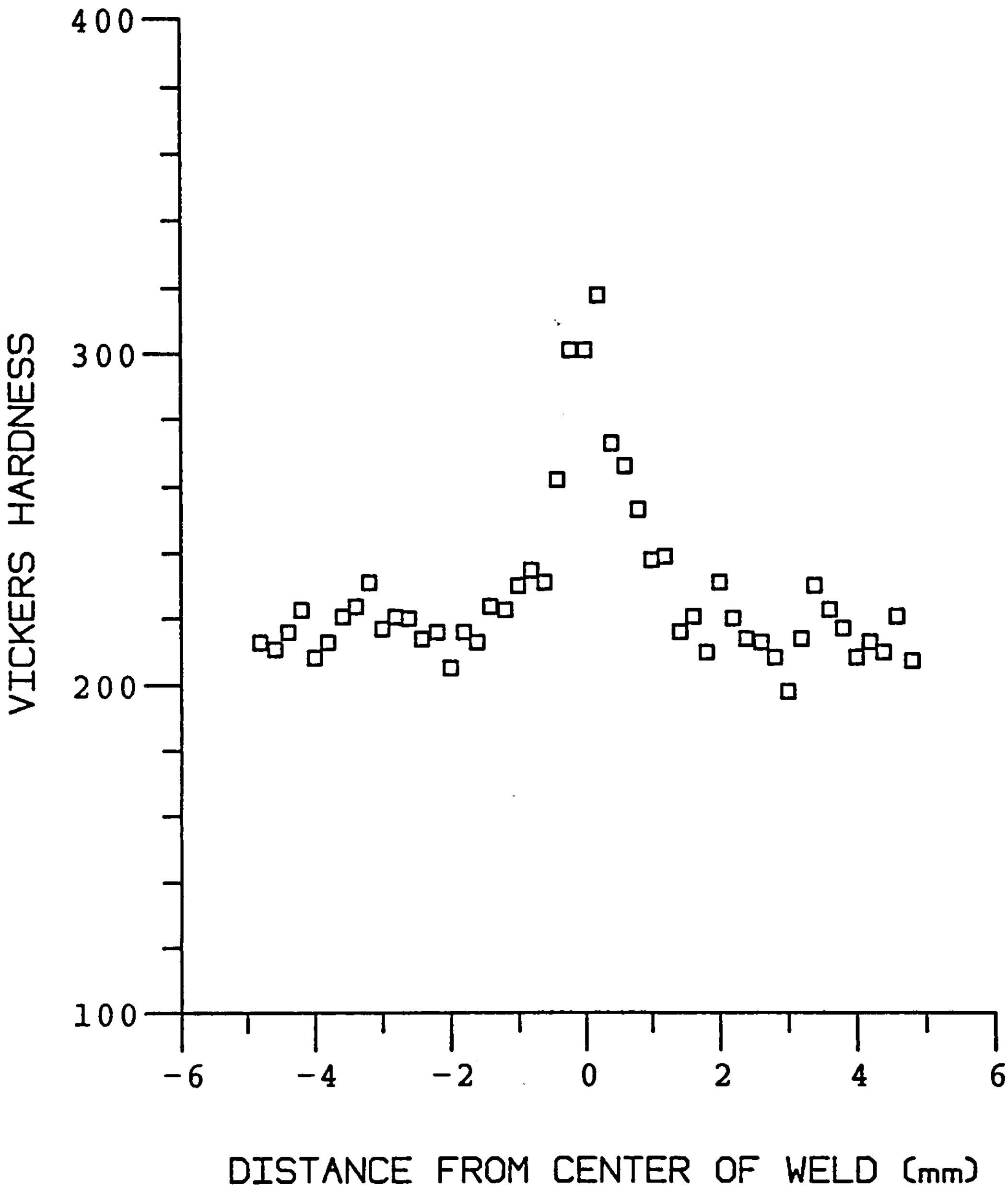

Figure IV-24. Microhardness versus position relative to the center of the weld pool for sample AR21.

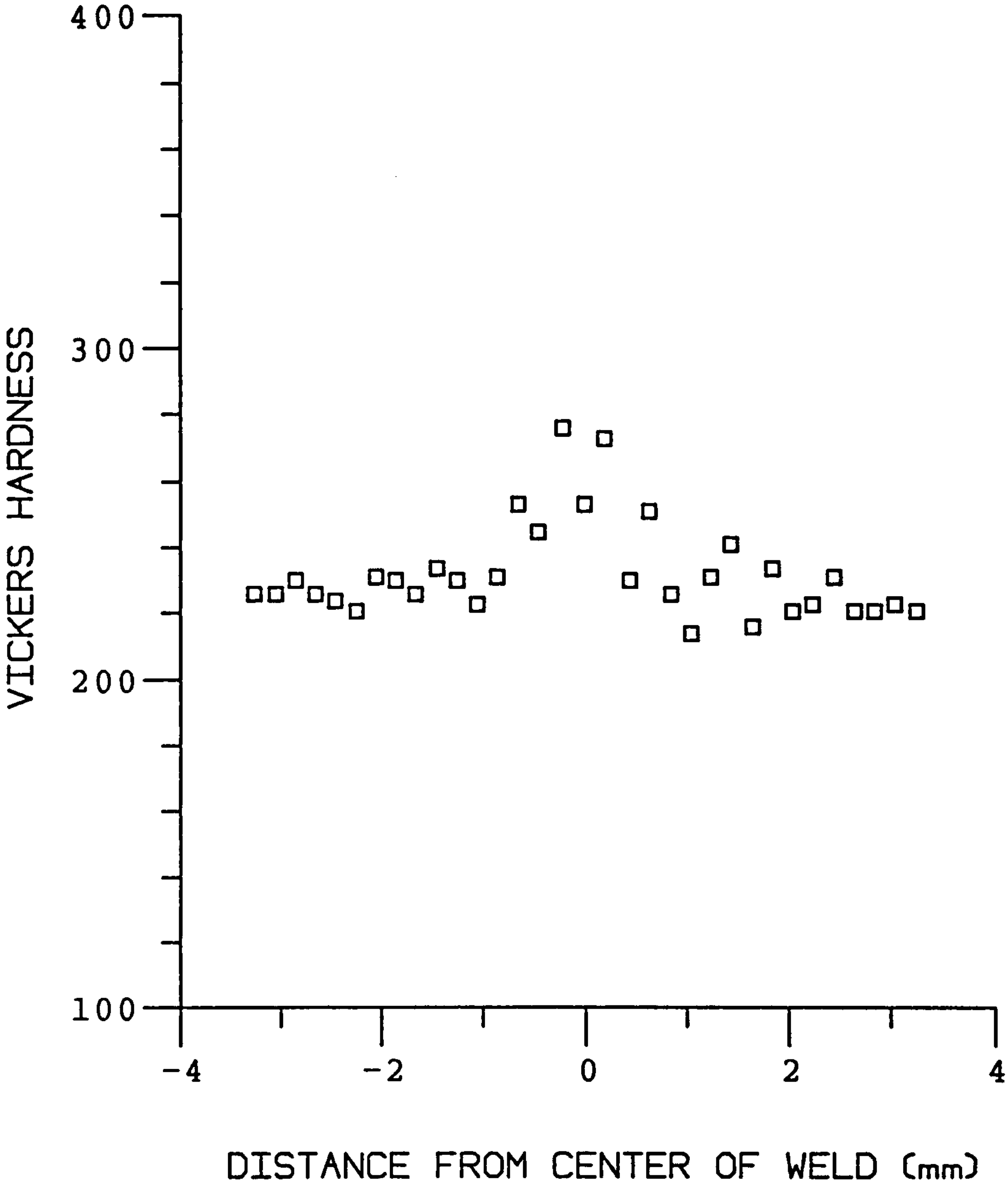

Figure IV-25. Microhardness versus position relative to the center of the weld pool for sample ST5.

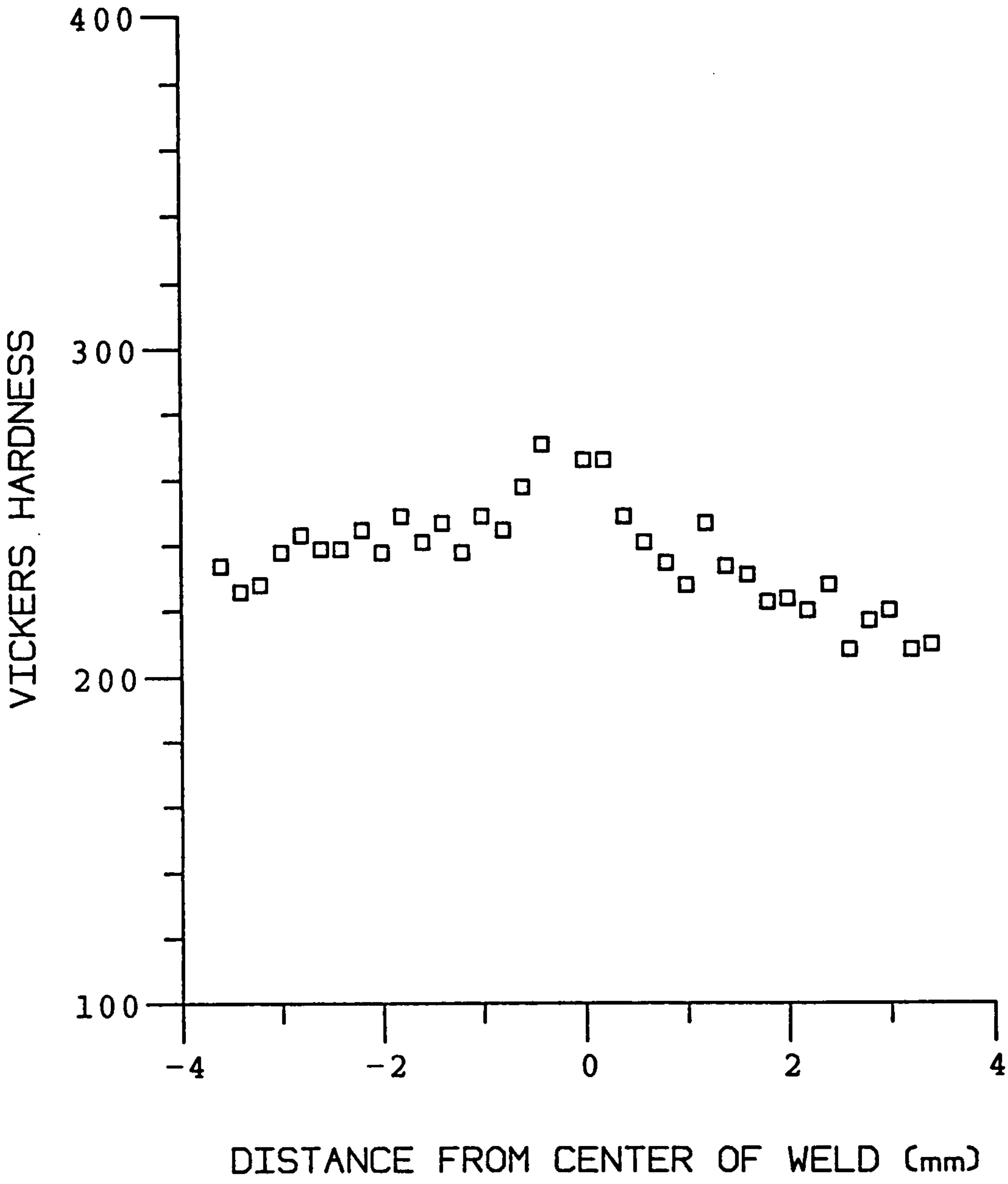

Figure IV-26. Microhardness versus position relative to the center of the weld pool for sample ST7.

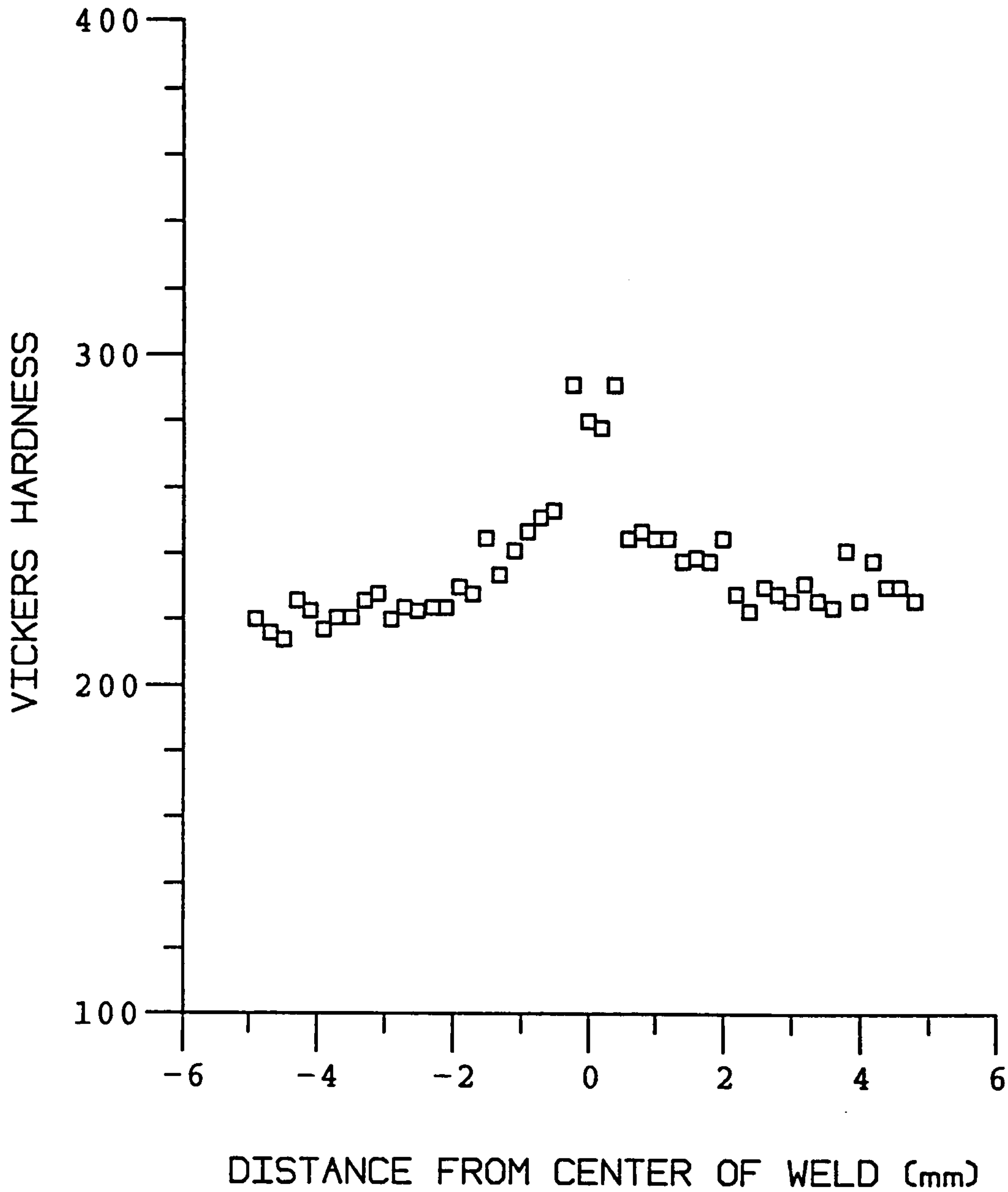

Figure IV-27. Microhardness versus position relative to the center of the weld pool for sample ST9.

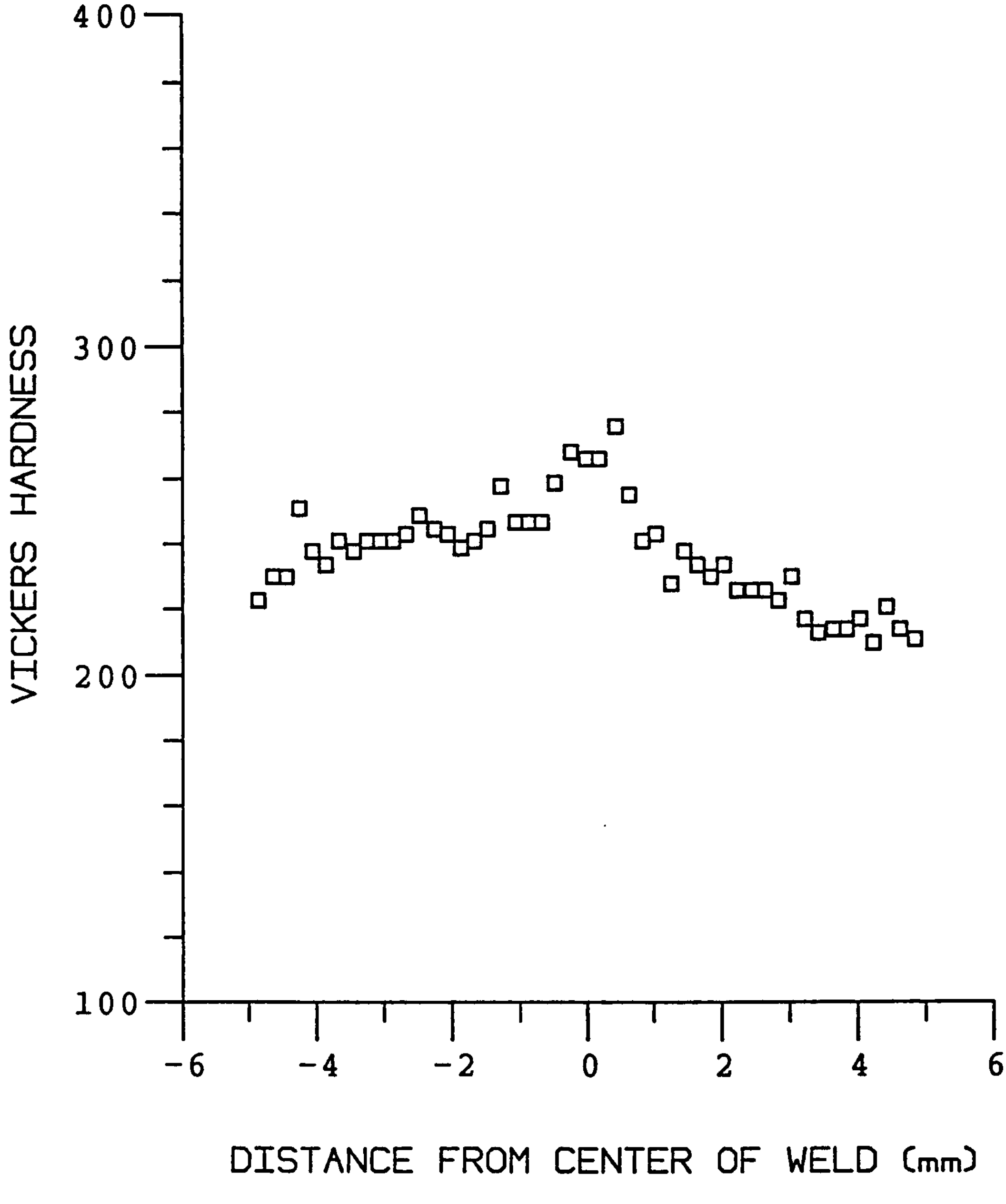

Figure IV-28. Microhardness versus position relative to the center of the weld pool for sample ST11.

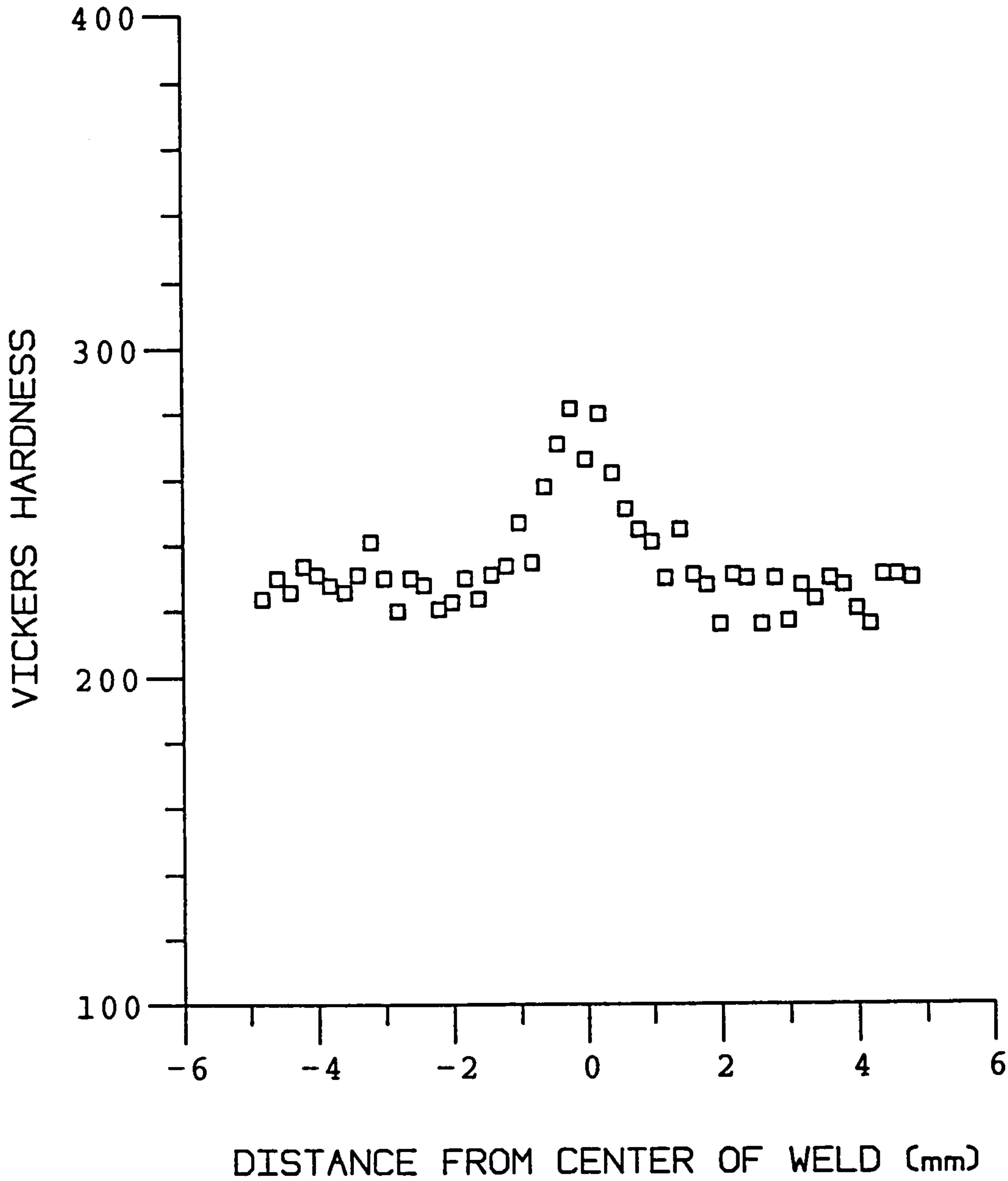

Figure IV-29. Microhardness versus position relative to the center of the weld pool for sample ST13.

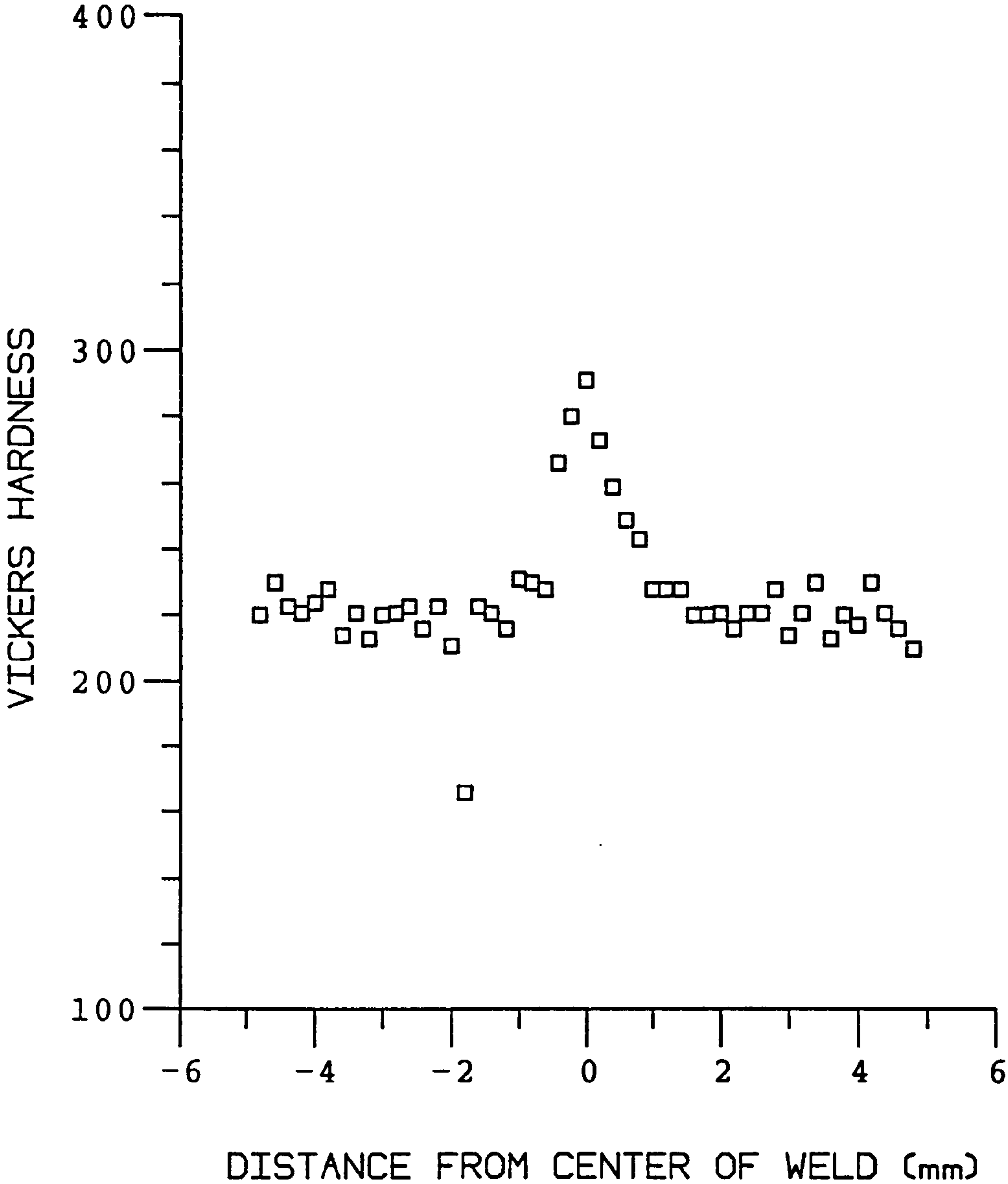

Figure IV-30. Microhardness versus position relative to the center of the weld pool for sample ST15.

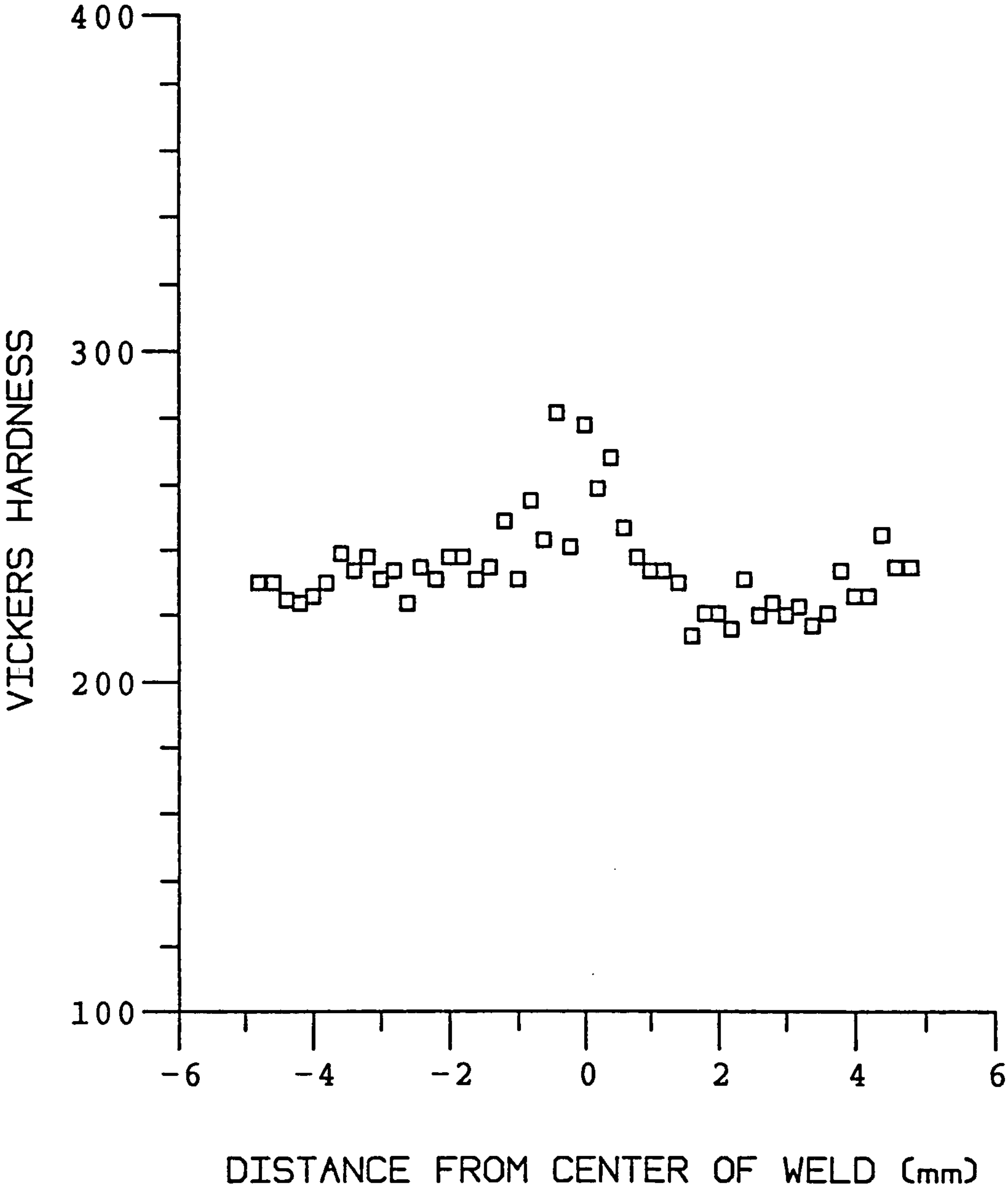

Figure IV-31. Microhardness versus position relative to the center of the weld pool for sample ST17.

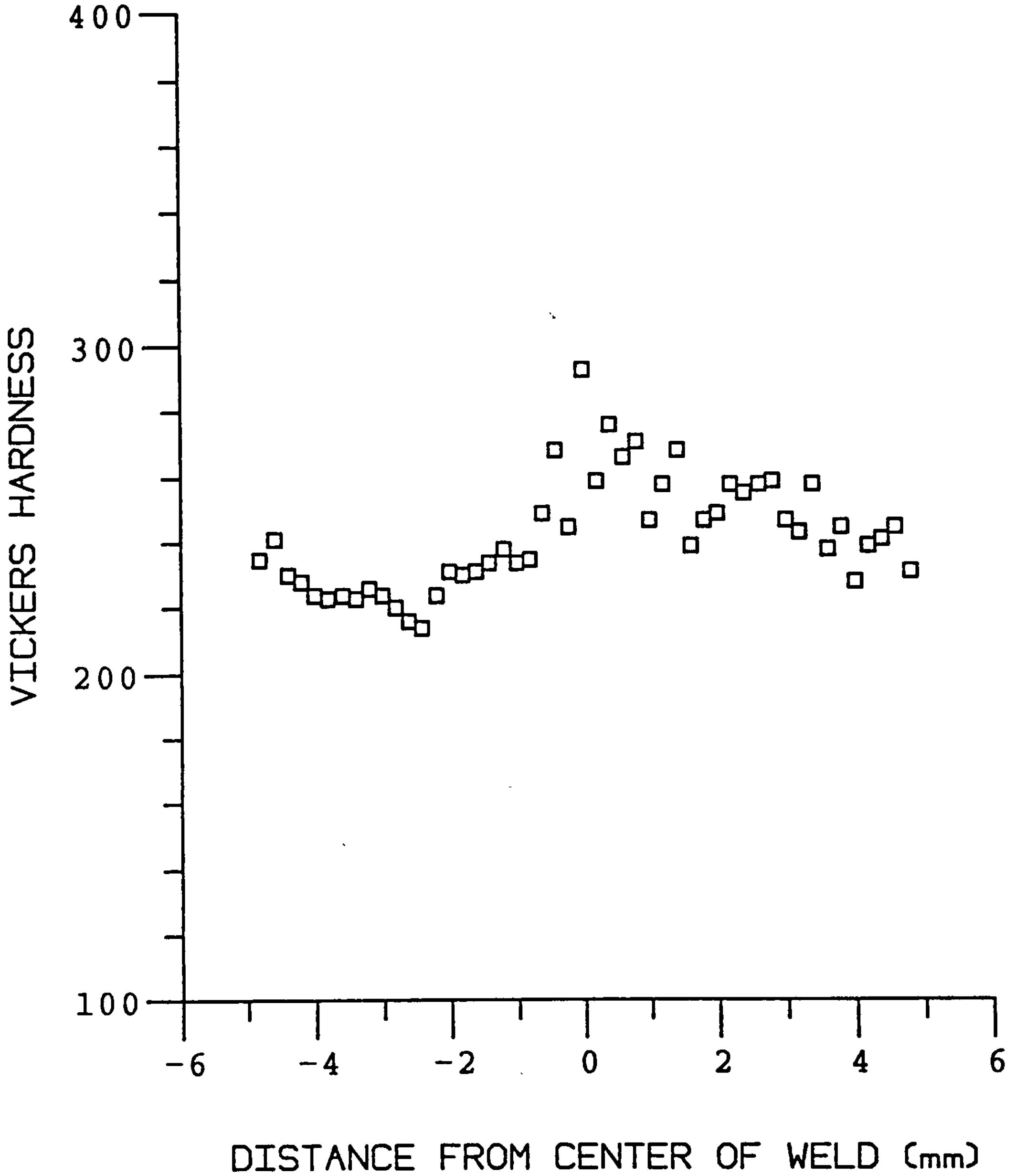

Figure IV-32. Microhardness versus position relative to the center of the weld pool for sample ST19.

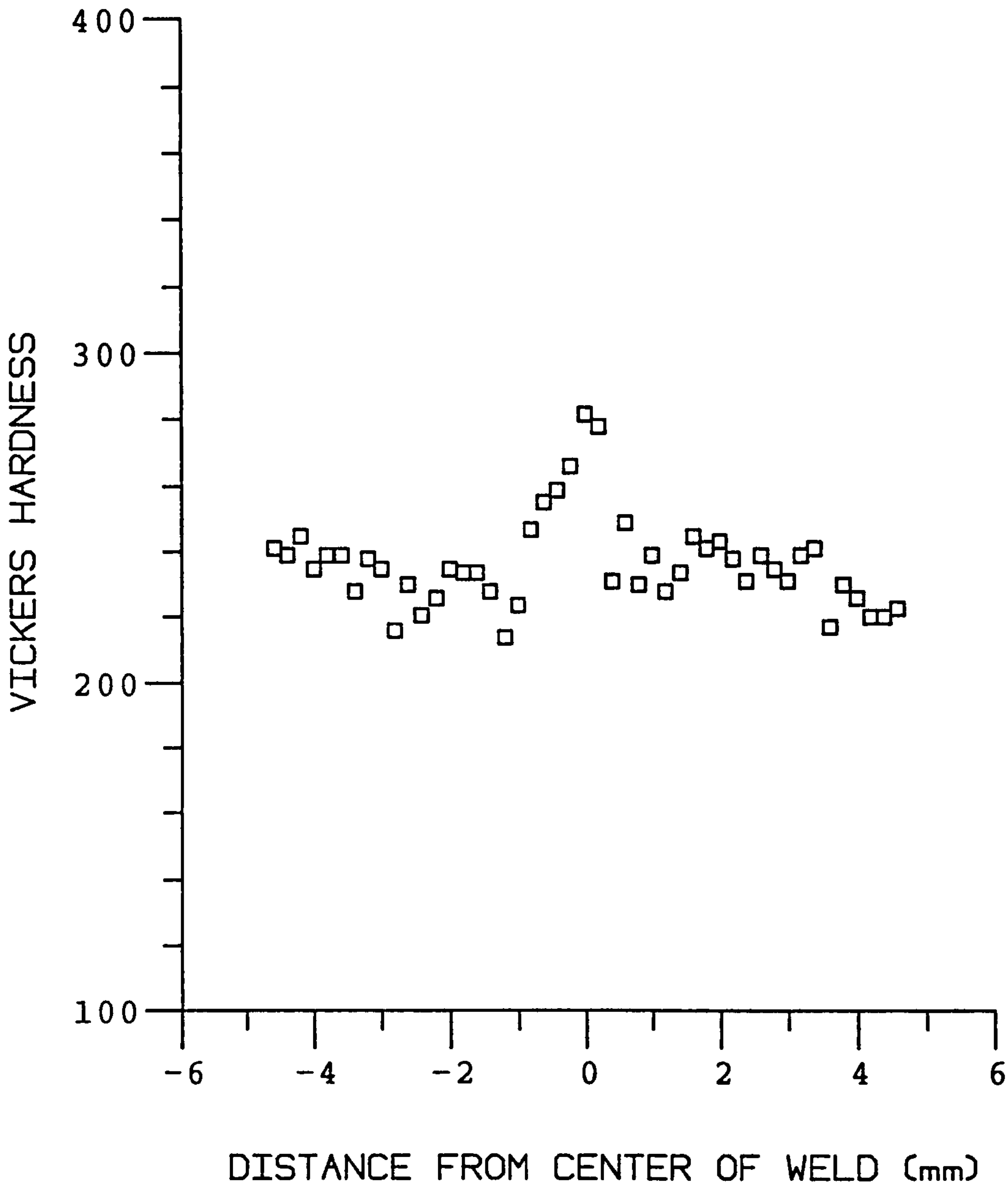

Figure IV-33. Microhardness versus position relative to the center of the weld pool for sample ST21.

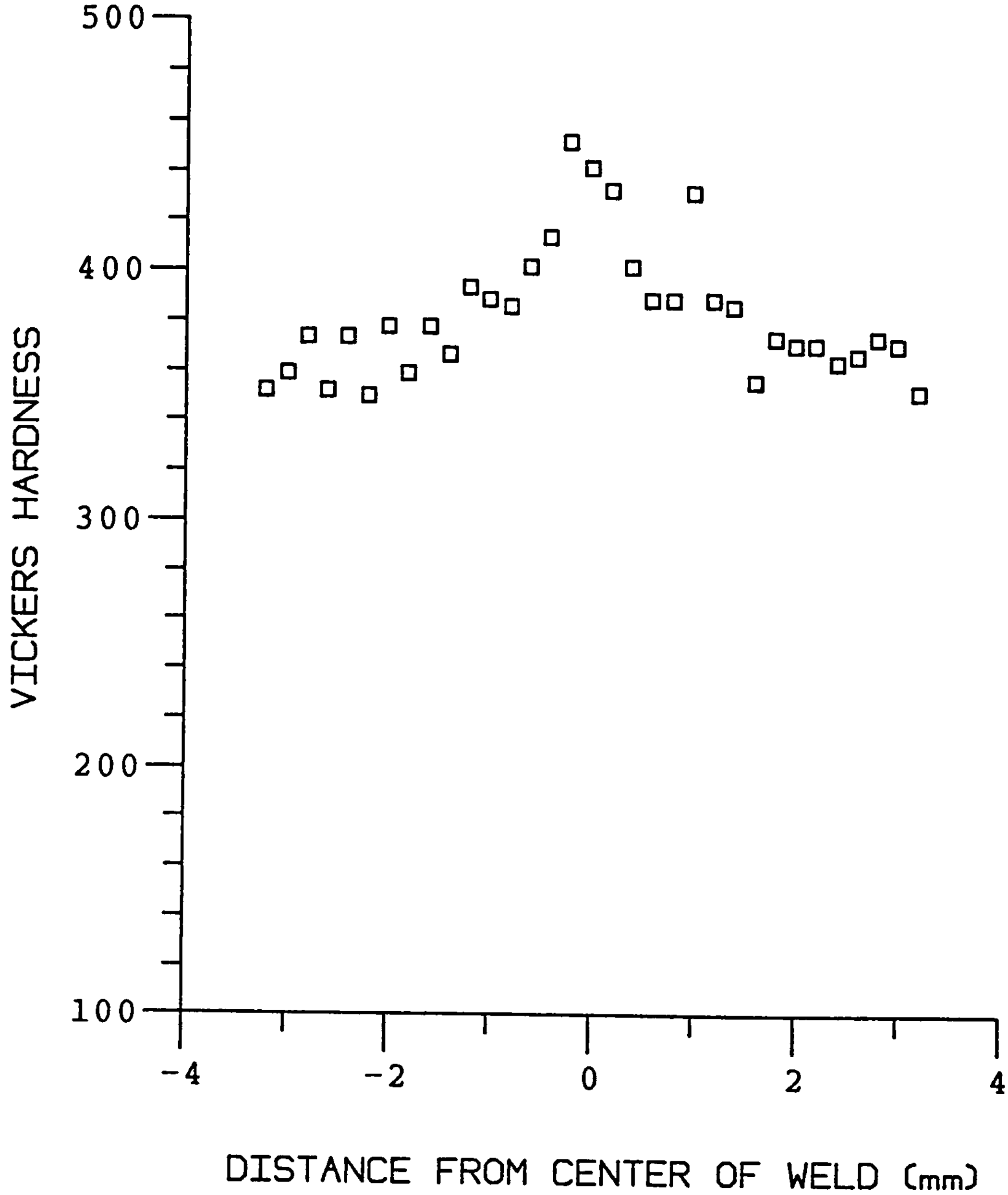

Figure IV-34. Microhardness versus position relative to the center of the weld pool for sample STA5.

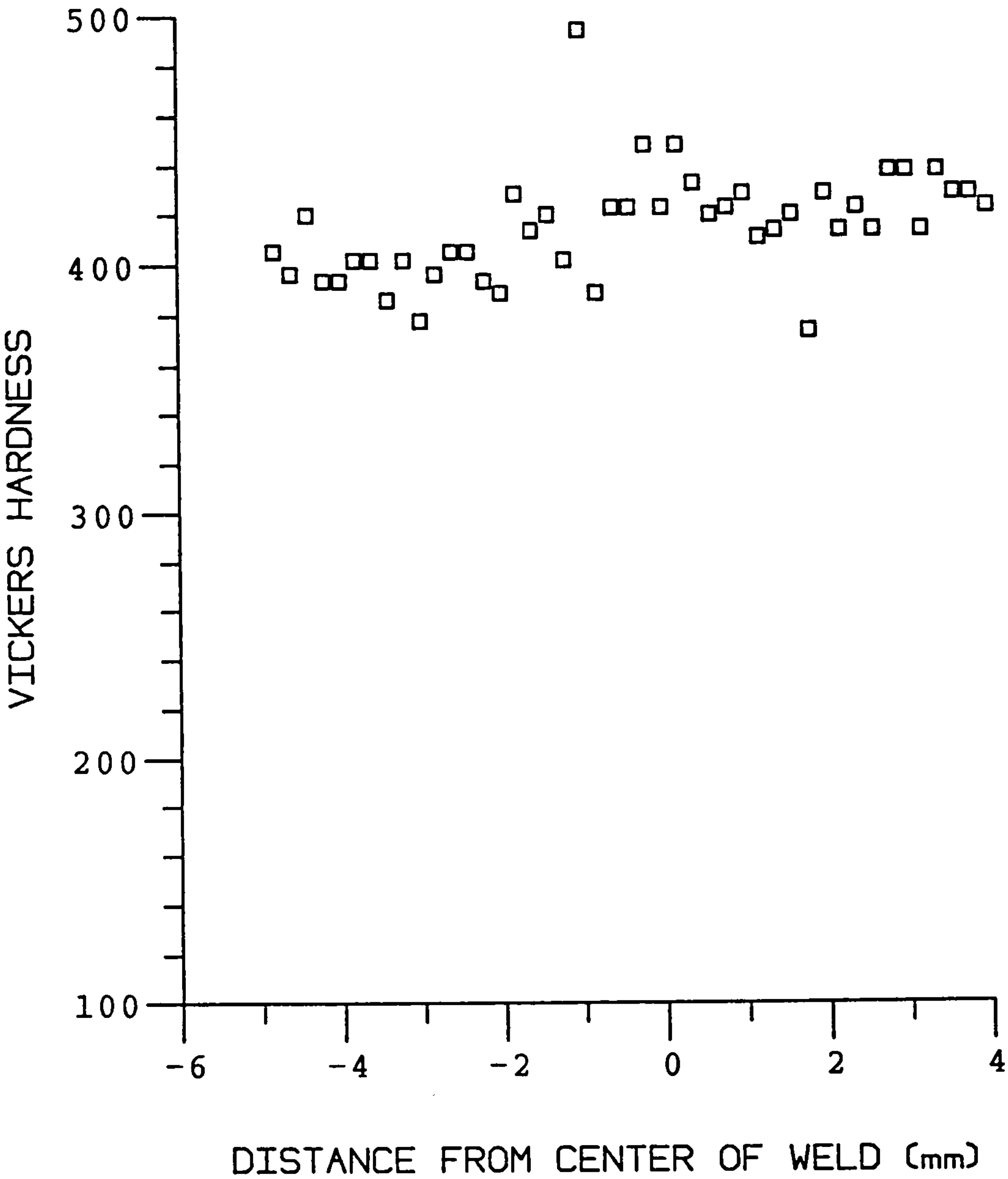

Figure IV-35. Microhardness versus position relative to the center of the weld pool for sample STA7.

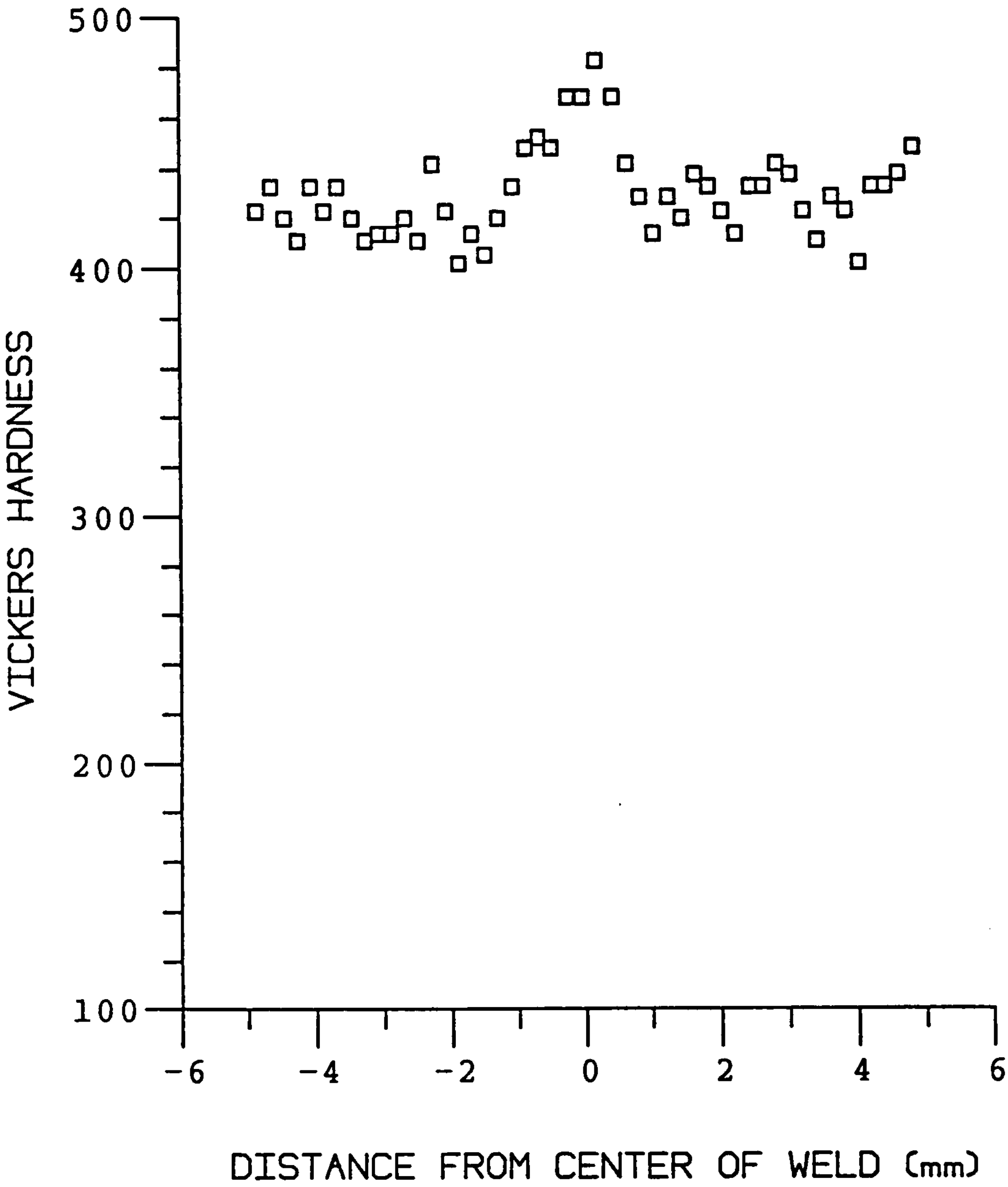

Figure IV-36. Microhardness versus position relative to the center of the weld pool for sample STA9.

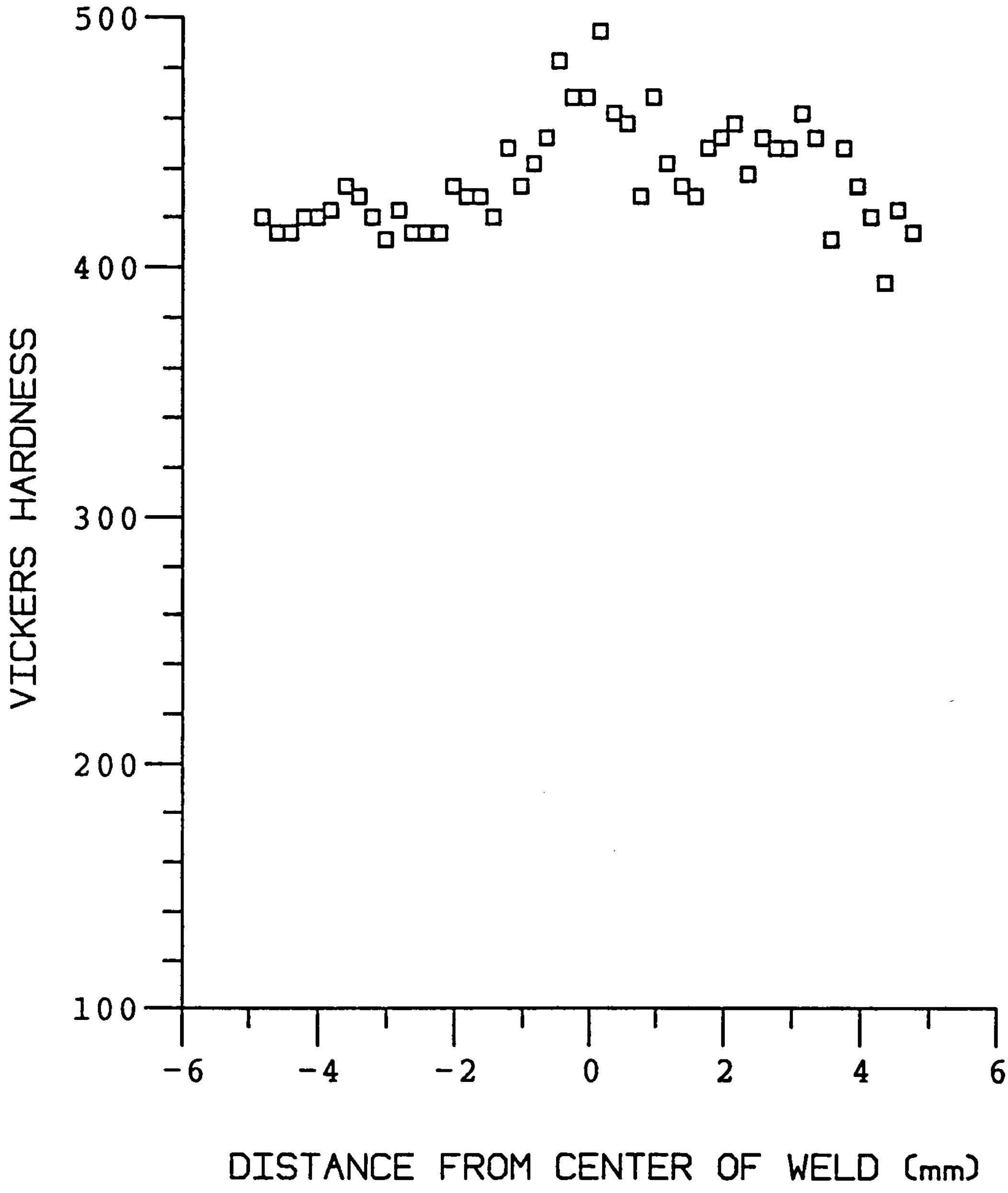

Figure IV-37. Microhardness versus position relative to the center of the weld pool for sample STA11.

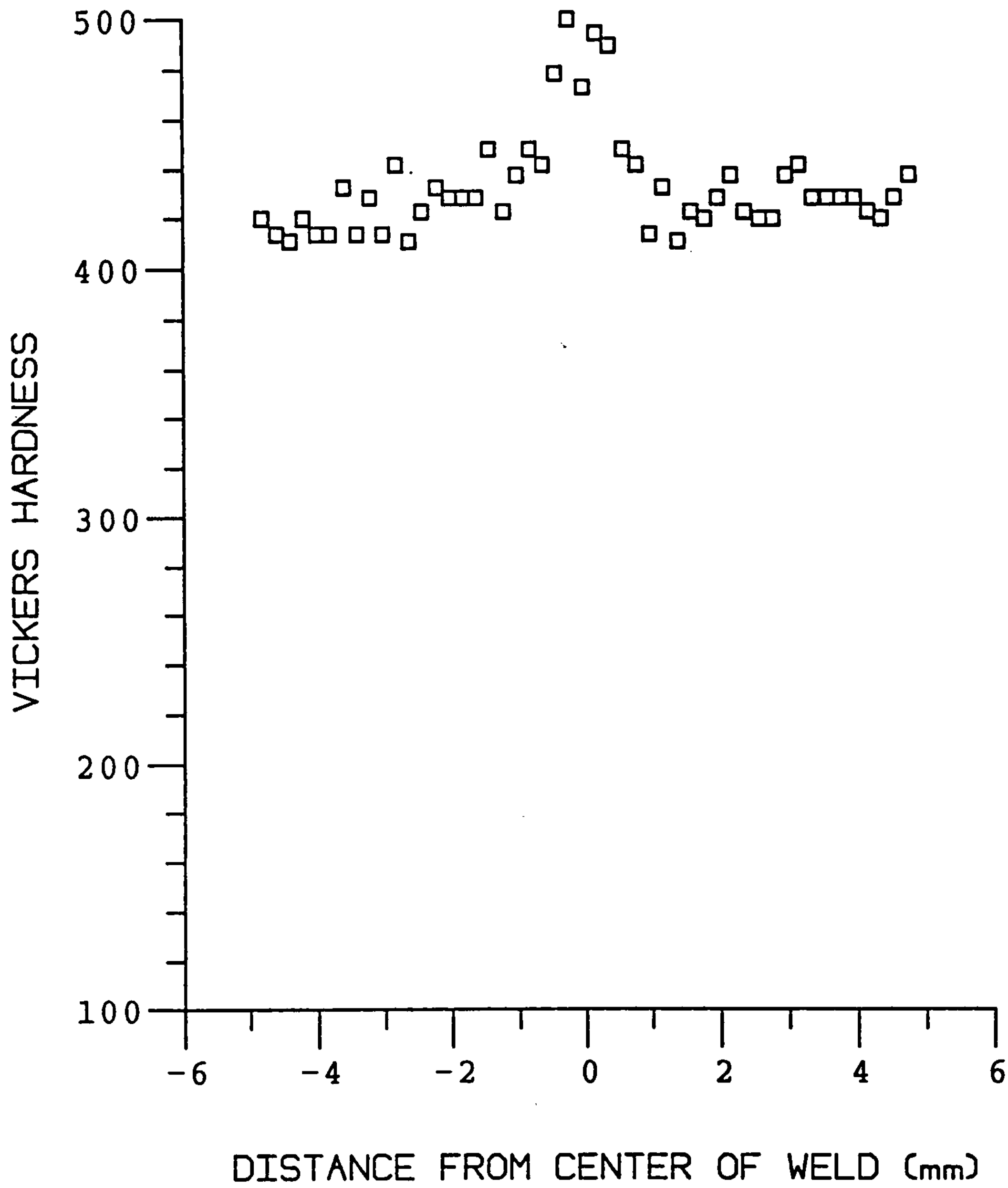

Figure IV-38. Microhardness versus position relative to the center of the weld pool for sample STA13.

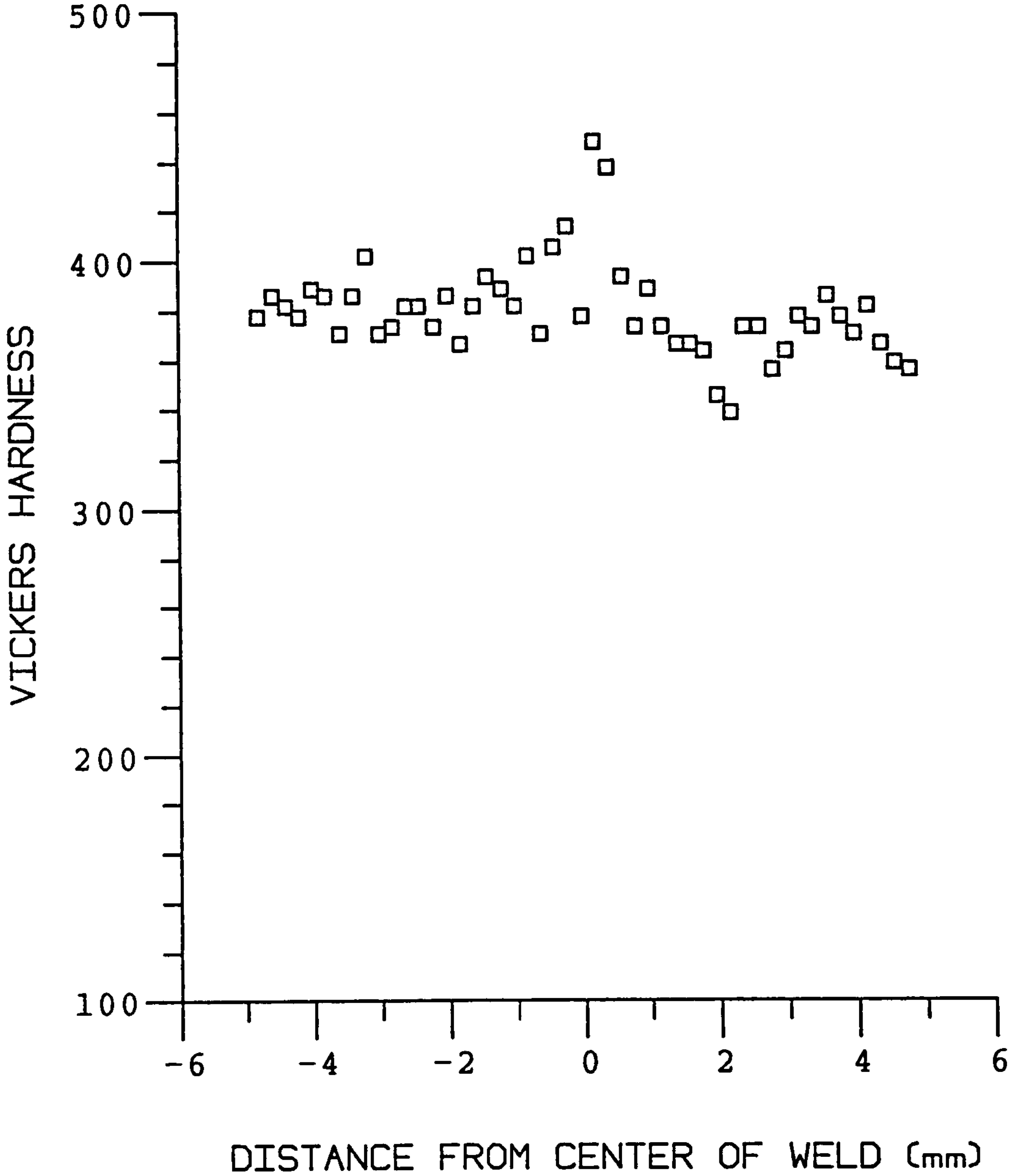

Figure IV-39. Microhardness versus position relative to the center of the weld pool for sample STA15.

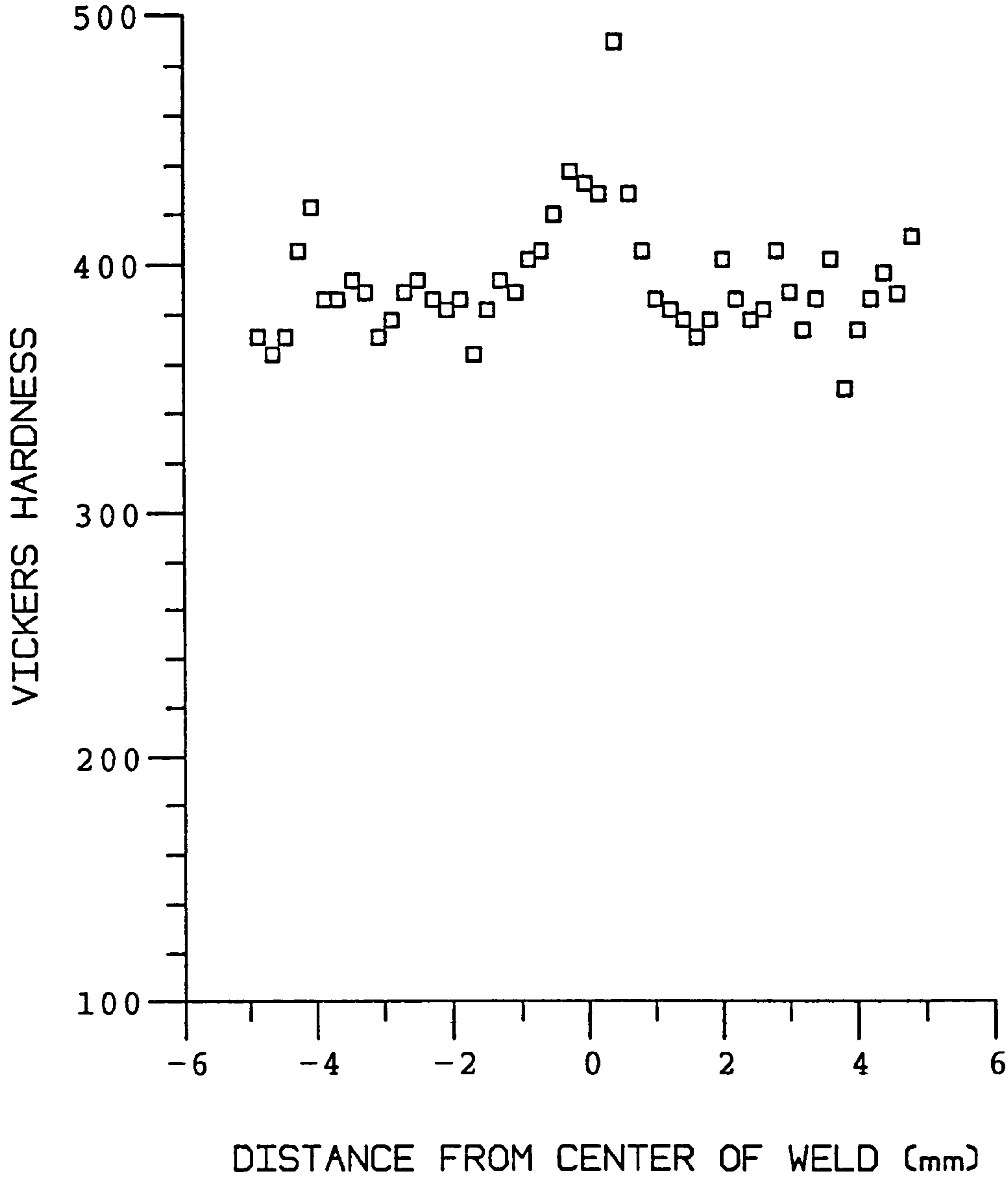

Figure IV-40. Microhardness versus position relative to the center of the weld pool for sample STA17.

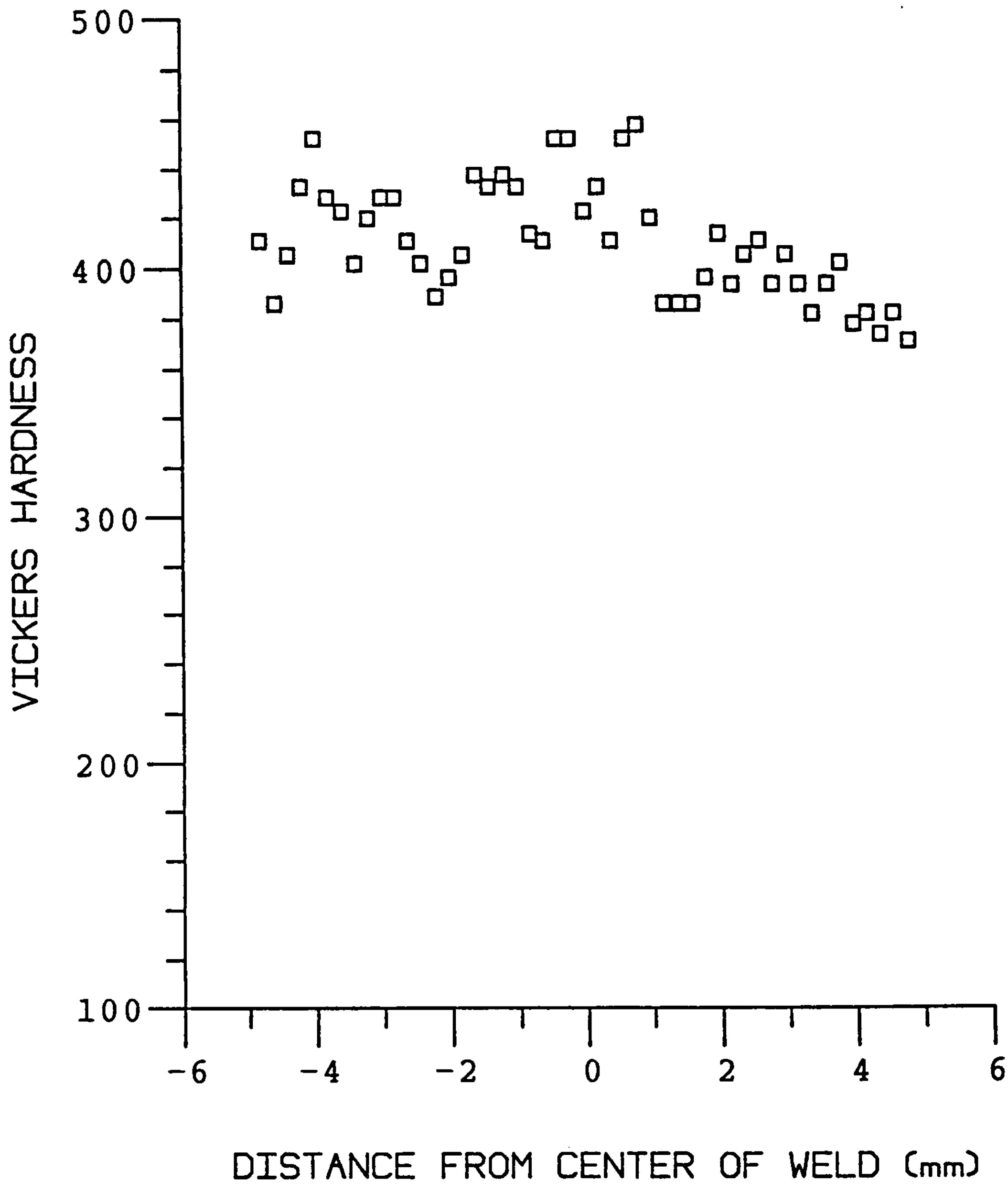

Figure IV-41. Microhardness versus position relative to the center of the weld pool for sample STA19.

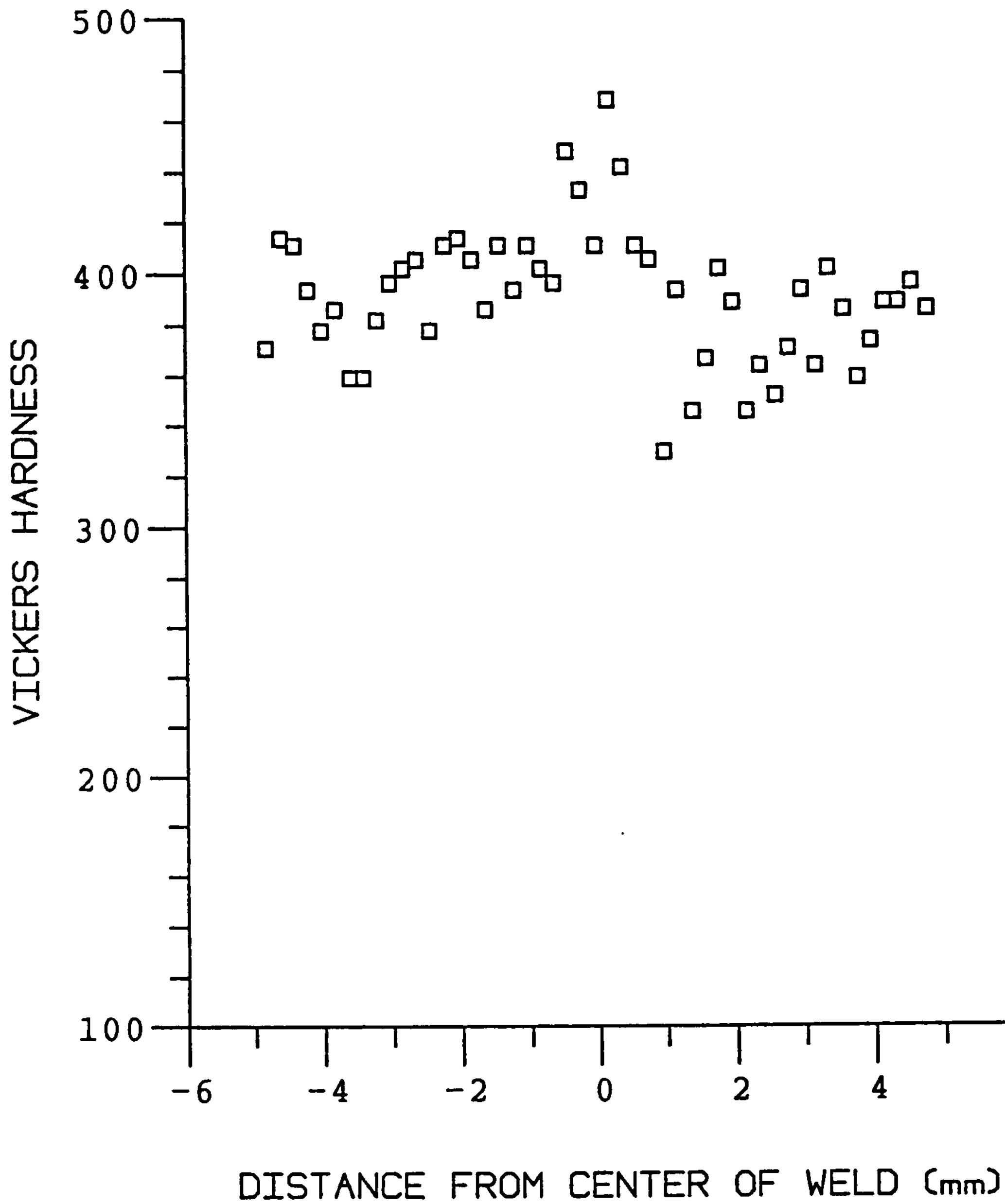

Figure IV-42. Microhardness versus position relative to the center of the weld pool for sample STA21.

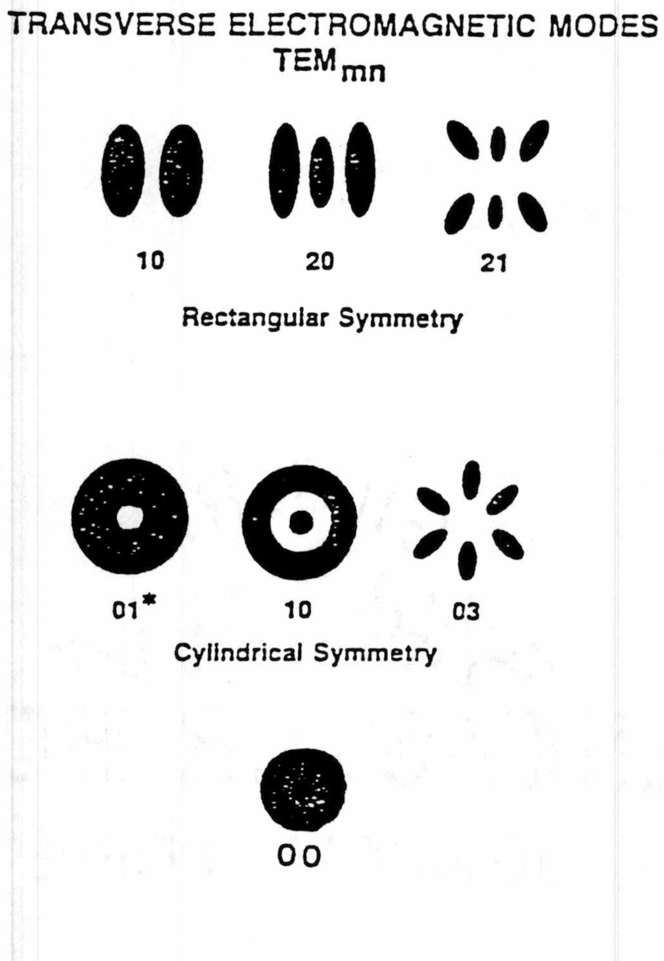

Figure A-1. Spatial intensity patterns for various common transverse electromagnetic modes.

APPENDIX C

TABLE II-1

COMPOSITION OF WROUGHT INCONEL 718

Element	Weight %
Cr	19.0
Ni	52.5
Mo	3.0
Nb	5.1
Ti	0.9
Al	0.5
Fe	18.5
C	0.08 (max)
Cu and other	0.15 (max)

TABLE III-1

PULSE WELD PARAMETERS

Variable	Units
Weld Speed	1.5 m/min
Focus	1 mm below XY plane
Pulse On Time	17 ms
Pulse Off Time	1-21 ms (by 2 ms)
Peak Power	3.2 kW
Gas	Helium
Flow Rate	60 l/min
Treatment	AR and ST

TABLE III-2

CW WELD PARAMETERS

Variable	Units
Weld Speed	1.5-3.5 m/min
Focus	1 mm below XY plane
Delivered Peak Power	2.5 kW
Gas	Helium
Flow Rate	60 l/min
Treatment	AR

VITA

Kevin T. Zysk was born in Boston, Massachusetts on July 18, 1950. He was graduated from Shaw Preparatory School in Boston in Aug. 1969. He later attended Northeastern University and Lowell Technological Institute on a part-time basis.

After working in private industry for a number of years he entered The University of Tennessee at Chattanooga in Sept. 1983. In may 1987, he received the degree of Bachelor of Science in Engineering.

He began study at the University of Tennessee Space Institute toward the degree of Master of Science in Mechanical Engineering in June 1987. This degree was awarded in May 1989.